Martin Söllradl, BSc

Fast Estimation of the Bound Pool Fraction in the Brain

MASTER'S THESIS

to achieve the university degree of

Diplom-Ingenieur

Master's degree programme: Biomedical Engineering

submitted to

Graz University of Technology

Supervisor

Univ.-Prof. Dipl.-Ing. Dr.techn. Rudolf Stollberger
Institute of Medical Engineering

Second Supervisor

Assoz. Prof. Univ.-Doz. Dipl.-Ing. Dr. Stefan Ropele
Neuroimaging Research Unit

Graz, April 2016

AFFIDAVIT

I declare that I have authored this thesis independently, that I have not used other than the declared sources/resources, and that I have explicitly indicated all material which has been quoted either literally or by content from the sources used. The text document uploaded to TUGRAZonline is identical to the present master‘s thesis dissertation.

Date

Signature

Abstract

The bound pool fraction (BPF) is a quantitative magnetization transfer (MT) parameter that has drawn interest in clinical research as a biomarker for the myelin content. Hence, it allows to quantify changes within the nervous system of the brain for example in a neurodegenerative disease like Multiple Sclerosis (MS). The estimation of high resolution BPF images in clinical acceptable scan times is still a challenging task. One approach that seems to overcome this issue is the fast BPF estimation from a single off-resonance measurement, which is based on constraints and assumptions of the pulsed MT-model. In the present Master's thesis this method was implemented and validated in three stages with the pulsed MT-model and numerical simulations.

In the first stage of the thesis, simulations with the pulsed MT-model and the coupled Bloch equations were carried out to validate the approximations of the pulsed MT-model. Furthermore a new numerical error model was developed to estimate the bias and error due noise of the fast BPF estimation for a specific sets of constraints.

In the second stage the constraints were estimated by fitting the parameters of the pulsed MT-model from bovine serum albumin (BSA) phantom measurements and post mortem measurements. With the derived constraints the fast BPF estimation was carried out and the estimated error was compared with the predicted error from the numerical simulations.

Finally, in the last stage, the model parameters of the pulsed-MT have been estimated in vivo. With the estimated parameters numerical error simulations were performed to find the best off-resonance saturation frequency and amplitude for the acquisition of high-resolution fast BPF maps.

The results of the BSA-phantom and the post mortem measurements point out that the fast BPF is possible within a certain error-tolerance. For predicting the error of the fast BPF estimation it has been shown that the numerical error simulations are better suited than the proposed error model. However, the results of the in vivo measurements indicate an overestimation of the parameters compared to the reported values in the literature.

A likely explanation for the difference is that in our measurements the Magnetization Prepared 2 Rapid Acquisition Gradient Echoes (MP2RAGE) sequence was used instead of the variable flip angle (VFA) method for the T_1-mapping. The VFA could bias the solution of the BPF estimation due to the short repetition rate of the sequence, which may result in a bias of the relaxation time $T_{1,obs}$. Therefore further research is necessary to study the influence of different T_1-mapping techniques on the fast BPF estimation.

Keywords: Magnetization Transfer, quantitative MRI, two-pool model, Multiple sclerosis, Myelin

Kurzfassung

Der Anteil an gebunden Protonen ist ein quantitativer Magnetisierunstransfer- (MT) Parameter, der klinisch als Biomarker für die Myelindichte relevant ist. Daher lassen sich mit diesem Parameter Änderungen der Myelindichte quantifizieren, welche typischerweise bei neurodegenerativen Erkrankungen wie bei der Multiplen Sklerose (MS) auftreten. Alle der bisher vorgestellten Methoden haben den Nachteil einer im klinischen Betrieb unzumutbaren Scanzeit für hochaufgelöste Bilder. Ein Ansatz, der dieses Problem zu lösen scheint, basiert auf der Reduktion der Parameter des gepulsten-MT Models, welcher die schnelle Bestimmung des gebunden Protonenpools mittels einer off-resonance Messung ermöglicht. In der vorliegenden Diplomarbeit wurde diese Methode implementiert und mit den Ergebnissen des gepulsten MT-Modells und numerischen Simulationen verglichen.
Der erste Teil der Arbeit bestand darin das gepulste MT-Modell mit den gekoppelten Bloch-Gleichungen zu vergleichen. Des Weiteren wurde ein neues numerisches Fehlermodell für die schnelle Messung des gebundenen Protonenpools entwickelt, welches den Bias und den durch das Rauschen verursachten Fehler abschätzt.
Im zweiten Teil der Arbeit wurden für verschiedene Konzentration von Rinderalbumin (BSA) und eines post mortem Gehirns die besten Parameterwerte für die schnelle Bestimmung des gebunden Protonenpools bestimmt. Danach wurde der gebunden Protonpool mit Hilfe der schnellen Methode bestimmt.
Im letzten Schritt wurden die Modellparameter des gepulsten MT-Modells in vivo bestimmt, welche dann verwendet wurden um den besten Abtastpunkt für die schnelle Bestimmung des gebunden Protonenpool zu ermitteln. Im Anschluss wurden hochaufgelöste Maps des gebundenen Protonenpools aufgenommen und berechnet.
Die Resultate der BSA und post mortem Messungen zeigen, dass die schnelle Bestimmung des gebunden Protonenpools mit gewissen Fehlerschranken möglich ist. Es wurde nachgewiesen, dass das numerische Fehlermodell besser geeignet ist den Fehler der schnellen Bestimmung zu ermitteln als das existierende Fehlermodell. Im Vergleich zur Literatur ist auffällig, dass die ermittelten in vivo Werte erhöht sind.
Eine mögliche Erklärung ist, dass in dieser Arbeit anstelle der Variable Flip Angle (VFA) Methode die Magnetization Prepared 2 Rapid Acquisition Gradient Echoes (MP2RAGE) Sequenz zur Bestimmung der T_1-map verwendet wurde. Die VFA könnte das Ergebnis des gebunden Protonenpools verfälschen, da es aufgrund der kurzen Repetitionszeit zu einem Fehler in der Bestimmung von $T_{1,obs}$ kommen kann. Folglich scheint es notwendig den Einfluss von unterschiedlichen T_1-mapping Methoden auf die Bestimmung des gebunden Protonenpools in zukünftigen Arbeiten zu ermitteln.

Schlüsselwörter: Magnetisierungstransfer, quantitatives MRT, Austauschmodell, Multiple Sklerose, Myelin

Danksagung

An erster Stelle richtet sich mein Dank an meine Familie und ganz besonders an meinen Eltern Gertraud und Friedrich die mich während meiner gesamten Studienzeit tatkräftig unterstützt haben.
Außerdem möchte ich Herrn Assoz. Prof. DI Dr. Ropele danken, der mich auf das spannende Themengebiet des Magnetisierungstransfers aufmerksam machte, und mich bei meiner Arbeit fachlich und persönlich bestens betreut hat. Weiters möchte ich mich bei Herrn Univ. Prof. DI Dr. Stollberger für die Betreuung an der Technischen Universität Graz bedanken.
Darüber hinaus möchte ich mich bei allen Mitarbeitern der Neuroimaging Forschungsgruppe an der Medizinischen Universität Graz für die ständige Unterstützung bedanken. Davon möchte ich Herrn DI Pirpamer ganz besonders hervorheben, welcher immer ein offenes Ohr für meine Fragen hatte.
Eine wichtige Stütze während des Studiums waren und sind, neben meinen alten und neuen Mitbewohner der Rechbauer-WG auch meine StudienkollegInnen und FreundInnen Isabella, Alex, Matthias, Patrik und Stefan. Vielen Dank für die schöne Zeit!

Contents

1 Introduction

Magnetization transfer (MT) imaging is an essential magnetic resonance imaging (MRI) contrast that can enhance T_1-weighted imaging. With MT imaging it is possible to get information about protons that are bound to macromolecules, which are otherwise invisible in conventional MRI due to their short T_2 relaxation times [1]. A commonly used semi-quantitative parameter in MT imaging is the magnetization transfer ratio (MTR), which is the relative change between an image acquired without and with a MT-saturation pulse. due to the off-resonance saturation of the bound protons magnetization is transferred from the free to the bound protons resulting in a signal decrease of the free protons. It has been shown that the magnetization transfer ratio (MTR) decreases in experimental induced inflammation [2], as well as the MTR is affected by the myelin content in multiple sclerosis (MS) [3, 4], which makes the MTR a common marker by accepted neurological MRI studies. Besides MS, MT imaging can give an insight into the understanding of different neurodegnerative diseases, in particular Alzheimer's disease and Parkinson's disease [5]. Recently it has been shown that MT-imaging helps in the differentiation of brain tumors, and furthermore that it provides additional information of the tumors compared with conventional MRI techniques [6].

The MTR, however, has the limitation that it is a semi-quantitative parameter that depends on the MRI pulse sequence parameters and imaging hardware [7].

To address these problems various quantitative MT (qMT) techniques have been develop that are based on a two-pool model introduced by Henkelmann [8]. Similar to a chemical exchange model, the basic model consists of two pools, one pool for the tissue water protons and one for the bound protons. The first qMT-experiments were performed with continous wave (CW) radio frequency (RF) saturation of the bound protons [8]. For in vivo applications this MT-imaging approach is not suited because of its high power deposition [9]. To overcome this problem pulsed MT models [10–12] have been developed that replace the CW-irradiation by short RF-pulses and estimate the qMT parameters from the change in the steady-state magnetization. In this work two approaches are investigated in detail – the pulsed MT-model by Yarnykh and Yuan [13] and the fast bound pool frac-

tion estimation from a single off-resonance saturation frequency measurement [14]. Since for the parameter estimation of the pulsed MT-model long scan times are unavoidable, Yarnykh [14] constrained the parameters of the model resulting in one parameter instead of four.

This strong reduction of model parameters rises the question about the accuracy of this approach. So far only a little number of publications were found that have implemented this approach. Underhill et. al [15] validated the approach with in vivo rat brains in the presence of tumor with the result that the bound pool fraction from a single off-resonance saturation frequncy measurement is an indicator for the myelin density in white matter (WM) and grey matter (GM). It has also been reported that the fast bound pool fraction estimation is possible within the spinal cord [16] and recently the approrach was adapted for the human liver for the quantitative assessment of hepatic fibrosis with the finding that macromolecular proton fraction is in increased in hepatic fibrosis [17].

The main focus on this thesis was a detailed validation of the fast bound pool fraction estimation from a single off-resonance saturation frequncy measurement [14] by estimating the four two-pool model parameters of the pulsed MT-model [13]. Investigations that have been reported in the literature are based on in vivo data that have the obvious drawback of limited scan time. Here the approach was validated from BSA-phantom measurements with reference values of the two-pool model that were estimated as accurate as possible with gold-standard methods by fitting all four parameter of the two-pool model. Furthermore in this work qMT parameters of a unfixed fresh post mortem brain, which has not been reported elsewhere, were estimated. Then MRI-protocols were developed that allow the measurement of the qMT parameters and the fast bound pool fraction estimation from a single off-resonance measurement in vivo.

2 Background

This chapter provides a detailed overview of the theoretical background that was necessary to accomplish this thesis. In the first section the fundamentals of MT in the context of MRI are given, following a literature review of quantitative MT methods with special focus on off-resonance methods that are based on the two-pool model. Then the pulsed MT-model by Yarnykh and Yuan [13] is explained in detailed because it is the basis for the estimation of the bound pool fraction from a single off-resonance measurement [14]. Further, for this method several assumptions and constrain has been proposed by Yarnykh [14], which are explained in a separate section. In the last section MRI field correction sequences are summarized that are necessary for the fast bound pool fraction estimation.

2.1 Basics of MT

In clinical MRI techniques water protons are used for imaging since the human body consists mainly of water. Therefore protons are excited within an external magnetic field at their Lamor frequency. After excitation the induced, measured, signal depends on the transversal relaxation time (T2), and the longitudinal relaxation times (T_1) of the tissue. These protons are considered as free, or mobile, reflected by their relative long T2 (i.e. greater than 10 ms) which allows to image them.
However, in the human body there are not only mobile protons – there are also immobile protons that are bound to macromolecules. These motional restricted protons have a very short T2 (i.e. less than 1 ms), which makes them invisible in conventional MRI. But theses bound protons are coupled with the free protons due MT, and thus it is possible to achieve information about the bound protons by measuring the signal of the free protons. In Figure 2.1 the absorption line-shapes of the free and bound protons are illustrated. Because of the high mobility of the free protons, the absorption lines-shape has a narrow peak at their resonance frequency, ω_0. In contrast, the line-shape of the bound protons is much broader since the bound protons are less mobile.

When applying an off-resonant saturation pulse the bound protons are getting saturated. Through the saturation pulse the exchange rate of magnetization is not in equilibrium any more, resulting in a decrease of the signal of the free protons due MT. Hence, the signal of the free protons – which is measured on-resonant – provides indirect information about the bound protons.

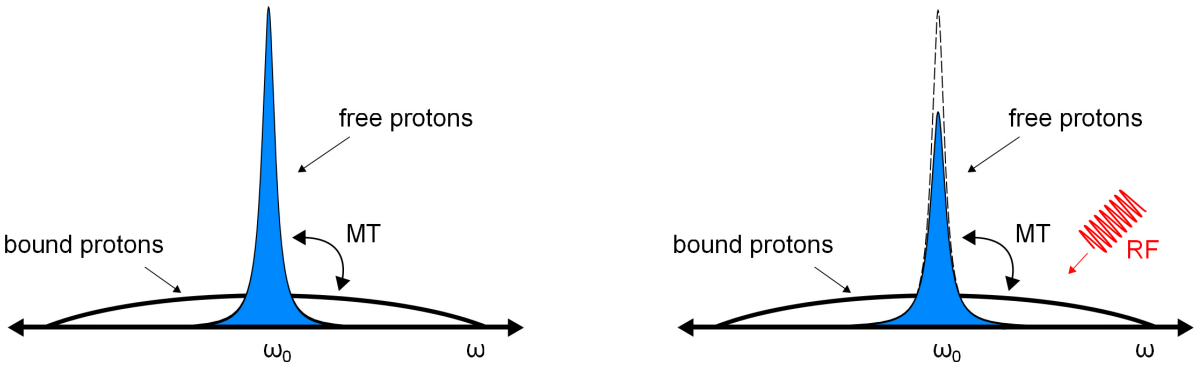

Figure 2.1: Schematic absorption line-shapes of the bound protons and the free protons. The free protons have their central peak at the Lamor frequency of protons ω_0, whereas the absorption shape of the bound protons extends over a wider range of frequencies. Through off-resonant RF irradiation the measured signal of the free protons decreases due MT.

2.1.1 Molecular Mechanism of MT

The molecular mechanism of MT are based on the nuclear Overhauser effect (NOE) and chemical exchange. In Figure 2.2 two models are illustrated that describe the transfer of magnetization from the macromolecule to the free bulk water [18]. It can be seen that the difference between these model is the pathway of the magnetization transfer from the bound protons of the macromolecule to the bulk water.

In the first model (a), the magnetization is transferred from the nonexchangeable proton to the hydration layer by NOE. Then, in the next step, the proton of the hydration layer exchanges rapidly with a proton of the bulk water.

By contrast, in model (b), the magnetization transfer has hydroxyl (OH), or amine groups (NH), involved that are bound to the macromolecule. In this model the magnetization is transferred to these groups by the NOE, and then, in next step the proton exchanges, again, rapidly with the free bulk water.

There is strong evidence that the exchangeable protons of the OH and NH groups are the main source for the contrast for MT weighted images in the brain. Investigations of

the proton exchange rates of OH and NH groups under physiological conditions showed that exchange rates are sufficient slow for the NOE with the nonexchangeable proton, and on the other hand, that the exchange rates are fast enough for the overall magnetization transfer [18]. This is in agreement with the experimental findings that the MT between lipid membrane models and water depends on the presence of sites with exchangeable hydroxyl and amino protons [19]. Furthermore, in white matter the cholesterol content, and the content of other lipid molecules with OH and NH groups, is higher then in gray matter, which results in faster T_1 relaxation rates of water in white matter than in gray matter [20].

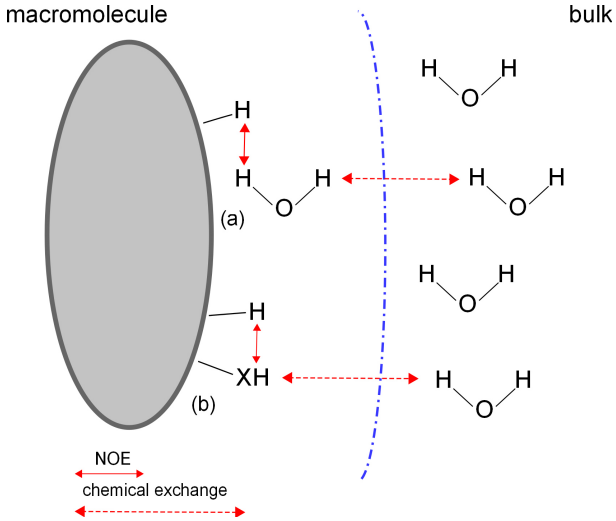

Figure 2.2: Two models for the exchange of magnetization between bound protons and free protons. In (a) the magnetization is transferred from the bound proton to the first hydration layer via NOE. Afterwards the proton of the hydration layer exchanges fast with the free bulk water. In model (b) magnetization is transferred from the nonexchangeable protons to exchangeable protons (X = O, N) due NOE. Then these protons exchange with the free bulk water. Adapted from [18].

2.1.2 Magnetization Transfer Ratio (MTR)

In classical MT-experiments so called Z-spectra are measured where the longitudinal magnetization is as a function of the off-resonance saturation frequency. An example of such a Z-spetrum is illustrated in Figure 2.3. The figure shows three curves where the solid line represents the actual measured relative longitudinal magnetization M with MT as a function of the off-resonance saturation frequency Δ. The dashed and dotted line are two theoretical curves that represent the relative longitudinal magnetization of the free/liquid pool and bound/macromolecular pool that would be achieved when the bound pool, or

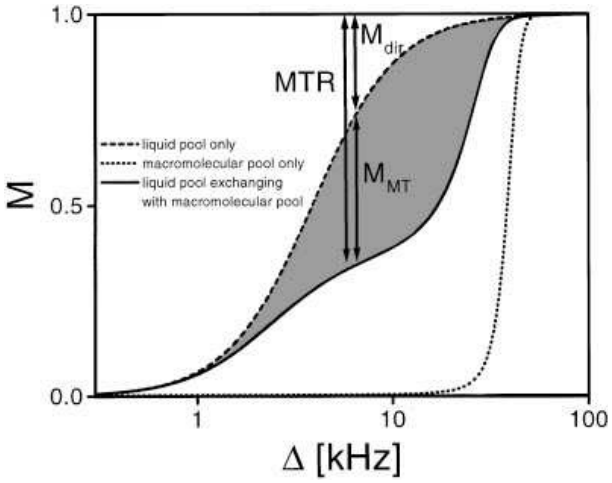

Figure 2.3: Example Z-spectrum which shows the longitudinal magnetization (solid line) and the theoretical longitudinal magnetization of the free pool (dashed line) and bound pool (dotted line) as a function of the off-resonance saturation frequency. (Adapted from [21])

the free pool, respectively, would be zero. Hence, these two curves show the spectra of the pools without MT.

Because the absorption line-shape of the free pool has a narrow peak around the Lamor-frequncy of protons, the magnetization is close to zero for small resonance offsets and increases with higher off-resonance frequencies. The effect of saturating the free pool due the off-resonance RF irradiation is called direct saturation. The dotted line shows the relative longitudinal magnetization of the bound pool that would be measured theoretically if the free pool would zero. Because of the broad absorption line-shape of the bound pool, the magnetization is saturated in a wide range.

The effect of the MT is indicated in the shaded area between the theoretical magnetization of the free pool and the measured magnetization. This area shows the decrease of the measured magnetization due MT.

One approach to describe the effect of MT semi-quantitatively is the magnetization transfer ratio (MTR):

$$MTR = \frac{M_0 - M_{sat}}{M_0} = 1 - \left(\frac{M_{dir}}{M_0} + \frac{M_{MT}}{M_0} \right) \tag{2.1}$$

The MTR is the normalized difference between the unsaturated signal M_0 and the saturated magnetization M_{sat} due to the off-resonance RF irradiation. In Figure 2.1 and Eqn. (2.1) can be seen that the saturated magnetization depends on both, the direct saturation of the free pool M_{dir}, and the actual M_{MT}. Hence, the image contrast in a MTR image

depends not only on the MT.
The advantage of the MTR is that it can be derived with little effort by measuring a reference image and a image with off-resonance saturation. The drawback of this method is that the ratio depends on the used pulse sequence and imaging hardware, which makes the application of this parameter only limited [7].

2.2 Quantitative MT

This section provides an overview of various quantitative MT methods that have been developed in the past 2 decades starting with the two-pool model for CW irradiation as an introduction, followed by pulsed MT-models, and in the last section on-resonance methods are described.

2.2.1 Two-Pool Model with CW Irradiation

This section gives an overview of the two-pool model that was introduced by Henkelman et al., in 1993, for the measurements of MT in agar gel [8]. Sincethen, several investigators have improved and simplified the two-pool model, but the key idea remains the same. Thus, this section aims to introduce the fundamental concept of the two-pool model and its limitations.
As illustrated in Figure 2.4 the model consists of a liquid pool A and a semi-solid pool B, which are also denoted in the literature as free and bound pool, respectively. The unshaded areas of each pool represent the available longitudinal magnetization M_z^a and M_z^b, and the shaded areas represents the magnetization that is not aligned longitudinally [8]. The rate of saturation due to RF-irradiation is given by R_{rfa} and R_{rfb} for each pool. The counterparts for the saturation rates are the relaxation rates R_a and R_b. The fully relaxed magnetizations is denoted with M_0^a and M_0^b, where M_0^a of the liquid pool is normalized to 1.
The exchange rate from one pool to the other is described by one constant, R. To calculate the exchange from pool A to B, and vice versa, R is multiplied by the magnetization of each pool. Hence, the exchange from A to B is RM_0^b, and for B to A it is RM_0^a, respectively.

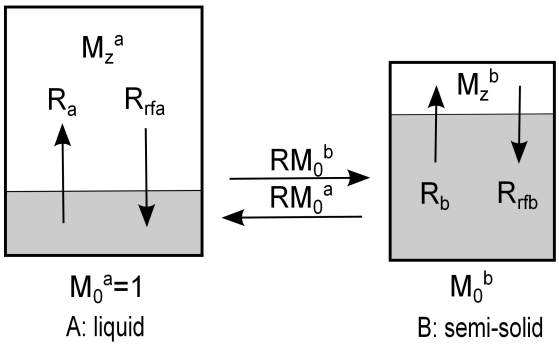

Figure 2.4: Two-pool model for the magnetization transfer. Pool A represents the liquid/free pool and pool B the semi-solid/bound pool with the available magnetization $M_z^a 0$ and M_z^b for each pool. The saturated magnetization due RF-irradiation is represented as shaded area with the saturation rates R_{rfa} and R_{rfb}. The relaxation rates are $R_{a,b}$, and the fully relaxed magnetizations are $M_0^{a,b}$. The exchange of magnetization between the pools is RM_0^b and RM_0^a. (Adapted from [8])

Mathematically the two-pool model is described with the coupled Bloch-equations Eqn. (2.2) that describe the evolving of the magnetization over time in the rotating frame of reference.

$$\begin{aligned}
\frac{dM_z^a}{dt} &= R_a(M_0^a - M_z^a) + \omega_1 M_y^a - RM_0^b M_z^a + RM_0^a M_z^b \\
\frac{dM_z^b}{dt} &= R_b(M_0^b - M_z^b) + \omega_1 M_y^b - RM_0^a M_z^b + RM_0^b M_z^a \\
\frac{dM_x^{a,b}}{dt} &= -\frac{M_x^{a,b}}{T_{2a,b}} - 2\pi\Delta M_y^{a,b} \\
\frac{dM_y^{a,b}}{dt} &= -\frac{M_y^{a,b}}{T_{2a,b}} + 2\pi\Delta M_x^{a,b} - \omega_1 M_z^{a,b}
\end{aligned} \tag{2.2}$$

In Eqn. (2.2), the evolving of the transverse magnetization is described by $M_x^{a,b}$ and $M_y^{a,b}$ for each pool. The frequency offset of the RF-irradiation is Δ, and its induced angular frequency is ω_1. The angular frequency is proportional to the amplitude of the pulse envelope of the RF-field since ω_1 is the gyromagnetic ratio γ, times the strength of the RF-field $|\mathbf{B_1}(\mathbf{t})|$.

The exchange of longitudinal magnetization due MT is highlighted in red and blue. Because of the short T2 of the semi-solid pool, the effect of transverse cross relaxation on MT is neglected. This was confirmed in simulations which included transverse cross re-

laxation [22].
In the experiments of Henkelman et. al [8] a CW saturation pulse was applied to saturate the semi-solid pool. The duration of the saturation pulse was sufficient long chosen, to guarantee, that the steady state of the agar sample was reached. Therefore the coupled Bloch-equations can be solved analytically by setting all six differential equations to zero. Doing so, one can solve the equations for the longitudinal magnetization of the liquid pool:

$$M_z^a = \frac{R_b R M_0^b + R_{rfb} R_a + R_b R_a + R_a R}{(R_a + R_{rfa} + R M_0^b)(R_b + R_{rfb} + R) - R M_0^b} \tag{2.3}$$

with absorption rates for each pool:

$$\begin{aligned} R_{rfa} &= \frac{\omega_1^2 T_{2a}}{1 + (2\pi \Delta T_{2a})^2} \\ R_{rfb} &= \frac{\omega_1^2 T_{2b}}{1 + (2\pi \Delta T_{2b})^2} \end{aligned} \tag{2.4}$$

Eqn. (2.3) has 6 model parameters ($R_a, T_{2a}, R_b, T_{2b}, R$ and M_0^b) that can not be fitted to experimental data [8, 23]. But Eqn. (2.4) can be approximated since $(2\pi \Delta T_{2a})^2 \gg 1$:

$$R_{rfa} = \frac{\omega_1^2 T_{2a}}{1 + (2\pi \Delta T_{2a})^2} \approx \frac{\omega_1^2 T_{2a}}{(2\pi \Delta T_{2a})^2} = \frac{\omega_1^2}{(2\pi \Delta)^2 T_{2a}} \tag{2.5}$$

Then, by diving Eqn. (2.3) by R_a, and substituting the approximation for the absorption rate R_{rfa}, the equation can be simplified to 5 five parameters:

$$M_z^a = \frac{R_b \frac{R M_0^b}{R_a} + R_{rfb} + R_b + R M_0^a}{\frac{R M_0^b}{R_a}(R_b + R_{rfb}) + \left(1 + \left[\frac{\omega_1}{2\pi \Delta}\right]^2 \left[\frac{1}{R_a T_2^a}\right]\right)(R_{rfb} + R_b + R M_0^a)} \tag{2.6}$$

With Eqn.(2.6) it is possible to fit the unknown five parameters ($R_b, T_{2b}, R, R M_0^b / R_a$ and $1/(R_a T_{2a})$) to the measured Z-sepctrum. However, the physical parameters can not be determined without information about the longitudinal relaxation rate of the free pool R_a [8]. To overcome these limitations an independent measurement of the observed relaxation rate R_{obs} is necessary. The observed relaxation rate is defined as the slow eigenvalue λ_2

of the solution of the coupled Bloch equations under free relaxation time intervals:

$$\begin{aligned}\frac{dM_z^a}{dt} &= R_a(M_0^a - M_z^a) - RM_0^bM_z^a + RM_0^aM_z^b \\ \frac{dM_z^b}{dt} &= R_b(M_0^b - M_z^b) - RM_0^aM_z^b + RM_0^bM_z^a\end{aligned} \tag{2.7}$$

where the solution for the longitudinal relaxation is biexponential with the two eigenvalues λ_1 and λ_2:

$$M_z^a(t) = C_1\mathrm{e}^{-\lambda_1 t} + C_2\mathrm{e}^{-\lambda_2 t} + M_0^a$$

$$\lambda_{1,2} = \frac{1}{2}\left([RM_0^b] + R_a + R + R_b \pm \sqrt{\left([RM_0^b] + R_a - R - R_b\right)^2 + 4R[RM_0^b]}\right) \tag{2.8}$$

$$R_{obs} = \lambda_2$$

Solving for R_a yields to:

$$\begin{aligned}R_a &= \frac{R_a^{obs}}{1 + \frac{\frac{[RM_0^b]}{R_a}(R_b - R_a^{obs})}{(R_b - R_a^{obs}) + R}} \\ &\approx \frac{R_a^{obs}}{1 + \frac{M_0^b}{R_a}(R_b - R_a^{obs})} \qquad R \gg (R_b - R_a^{obs})\end{aligned} \tag{2.9}$$

In the agar-gel experiments of Henkelman et al.[8] it was shown that the Lorentzian line-shape R_{rfb} of the semi-solid pool does not fit the data well. Alternatively a Gaussian line-shape instead of a Lorentzian was used. For tissues it was found that a super-Lorentzian [24], or a "flexible" line-shape [25], provides the best results.
The usage of CW-irradiation in MT is limited since most of the MRI-scanners are not designed for CW-irradiation, and also the specific absorption rate (SAR) for CW-experiments exceeds current limits [26].

2.2.2 Steady-State Pulsed MT-Models

To overcome the limitations of CW-irradiation pulsed MT-models were developed. Instead of CW-irradiation, short RF saturation pulses are applied with a certain pulse repetition rate until a pulsed steady state is reached. The advantage of this approach is that in the time interval between two pulses the imaging of the tissue can be accomplished (i.e. spoiling gradient, excitation pulse and readout gradient). A model by Graham and Henkelman [27] that describes the behaviour of the magnetization with pulsed saturation pulses is shown in Figure 2.5.

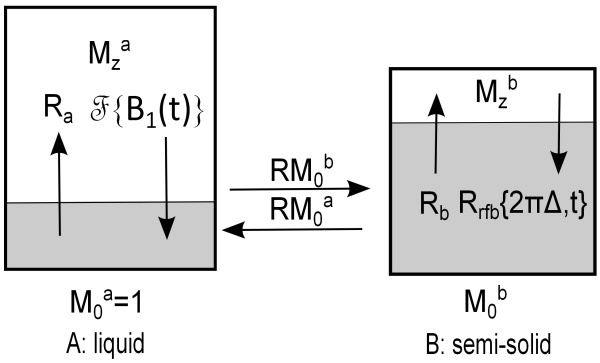

Figure 2.5: Modified two-pool model for the pulsed-MT. Pool A represents the liquid/free pool and pool B the semi-solid/bound pool with the available magnetization M_z^a and M_z^b for each pool. The saturated magnetization due RF-irradiation is represented as shaded area with the saturation rates $\mathcal{F}\{B_1(t)\}$ and $R_{rfb}\{2\pi\delta, t\}$. The relaxation rates are $R_{a,b}$, and the fully relaxed magnetizations are $M_0^{a,b}$. The exchange of magnetization between the pools is RM_0^b and RM_0^a. (Adapted from [27])

Basically the modified model that is presented in Fig 2.5 is quiet similar to model for CW-irradiation in Figure 2.4. However, there are two differences to the model for CW-irradiation. First, the induced angular frequency ω_1 is not constant over time anymore since the the pulse envelope of the RF-pulse varies over time ($|\mathbf{B_1}(\mathbf{t})| \neq const.$). For the pulsed MT, for example, a Gaussian pulse envelope can be used as pulse envelope and hence, the angular frequency is a function over time. Whereas in a CW-experiment the pulse envelope is a rectangular and therefore $|\mathbf{B_1}(\mathbf{t})| = const.$. Second, the saturation rate R_{rfb} has to be adapted because the Bloch-equations are only valid for a narrow-spectrum [27] and not a broad spectrum like the spectrum of the semi-solid pool. Thus, the absorption rate of the semi-solid pool is described by a time dependent saturation rate $R_{rfb}(2\pi\Delta, t)$.

In Eqn. (2.10) the modified coupled Bloch-equations for the pulsed-MT are shown, where the differences to the CW-saturation model are highlighted in blue.

$$\begin{aligned}
\frac{dM_z^a}{dt} &= R_a(M_0^a - M_z^a) + \omega_1(t)M_y^a - RM_0^bM_z^a + RM_0^aM_z^b \\
\frac{dM_z^b}{dt} &= R_b(M_0^b - M_z^b) - (R_{rfb}(2\pi\Delta, t) + RM_0^a)\, M_z^b + RM_0^bM_z^a \\
\frac{dM_x^a}{dt} &= -\frac{M_x^a}{T_{2a}} - 2\pi\Delta M_y^a \\
\frac{dM_y^a}{dt} &= -\frac{M_y^a}{T_{2a}} + 2\pi\Delta M_x^a - \omega_1(t)M_z^b
\end{aligned} \tag{2.10}$$

For these equations no analytic solution exists, and therefore they must be solved numerically [27]. However, there have been various numerical approximation derived [10–12] that are all based on the here presented two-pool model.
The approach of Ramani et al. [12] replaces the time dependent amplitude of the RF-pulse $\omega_1(t)$, with a "continuous wave power equivalent", ω_{1CWPE}. Therefore the amplitude of the RF-pulse is replaced by its root man square $\sqrt{P_{SAT}}$, averaged over time T_R':

$$\omega_{CWPE} = \gamma\sqrt{P_{SAT}} = \gamma B_{1CWPE} \tag{2.11}$$

For 2D multislice sequences T_R' is equal to the repetition time T_R divided by the number of slices acquired withing one T_R and for single slice and 3D sequence $T_R' = T_R$. With ω_{CWPE} the signal equation derived by Henkelman et al. [8] for a CW-saturation pulse can be rewritten by replacing ω_1 with ω_{CWPE}:

$$\begin{aligned}
S &= gM_Z^a \\
&= gM_0^a \left(\frac{R_b\frac{RM_0^b}{R_a} + R_{rfb} + R_b + RM_0^a}{\frac{RM_0^b}{R_a}(R_b + R_{rfb}) + \left(1 + \left[\frac{\omega_{CWPE}}{2\pi\Delta}\right]^2 \left[\frac{1}{R_aT_2^a}\right]\right)(R_{rfb} + R_b + RM_0^a)} \right)
\end{aligned} \tag{2.12}$$

where g is scaling factor, and compared to Henkelman et al. [8] the magnetization of the free pool M_0^a is not set to 1.
Instead of deriving an approximation for the whole pulse-sequence, Sled and Pike [10] split up the pulse sequence in three different parts that have a closed solution. In their approach the off-resonance pulse is approximated with a CW-irradiation for the restricted pool. Since the off-resonance pulse does not only influence the restricted pool, the effect of

saturating the free pool is modelled with an instantaneous saturation. In the remaining time the approximation for the two pools is free precession. In Figure 2.6 the pulsed MT-sequence with its approximations in the different time intervals is shown.

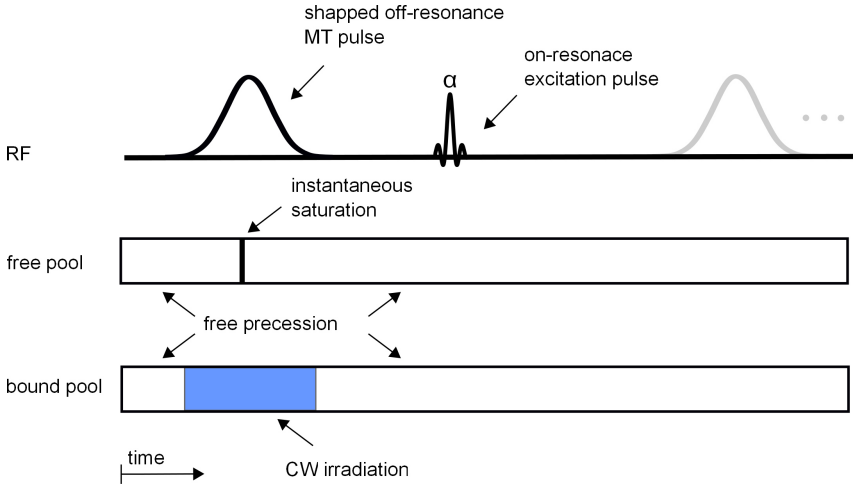

Figure 2.6: Approximation for the pulsed MT-model by Sled and Pike [10].The off-resonance pulse is modelled with CW-irradiation for the restricted pool and instantaneous saturation of the liquid pool. In the remaining time each pool is described by free precession.

The approximation of Yarnkyh [13] divides also the pulse sequence in different time intervals, in which for each one, a closed solution exists. This approach is discussed in detail in Section 2.3 since it is the method that is implemented and evaluated in this thesis.

2.2.3 Transient Pulsed MT-Models

In 2003, Ropele et al. [28] proposed a new approach for estimating the bound pool fraction in tissues. The method is based on the biexponential decay of the longitudinal magnetization of the free pool that is derived from the coupled Bloch-equations. The eigenvalues for the biexponential deay are identical to the derived results of Henkelman [8] for the estimation of the longitudinal relaxation rate for the free pool R_1^F from Eqn. (2.8).
The idea is to label the spins of the free-pool, and due MT the labelled spins are exchanged with the bound pool resulting in a steady sate concentration of the labelled spins between the two pools. The labelling is performed with a stimulated echo sequence, where between the first and second excitation pulse a modulation gradient is turned on. Between the second and third excitation pulse is a mixing time, where the labelled spins exchange and T_1 relaxation occurs. After the third pulse, the spins are demodulated with the same gradient, and only the spins that have been initial modulated will contribute to the signal

of the stimulated echo.
Ropele et al. [28] presented two approaches for fitting the signal to the equation. The first one is based on several measurement with different mixing times, where signal equation for the biexponetial decay is fitted to the data. The second one is a fast two-point method that neglects the fast eigenvalue due the fast decay. Then the bound pool fraction is estimated from two-mixing times, where the second mixing time has an 180° inversion pulse included.
The method by Ropele et al. [28] has the restriction that it is implemented for single-slice acquisition, and further that it is sensitive to B_1 inhomogeneities. In 2011, Soellinger et al. [29] extended the method of Ropele et al. by an interleaved, multislice, single-shot echo planar readout (sshEPI). The advantage of this method is that it is possible to acquire whole brain bound pool fraction map, and an apparent T_1 map, within 10-15 min.
The advantage of the STEAM approaches are the low SAR values since there is no off-resonance pulse needed. Furthermore, there is no additional information necessary compared with the previous described methods with off-resonance saturation because all these methods need at least a measurement for the observed relaxation rate to estimate parameters of the two-pool model.
Besides the STEAM approach there are different approaches that are using the biexponential relaxation [30–33]. In 2003, a method modified IR sequence by Gochberg [32] with EPI has been presented. Therefore several inversion recovery measurements with a 1.5ms, 180°, rectangular inversion pulse at different inversion times are acquired to estimate the parameters by fitting the equation for the biexponential relaxation. The first clinical implementation has been desriebd in 2011 with a selective IR (SIR) pulse sequence with an fast spin echo (FSE) readout and reduced TR [33]. Similar to the above introduced STEAM approaches, the IR approaches have the advantage that no B_0-, B_1- and T_1-map is needed compared to the pulsed MT-models and that the SAR is lower. However, one limimations is that scan time is high with 4 min for one slice [33].
The are also two others methods for the parameter estimation of the two-pool model that are based on balanced steady state free precession (bSSFP), and nonbalanced SSFP.
The standard signal equations for the balanced, and unbalanced, SSFP do not include MT. However, in 2008, Gloor et al. [34] derived a signal equation for the bSSFP that incorporates the coupled Bloch-equations for MT, into the deviation of the bSSFP signal equation. With this method it is possible to estimate the relaxation rates of the free pool (T_1^F and T_2^F), the fractional pool size ($\frac{M_0^B}{M_0^F}$), and the forward exchange rate (k), by fitting the data of several bSSFP measurements with different repetition rate T_R.
In 2010, Gloor et al. [35] extended the principal of the bSSFP for the nonbalanced SSFP,

and derived a signal equation for the SSFP-FID including the two-pool model. In contrast to the bSSFP, the nonbalanced has the advantage that it is not prone to susceptibility, but on the other hand it is sensitive to motion artefacts.

2.3 Pulsed MT-Model by Yarnykh and Yuan

In this Section a detailed description of the approximation for the pulsed-MT two pool model by Yarnykh and Yuan [13] is given. In the beginning the pulsed MT-model is explained, following a deviation of the signal equation. Furthermore, the approach for measuring the bound pool fraction from a signal off-resonance measurement is discussed [14].

2.3.1 Overview of the Model

The proposed model of Yarnykh and Yuan [13] for the pulsed-MT is shown in Figure 2.7. It can be seen that the notations compared to Henkelman and Graham [27] are slightly different. Yarnkyh [11] introduced two new parameters, the molar fraction f of the bound spins, and the effective cross-relaxation rate k, which are derived from the parameters of Graham and Henkelman [27]. Another difference is that Yarnykh describes the saturation rate of the free pool with W^F, and for the bound pool with W^B.
In Table 2.1 the notations of Yarnykh [11] are compared with the one of Graham and Henkelman [27].

Table 2.1: Overview of the notations of Graham and Henkelman [27] and Yarnyk [11] for the pulsed-MT two-pool model.

Description	Henkelman	Yarnykh
Abbreviation free pool	A	F
Abbreviation bound pool	B	B
Molar fraction of bound spins	$\frac{M_0^B}{M_0^A+M_0^B}$	f
Molar fraction of free spins	$\frac{M_0^A}{M_0^A+M_0^B}$	1 - f
Exchange rate	R	M_0^B/k
Exchange rate from free to bound pool	RM_0^B	k
Exchange rate from bound to free pool	RM_0^A	k(1-f)/f
Saturation rate free pool	R_{rfa}	W^F
Saturation rate bound pool	R_{rfb}	W^B

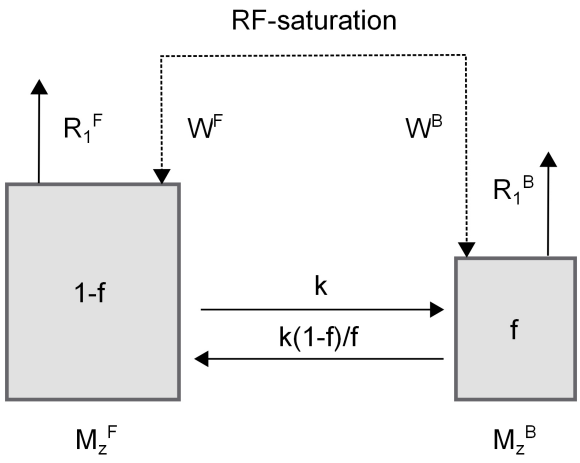

Figure 2.7: Two-pool model of Yarnykh and Yuan [13] for the pulsed-MT with direct saturation. The free pool is on the left hand side (denoted with F) and the bound pool on the right hand side (denoted with B) where f is the fraction of bound spins. The available longitudinal magnetization is M_z^F and M_z^B, and the relaxation rates of the pools are R_1^F and R_1^F. The influence of RF-saturation is modelled with the saturation rates W^F and W^B. The exchange from the free to the bound pool is k and in the opposite direction it is k(1-f)/f.

2.3.2 MRI-Sequence

The pulse sequence that is used by Yarnykh [14] for the MT-imaging is shown in Figure 2.8. It consists basically of two parts, the off-resonance saturation pulse, and a 3D SPGRE (spoiled gradient echo) imaging sequence. For the off-resonance saturation pulse a single-lobe sinc with gaussian apodization was applied in the experiments of Yarnykh [14].
Gradient echo sequences are fast imaging sequences that use low-flip angles, and instead of forming a spin echo with a 180° refocusing pulse, a gradient echo is used. The first gradient echo sequences was published by Haase et al. [36] and its abbreviation is FLASH (fast low-angle shot). Because of the low-flip angle it is possible to decrease the repetition rate since the majority of the longitudinal magnetization stays unaffected by the excitation pulse [36]. Therefore it is possible to start the next excitation immediately after the readout gradient. The spoiled GRE, or spoiled FLASH, has a spoiling gradient included, which destroys the transverse magnetization, and due to that, the contrast in spoiled GRE is mainly T_1-weighted.
The difference between a 2D and 3D sequence is that the slice selective excitation pulse is replace by an nonselective excitation pulse where the whole volume is excited, and after the excitation pulse, an additional encoding gradient in z-direction is placed for the slice selection. 3D sequences have the advantage that due the additional encoding in

z-direction the resolution is isotropic.

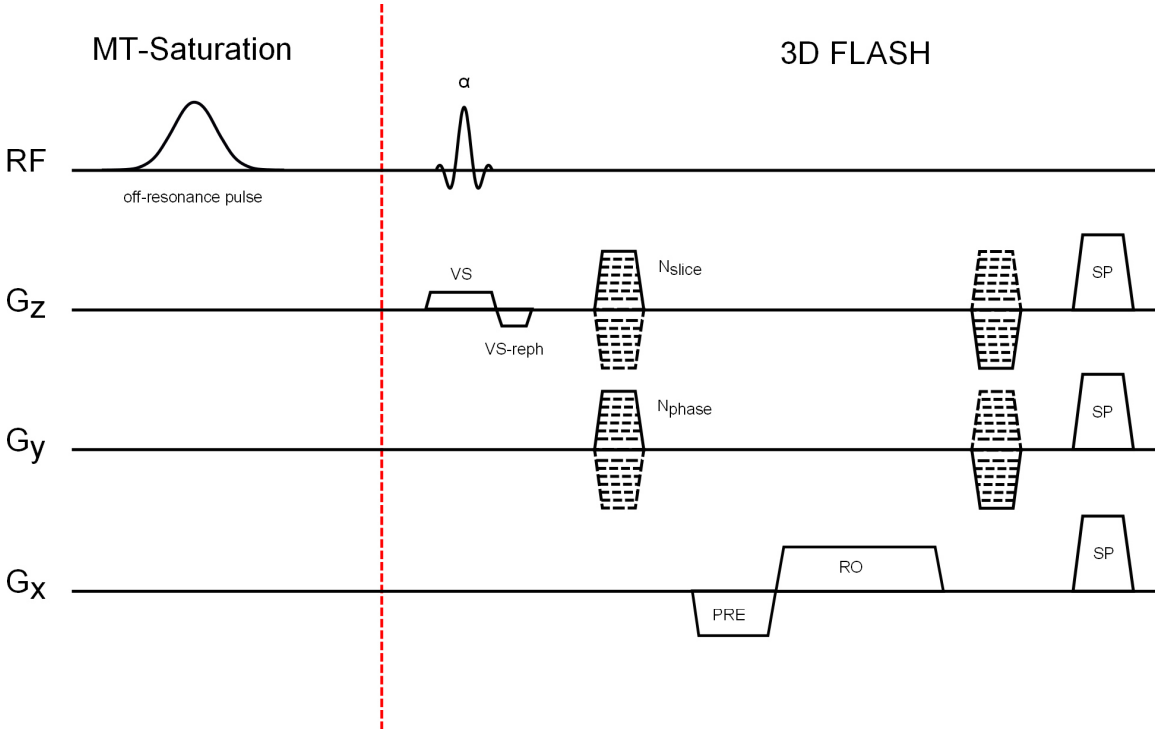

Figure 2.8: 3D FLASH sequence with MT off-resonance saturation pulse. RF: pulse timing, $G_{x,y,z}$: encoding gradients, VS: Volume selection, VS-reph: Rephasing gradient of volume selection, N_{slice}: N times slice encoding, N_{phase}: N times phase encoding, PRE: Prephasing before readout gradient, RO: Readout gradient, SP: Spoiling gradient.

2.3.3 Deviation of the Signal Equation

The signal equation for the pulsed MT by Yarnykh and Yuan is based on an earlier model by Yarnyk [11], in 2002, which does not include effect of direct saturation since it assumes high off-resonance frequencies [11]. Whereas the later model by Yarnykh and Yuan [13] includes the direct saturation in the deviation of the steady state magnetization.
For the model in Figure 2.7 the modified coupled Bloch-equations, in the rotating frame of reference, are:

$$\begin{aligned}
\frac{dM_x^F}{dt} &= -\frac{M_x^F}{T_2^F} - 2\pi\Delta M_y^F \\
\frac{dM_y^F}{dt} &= 2\pi\Delta M_x^F - \frac{M_y^F}{T_2^F} - \gamma B_1(t) M_z^F \\
\frac{dM_z^F}{dt} &= \gamma B_1(t) M_y^F - (R_1^F + k) M_z^F + \frac{k(1-f)}{f} M_z^B + R_1^F (1-f) \\
\frac{dM_z^B}{dt} &= -R_1^B M_z^B - \frac{k(1-f)}{f} M_z^B - W^B M_z^B + k M_z^F + R_1^B f
\end{aligned} \tag{2.13}$$

In Figure 2.9 the time intervals for the RF-pulses of the spoiled gradient echo pulse sequence (GRE) are shown. The concept for solving the coupled Bloch equations (2.13) is similar to the one proposed by Sled and Pike [9], where an approximated solution for different time intervals within the pulsed steady state is derived.
Yarnyk [11] divides the pulse sequence into the following four intervals: off-resonance pulse with duration t_m, delay t_s for the excitation pulse α, the excitation pulse itself, and delay for signal readout t_r.

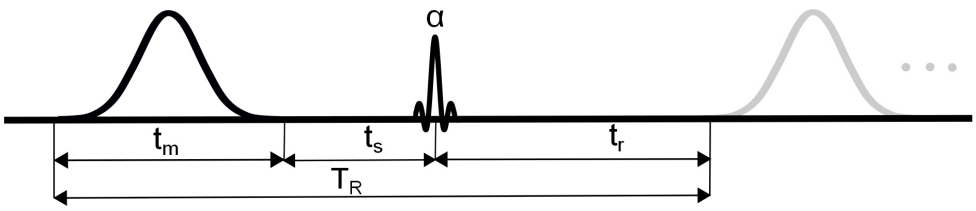

Figure 2.9: Timing of the RF-pulse for the pulse sequence of Yarnykh [13]. It is divided in four different time intervals. Saturation pulse with time t_m, delay t_s for excitation pulse α, excitation pulse, and delay for the signal readout and relaxation t_r.

For the approximation of the modified coupled Bloch equations (2.13) the analysis is restricted to the evolving of the longitudinal magnetization. Therefore, the longitudinal magnetization of the free pool M_{zi}^F, and the bound pool M_{zi}^B, is described by a 2x1 vector at the end of each time interval:

$$\mathbf{M}_i = \begin{bmatrix} M_{zi}^F \\ M_{zi}^B \end{bmatrix} \quad with \quad i = m, s, p, r \tag{2.14}$$

where the indices m,s, and r denote the time intervals in Figure 2.9 and p denotes the excitation pulse.

Approximation of the saturation pulse: To find an approximated solution for the modified coupled Bloch equations Yarnykh [11] proposed to replace the time varying RF amplitude, $B_1(t)$, by its root-mean-square value:

$$B_{1rms} = \left(\frac{1}{t_m} \int_0^{tm} B_1^2(t)\ dt \right)^{1/2} \tag{2.15}$$

Since the RF amplitude is now constant over time the saturation rates for the free and bound pool are also constant:

$$\begin{aligned} W^{F,B} &= \pi\ \gamma\ B_{1rms}\ g^{F,B}(\Delta, T_2^{F,B}) \\ &= \pi\ \omega_{1rms}\ g^{F,B}(\Delta, T_2^{F,B}) \end{aligned} \tag{2.16}$$

The absorption line shape of the free pool g^F is a Lorentzian that is described in Eqn. (2.5), and the absorption line shape of the bound pool g^B is a super-Lorentzian function:

$$g^B(2\pi\Delta, T_2^B) = \int_0^{\frac{\pi}{2}} \sin(\theta) \frac{2}{\pi} \frac{T_2^B}{|3\ \cos(\theta)^2 - 1|}\ exp\left(-2 \left[\frac{2\pi\Delta T_2^B}{|3\ \cos(\theta)^2 - 1|} \right]^2 \right) d\theta \tag{2.17}$$

If the pulse duration $t_m \gg \frac{1}{\Delta}$ the transverse components of the free pool contain fast-evolving terms, and therefore they can be set zero [13]. Incorporating the saturation rate of the free pool into the modified-Bloch equations (2.13), and neglecting the transverse components of the free pool, one can describe evolving of the longitudinal magnetization

as followed:

$$\begin{aligned}\frac{dM_z^F}{dt} &= -W^F M_y^F - (R_1^F + k)M_z^F + \frac{k(1-f)}{f}M_z^B + R_1^F(1-f) \\ \frac{dM_z^B}{dt} &= -R_1^B M_z^B - \frac{k(1-f)}{f}M_z^B - W^B M_z^B + kM_z^F + R_1^B f\end{aligned} \tag{2.18}$$

Or rewritten in matrix form:

$$\frac{d\mathbf{M_z}}{dt} = (\mathbf{R} + \mathbf{W})\mathbf{M_z} + \begin{bmatrix} R_1^F \\ R_1^B \end{bmatrix} \mathbf{M_{eq}} \tag{2.19}$$

where $\mathbf{R}$ is the relaxation matrix, $\mathbf{W}$ the saturation matrix, and $\mathbf{M_{eq}}$ the equilibrium magnetization:

$$\mathbf{R} = \begin{bmatrix} -R_1^F - k & \frac{k(1-f)}{f} \\ k & -R_1^B - \frac{k(1-f)}{f} \end{bmatrix} \tag{2.20}$$

$$\mathbf{W} = \begin{bmatrix} -W^F & 0 \\ 0 & -W^B \end{bmatrix} \tag{2.21}$$

$$\mathbf{Meq} = \begin{bmatrix} 1-f \\ f \end{bmatrix} \tag{2.22}$$

The differential equations (2.19) have the same form as:

$$\frac{d\mathbf{M}}{dt} = \mathbf{AM} + \mathbf{BM_0} \tag{2.23}$$

When a steady state solution of Eqn. (2.23) exists, these equations have an analytic solution:

$$\mathbf{M}(t) = \mathrm{e}^{\mathbf{A}t}\mathbf{M}(0) + [\mathbf{I} - \mathrm{e}^{\mathbf{A}t}]\mathbf{M}_{ss} \tag{2.24}$$

where $e^{\mathbf{A}t}$ is the matrix exponential, $\mathbf{M}(0)$ the initial value, and $\mathbf{M}_{ss}$ the steady state value. Substituting the matrix coefficient of Eqn. (2.19) into the solution of Eqn. (2.24) yields to:

$$\mathbf{M}_m(t) = e^{(\mathbf{R}+\mathbf{W})t}\mathbf{M}_r + [\mathbf{I} - e^{(\mathbf{R}+\mathbf{W})t}]\mathbf{M}_{ss} \tag{2.25}$$

To characterize the magnetization $\mathbf{M}_m(t)$ fully, the steady state magnetization $\mathbf{M}_{ss}$ has to be determined. The steady state magnetization is the magnetization that would be obtained when applying a RF-pulse with theoretically infinite duration. Therefore, all the derivatives in Eqn. (2.18) have to be zero to estimate the steady state magnetization:

$$\begin{aligned} 0 &= (\mathbf{R}+\mathbf{W})\mathbf{M}_{ss} + \begin{bmatrix} R_1^F(1-f) \\ R_1^B f \end{bmatrix} \\ \mathbf{M}_{ss} &= -(\mathbf{R}+\mathbf{W})^{-1} \begin{bmatrix} R_1^F(1-f) \\ R_1^B f \end{bmatrix} \end{aligned} \tag{2.26}$$

For a 2x2 matrix the inverse is:

$$(\mathbf{R}+\mathbf{W})^{-1} = \frac{1}{\det(\mathbf{R}+\mathbf{W})}\ \mathrm{adj}(\mathbf{R}+\mathbf{W}) \tag{2.27}$$

For the determinant and adjoint of the matrix follows:

$$\begin{aligned}
\det(\mathbf{R}+\mathbf{W}) &= \det\begin{bmatrix} -R_1^F - k - W^F & \frac{k(1-f)}{f} \\ k & -R_1^B - \frac{k(1-f)}{f} - W^B \end{bmatrix} \\
&= R_1^F R_1^B + R_1^F \frac{k(1-f)}{f} + R_1^F W^B + kR_1^B + \frac{k^2(1-f)}{f} \\
&+ kW^B + W^F R_1^B + W^F \frac{k(1-f)}{f} + W^F W^B - \frac{k^2(1-f)}{f} \\
&= A + (R_1^F + k)W^B + (R_1^B + \frac{k(1-f)}{f})W^F + W^F W^B \\
&= D
\end{aligned} \tag{2.28}$$

where A is the determinant of the relaxation matrix:

$$A = \det(\mathbf{R}) = R_1^F R_1^B + R_1^F \frac{k(1-f)}{f} + R_1^B k \tag{2.29}$$

Finally, for the steady state magnetization follows:

$$\begin{aligned}
\mathbf{M}_{ss} &= -(\mathbf{R}+\mathbf{W})^{-1}\begin{bmatrix} R_1^F(1-f) \\ R_1^B f \end{bmatrix} \\
&= -\frac{1}{D}\begin{bmatrix} -R_1^B - \frac{k(1-f)}{f} - W^B & -\frac{k(1-f)}{f} \\ -k & -R_1^F - k - W^F \end{bmatrix}\begin{bmatrix} R_1^F(1-f) \\ R_1^B f \end{bmatrix} \\
&= \frac{1}{D}\begin{bmatrix} (R_1^B + \frac{k(1-f)}{f} + W^B)R_1^F(1-f) + kR_1^B(1-f) \\ kR_1^F(1-f) + (R_1^F + k + W^F)R_1^B f \end{bmatrix} \\
&= \frac{1}{D}\begin{bmatrix} (1-f)(A + R_1^F W^B) \\ f(A + R_1^B W^F) \end{bmatrix}
\end{aligned} \tag{2.30}$$

Solution for non-irradiated time intervals: In the time-intervals without RF-irradiation the modified Bloch equations are easy to solve. There are two time-intervals without RF-irradiation of the spoiled GRE sequence. The first one is between the off-resonance saturation pulse and the readout pulse (t_s), and the second one is after the readout pulse and before the next saturation pulse (t_r). For these time intervals the modified Bloch-equations for the longitudinal magnetization simplify to:

$$\begin{aligned}
\frac{dM_z^F}{dt} &= -(R_1^F + k)M_z^F + \frac{k(1-f)}{f}M_z^B + R_1^F(1-f) \\
\frac{dM_z^B}{dt} &= -R_1^B M_z^B - \frac{k(1-f)}{f}M_z^B + kM_z^F + R_1^B f
\end{aligned} \tag{2.31}$$

With the same approach as for the saturation pulse, for the solution of the non-irradiated time intervals follows:

$$\mathbf{M}_{s,r} = \mathrm{e}^{\mathbf{R}t_{s,r}}\mathbf{M}_{m,p} + [\mathbf{I} - \mathrm{e}^{\mathbf{R}t_{s,r}}]\mathbf{M}_{eq} \tag{2.32}$$

Readout pulse: For the readout pulse it is assumed that it does not affect the bound

pool, and for the free pool it is described by the flip angle α:

$$\begin{aligned}\mathbf{M}_p &= \begin{bmatrix}\cos\alpha & 0\\ 0 & 1\end{bmatrix}\mathbf{M}_s \\ &= \mathbf{C}\mathbf{M}_s\end{aligned} \tag{2.33}$$

Pulsed steady state solution: With Equations (2.25), (2.32), and (2.33) every time-point of the spoiled GRE pulse sequence is defined. Furthermore, if the magnetization is in the pulsed steady state, Equation (2.34) must be satisfied:

$$\mathbf{M}(t) = \mathbf{M}(t + T_R) \tag{2.34}$$

where T_R is the repetition time of the pulse sequence. This condition is schematically illustrated in Figure 2.10 where the evolving of the approximated solution for the longitudinal magnetization of the liquid pool is shown.

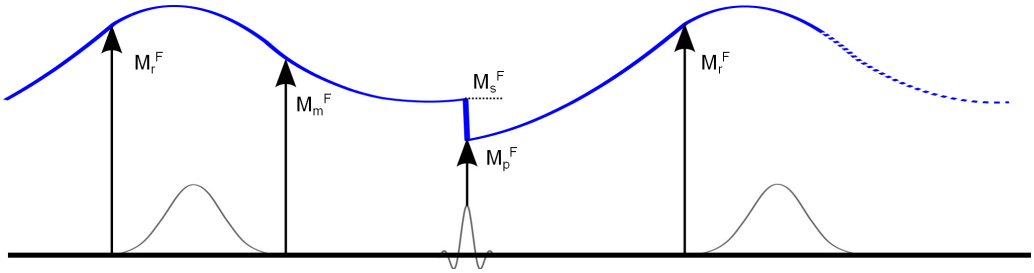

Figure 2.10: Schematic evolving of the liquid pool longitudinal magnetization with the approximation of Yarnykh and Yuan [13] in the pulsed steady state (blue line). The arrows indicate the end of the four time intervals defined in Figure 2.9.

With the condition that the pulsed steady state is reached it is possible to solve the equations for the magnetization $\mathbf{M_s}$ immediately before the readout pulse. To use the same formalism as Yarnykh and Yuan [13], the matrix exponentials are rewritten to: $\mathbf{E}_m = \exp((\mathbf{R} + \mathbf{W})t_m)$, $\mathbf{E}_s = \exp(\mathbf{R}t_s)$, and $\mathbf{E}_r = \exp(\mathbf{R}t_r)$.
The initial value of the relaxation in the time interval t_s is the magnetization M_m, at end

of the saturation pulse, and thus can be plugged into (2.32):

$$\begin{aligned}\mathbf{M}_s &= \mathbf{E}_s\mathbf{M}_m + (\mathbf{I} - \mathbf{E}_s) \\ &= \mathbf{E}_s[\mathbf{E}_m\mathbf{M}_r + (I - \mathbf{E}_m)\mathbf{M}_{ss}] + (\mathbf{I} - \mathbf{E}_s)\mathbf{M}_{eq}\end{aligned} \tag{2.35}$$

Plugging in the magnetization $\mathbf{M_r}$ after the delay t_r:

$$\mathbf{M}_s = \mathbf{E}_s[\mathbf{E}_m[\mathbf{E}_r\mathbf{M}_p + (\mathbf{I} - \mathbf{E}_r f)\mathbf{M}_{eq}] + (I - \mathbf{E}_m)\mathbf{M}_{ss}] + (\mathbf{I} - \mathbf{E}_s)\mathbf{M}_{eq} \tag{2.36}$$

Incorporating the rotation due the flip angle α yields to:

$$\mathbf{M}_s = \mathbf{E}_s[\mathbf{E}_m[\mathbf{E}_r\mathbf{C}\mathbf{M}_s + (\mathbf{I} - \mathbf{E}_r f)\mathbf{M}_{eq}] + (\mathbf{I} - \mathbf{E}_m)\mathbf{M}_{ss}] + (\mathbf{I} - \mathbf{E}_s)\mathbf{M}_{eq} \tag{2.37}$$

Solving Eqn. (2.39) for $\mathbf{M}_s$:

$$\mathbf{M}_s = \mathbf{E}_s\mathbf{E}_m\mathbf{E}_r\mathbf{C}\mathbf{M}_s + \mathbf{E}_s\mathbf{E}_m(\mathbf{I} - \mathbf{E}_r)\mathbf{M}_{eq} + \mathbf{E}_s(\mathbf{I} - \mathbf{E}_m)\mathbf{M}_{ss} + (\mathbf{I} - \mathbf{E}_s)\mathbf{M}_{eq}$$

$$(\mathbf{I} - \mathbf{E}_s\mathbf{E}_m\mathbf{E}_r\mathbf{C})\mathbf{M}_s = \mathbf{E}_s\mathbf{E}_m(\mathbf{I} - \mathbf{E}_r)\mathbf{M}_{eq} + \mathbf{E}_s(\mathbf{I} - \mathbf{E}_m)\mathbf{M}_{ss} + (\mathbf{I} - \mathbf{E}_s)\mathbf{M}_{eq} \tag{2.38}$$

$$\mathbf{M}_s = (\mathbf{I} - \mathbf{E}_s\mathbf{E}_m\mathbf{E}_r\mathbf{C})^{-1}\left(\mathbf{E}_s\mathbf{E}_m(\mathbf{I} - \mathbf{E}_r)\mathbf{M}_{eq} + \mathbf{E}_s(\mathbf{I} - \mathbf{E}_m)\mathbf{M}_{ss} + (\mathbf{I} - \mathbf{E}_s)\mathbf{M}_{eq}\right)$$

The final induced signal S_{MT} in the spoiled GRE is proportional to the longitudinal magnetization M_{zs}^F of Eqn. (2.38):

$$S_{MT} = M_0 M_{zs}^F exp(-TE/T_2^*)\sin\alpha \tag{2.39}$$

where M_0 is the equilibrium magnetization, T_E the echo time, α the flip angle, and the T_2^* decay.
To eliminate the influence of the unknown equilibrium magnetization and T_2^* a reference

scan is performed without RF-saturation:

$$m_z = \frac{S_{MT}}{S_{ref}} = \frac{M_0 M_{zs}^F(W^F(\Delta, FA_{MT}), W^B(\Delta, FA_{MT}) exp(-TE/T_2^*) \sin\alpha}{M_0 M_{zs}^F(W^F(\Delta = 0, FA_{MT} = 0), W^B(\Delta = 0, FA_{MT} = 0)) exp(-TE/T_2^*) \sin\alpha}$$

$$= \frac{M_{zs}^F(W^F(\Delta, FA_{MT}), W^B(\Delta, FA_{MT}))}{M_{zs}^F(W^F(\Delta = 0, FA_{MT} = 0), W^B(\Delta = 0, FA_{MT} = 0))} \tag{2.40}$$

2.4 Bound Pool Estimation from a Single Off-Resonance Measurement

In this work, so far, the pulsed-MT two-pool model by Yarnykh and Yuan [13] including the approximation for the signal equation has been described. With this approach it is possible to obtain the parameters of the two-pool model by fitting the data from several off-resonance measurements, and amplitudes of the RF-pulse, to Eqn. (2.39). However, in clinical practice this is not acceptable because of the too long scanning times.
In 2002, Yarnkyh proposed a first order approximation of Eqn. (2.39) with neglecting the direct saturation of the free pool reducing the unknown parameters to three [11]. Later, in 2012, Yarnykh [14] presented a method for estimating the bound pool fraction within an acquisition time of 10 min. For decreasing the scanning time that much, several assumption and constraints has been proposed, to estimate the bound pool fraction from a single off-resonance measurement and one reference scan without an off-resonance saturation pulse.

2.4.1 Assumptions and Constraints

Relaxation rates $\mathbf{R_1^F}$ and $\mathbf{R_1^B}$: Without any information about the relaxation rates R_1^F and R_1^B it is not possible to separate the cross-relaxation parameters f and k [14]. Therefore it is necessary to measure the observed relaxation rates R_1 in an independent measurement [8]. There are basically two approaches for estimating R_1^F and R_1^B. In the first one, the relaxation rates of the bound pool is set constant, $R_1^B = 1s^{-1}$ [8, 24], and in the second one all relaxation rates are set equal, $R_1 = R_1^B = R_1^F$ [13, 31]. The last assumption is used by Yarnykh for estimating the molar fraction f because it excludes the

question about the magnetic field dependency of R_1^B [14].

Transverse relaxation $\mathbf{T_2^B}$: In the literature only small variations of T_2^B for white matter, grey matter, and multiple sclerosis lesions, have been reported [13]. Therefore Yarnykh [14] assumed that T_2^B is constant for all brain tissues.

Transverse relaxation $\mathbf{T_2^F}$: Although the parameter T_2^F and R_1^F vary, the product is similar for different brain tissue [13], resulting in a constant product $T_2^F R_1^F$ as an approximation for T_2^F.

Forward rate constant k: By fixing the value of the reverse rate constant, from the bound to the free pool, it is possible to constrain k [15]:

$$R = k\frac{1-f}{f} \tag{2.41}$$

2.4.2 Sensitivity Analysis

Yarnkyh [14] also analysed the influence of the different parameters as a function of the off-resonance saturation frequency and the effective flip angle, to find the best sampling point, with the above explained assumptions and constraints. For that purpose a sensitivity analysis was carried out, where the influence of the parameters f, R, T_2^B, and T_2^F was examined from Z-spectra of white matter (WM), grey matter (GM) and MS-lesions. The relative sensitivity s for the normalized longitudinal magnetization m_z for each parameter is calculated as followed:

$$s = \frac{\delta m_z}{\delta p}\frac{p}{m_z}, \quad where \quad p \equiv f, R, T_2^F, T_2^B \tag{2.42}$$

The sensitivity analysis examines how a change of the input parameter affects the output of model. If s is small, the influence of the input parameter may be neglected since it does hardly affect the output, whereas a high s means, that the input parameter has a strong effect on the output.
As an example the sensitivity analyses of Yarnykh [14] for WM are shown in Figure 2.11. The fitted Z-spectra for different effective flip angle FA_{MT} are plotted in (a), and the results of the sensitivity analysis for the off-resonance saturation frequency Δ and FA_{MT} are shown in (b) and (c). Here only WM is shown because the tendency for the curves

for GM and MS is quiet similar.

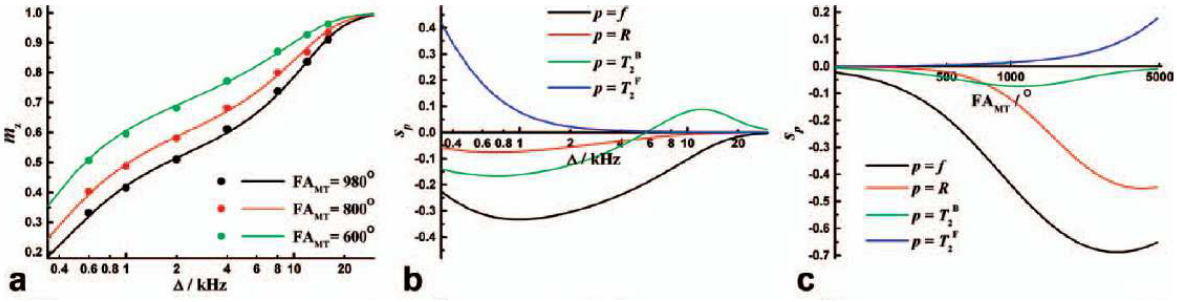

Figure 2.11: Sensitivity analysis of the pulsed Z-spectra at different effective flip angel FA_{MT}. (a) shows the pulsed Z-spectra for WM. The sensitivity analysis as function of the off-resonance saturation frequency Δ is plotted in (b), and of FA_{MT} in (c). Taken from [14].

.

As can be seen from Figure 2.11, the bound pool fraction has the largest sensitivity of all four parameters, whereas the reverse exchange rate R has a very small influence in a wide range of off-resonance frequencies. The sensitivity of T_2^F decreases exponential and is zero at off-resonance frequencies greater than 2kHz. T_2^B has one negative peak at about 600 Hz and a positive one at about 12kHz. Between these two points the zero-crossing is at around 5-6 kHz.

An important point resulting from the sensitivity analysis is that the above formulated constraints have only little influence on the result for off-resonance frequencies between 3 kHz to 6 kHz, and effective flip angle smaller than 1000°.

The sensitivity analysis can be used to formulate an optimization problem where the sensitivity of the bound pool fraction f is maximized, and the influence of the other parameters are minimized. Therefore Yarnykh [14] proposed an error model, which is briefly explained in the next section.

2.4.3 Error Model

The error model of Yarnykh [14] estimates the total error of f for the whole images. The standard deviation of the bound pool fraction σ_f is calculated in the model as follows:

$$\begin{aligned}\sigma_f &= \sum_{i=1}^{N}\sum_{j=1}^{N}\sum_{k=1}^{N} h_{i,j,k}\sigma_h(f, R_i, T_{2,j}^F, T_{2,k}^B) \\ &= \sum_{i=1}^{N}\sum_{j=1}^{N}\sum_{k=1}^{N} h_{i,j,k}(\sigma_{i,j,k}^2 + \beta_{i,j,k}^2)^{1/2}\end{aligned} \tag{2.43}$$

In this model there are two sources for the error in f; namely the errors due noise, which are described with $\sigma_{i,j,k}$, and a bias $\beta_{i,j,k}$ due constraining the remaining parameters, k, $T_{2,b}$ and $T_{2,f}$, of the two pool model. The indices denote the different combinations of parameters wit a total number N that are either measured, for example with a four point fit of several Z-spectra, or statisticaly description by parameter distributions. The weighting for each combination of parameters is accomplished by a multiplication of the two error terms with the joint distribution $h_{i,j,k}$. One way to estimate the joint distribution of the parameters is to multiply the estimated parameter histograms for each parameter. Therefore the error of different parameter combinations has not the same influence on the total error.
The bias due the constrained parameters is be estimated with an first order error approximation. Changes of the magnetization m_z due an error β of the bound pool fraction are described as:

$$\begin{aligned} m_z(f+\beta) &\approx m_z(f) + \frac{\partial m_z}{\partial f}\beta \\ m_z(f+\beta) - m_z(f) &\approx \frac{\partial m_z}{\partial f}\beta \\ \Delta m_z &\approx \frac{\partial m_z}{\partial f}\beta \\ \beta &\approx \left(\frac{\partial m_z}{\partial f}\right)^{-1}\Delta m_z \end{aligned} \tag{2.44}$$

Now the deviation of the magnetization Δm_z is estimated with an first order approxi-

mation:

$$\beta_{i,j,k} = \left(\frac{\partial m_z}{\partial f}\right)^{-1} \left(\frac{\partial m_z(f, R_i, T^F_{2,j}, T^B_{2,k})}{\partial R_i}\Delta R_i + \frac{\partial m_z(f, R_i, T^F_{2,j}, T^B_{2,k})}{\partial T^F_{2,j}}\Delta T^F_{2,j} + \frac{\partial m_z(f, R_i, T^F_{2,j}, T^B_{2,k})}{\partial T^B_{2,k}}\Delta T^B_{2,k}\right) \tag{2.45}$$

where ΔR_i, $\Delta T^F_{2,j}$, $\Delta T^B_{2,k}$ described the deviation from the constrained parameters. Since the noise affects the normalized signal m_z, the deviation Δm_z in Eqn. (2.44) has to be estimated. Assuming that the covariance of the noise in the reference image (S_{ref}) and in the MT weighted images (S_{MT}) is and that the standard deviation of the noise (σ_N) is equal in both images then, the deviation of the normalized magnetization can be described in terms of SNR_{ref} and m_z:

$$\begin{aligned}
\Delta m_z &= m_z \left(\left(\frac{\sigma_N}{S_{MT}}\right)^2 + \left(\frac{\sigma_N}{S_{ref}}\right)^2\right)^{1/2} = \left(\left(\frac{m_z\sigma_N}{S_{MT}}\right)^2 + \left(\frac{m_z\sigma_N}{S_{ref}}\right)^2\right)^{1/2} \\
&= \left(\left(\frac{m_z\sigma_N}{S_{MT}}\frac{S_{ref}}{S_{ref}}\right)^2 + \left(\frac{m_z}{SNR_{ref}}\right)^2\right)^{1/2} = \left(\left(\frac{1}{m_z}\right)^2 + \left(\frac{m_z}{SNR_{ref}}\right)^2\right)^{1/2} \\
&= \left(\frac{1+m_z^2}{SNR_{ref}}\right)^{1/2}
\end{aligned} \tag{2.46}$$

Now the final error due noise can be estimated by plugging in the results of Eqn. (2.46) in Eqn. (2.45):

$$\sigma_{i,j,k} = \left(\frac{\partial m_z(f, R_i, T^F_{2,j}, T^B_{2,k})}{\partial f}\right)^{-1} \frac{(1 + m_z(f, R_i, T^F_{2,j}, T^B_{2,k})^2)^{1/2}}{SNR_{ref}} \tag{2.47}$$

2.4.4 T_1-Mapping

As mentioned in Section 2.2 it is not possible to determine the two-pool parameters without an independent measurement of the observed relaxation time T_1.
The gold standard for estimating T_1 is based on an inversion recovery (IR). The sequence starts with an 180° RF-pulse that inverts the longitudinal magnetization. Then the mag-

netization recovers with the T_1-relaxation time and after the inversion time a 90° RF-pulse flips the magnetization into the transverse plane. By forming a spin echo with a 180° RF-pulse at $T_E/2$ the signal is measured [37].
If the repetition rate is sufficient long ($TR \geq 5T_1$), T_1 can be fitted by the following signal equation:

$$M(TI) = M_0(1 - \beta e^{-TI/T_1}) \tag{2.48}$$

where M_0 is the equilibrium magnetization, β the inversion factor, which is 2 for a perfect 180° inversion pulse, and TI the inversion time.
However, this method has the drawback that it is slow since fully recovery of the longitudinal magnetization ($TR \gg 5T_1$) is necessary for the validity of the signal equation. Instead of acquiring one sample with one inversion pulse, the Look-Locker sequence [38] uses one inversion pulse followed by train of RF-pulses with low-flip angle.
Another approach is the Magnetization Prepared 2 Rapid Acquisition Gradient Echoes (MP2RAGE) sequence [39]. The MP2RAGE can be split up into two MPRAGE [40] blocks, where each block consists of a GRE block with two different flip angles, α_1 and α_2. Before the first GE block a 180° inversion pulse is used to invert the magnetization. The inversion times, TI_1 and TI_2, are defined from the inversion pulse until the center of the k-space is acquired. TA is the delay until the start of the first gradient echo block, TB the delay until the second gradient echo block, and TC the time until the next repetition.

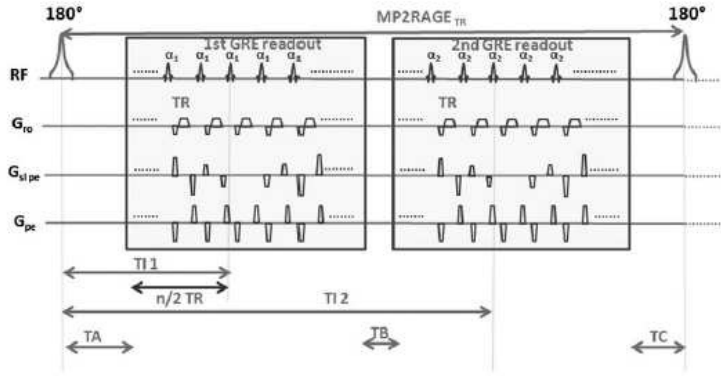

Figure 2.12: Sequence diagram of the MP2RAGE [39] sequence.

With two images, GRE_{TI1} and GRE_{TI2}, acquired at different inversion times the

MP2RAGE is calculate:

$$MP2RAGE = \frac{GRE_{TI1}GRE_{TI1}}{GRE^2_{TI1} + GRE^2_{TI2}} \tag{2.49}$$

which is ranging from -0.5 to 0.5. By using the signal equation of the MP2RAGE, which includes also the sequence parameters, a look-up table is generated that assigns a T_1-value to the MP2RAGE value [39]. The advantage of this method is that it eliminates the influence of the proton density M_0, T_2^*, and the receive B_1^- fields [39].
In the experiments of Yarnykh [14] the variable flip angle (VFA) method by Fame et al. [41] was implemented for estimating the T_1-Map.
The VFA method is based on a gradient echo sequence with variable flip angle α where T_1 is estimated by fitting the signal of different flip angles $I(\alpha)$ to Eqn. (2.50).

$$\frac{I(\alpha)}{\sin(\alpha)} = e^{-TR/T_1}\frac{I(\alpha)}{\tan(\alpha)} + N(H)(1 - e^{-TR/T_1})^{-TE/T2^*} \tag{2.50}$$

Since the additive term on the right hand side of Eqn. (2.50), with the factor N(H) that incorporates the relative proton density, the amplification factor and coil sensitivity, is constant for all measurement it is possible to estimate T_1 from several measurements with different flip angle.

2.5 Field Corrections for the Pulsed MT-Model

2.5.1 B_0-Mapping

A simple approach for the estimation of the B_0 field map is the dual phase difference method where two phase images with different echo times are acquired [42].
The phase shift ϕ for the two echoes, $T_{E,1}$ and $T_{E,2}$, is given by:

$$\begin{aligned}\phi_1 &= \phi_0 + \omega T_{E,1} \\ \phi_2 &= \phi_0 + \omega T_{E,2}\end{aligned} \tag{2.51}$$

where ϕ_0 is the initial phase shift. With the phase difference, $\Delta\phi = \phi_2 - \phi_1$, of the acquired phase images one can solve Eqn. (2.51) for the angular frequency ω:

$$\omega = \frac{\Delta\phi}{T_{E,2} - T_{E,1}} \tag{2.52}$$

If the time difference between the two echos is small enough, such that both phases are $< 2\pi$, the phase difference can be calculated with the two complex images I_1 and I_2:

$$\Delta\phi = \tan^{-1}\left(\frac{\mathbf{Im}\{I_1 I_2^*\}}{\mathbf{Re}\{I_1 I_2^*\}}\right) \tag{2.53}$$

2.5.2 B_1-Mapping

For a preciser estimation of the bound pool fraction from the pulsed MT-model knowledge of the actual flip angle is needed for the correction of the flip-angle in Eqn. (2.38), the correction of the saturation pulse amplitude, and for the correction of the VFA method for estimating T_1.
There have been several techniques proposed in the literature for B_1-mapping [43–46]. All these methods have in common that they acquire two images with different settings from which the B_1-map is estimated. The Double Angle Method (DAM) [43] for example uses two different excitations angles with a repetition, which is much more longer than the T_1-relaxation ($TR \geq 5T_1$), to guarantee that longest T_1 relaxation within the object is fully relaxed. With the constrain that $\alpha_2(\mathbf{x}) = 2\alpha_1(\mathbf{x})$, the flip angle $\alpha_1(\mathbf{x})$ can be derived

from the ratio of the two signal intensities. Doing so, one gets a solution for $\alpha_1(\mathbf{x})$:

$$\alpha_1(\mathbf{x}) = \arccos \frac{I_2(\mathbf{x})}{2I_1(\mathbf{x})} \tag{2.54}$$

The advantage of the DAM is that it excludes the influence of the coil sensitivity, spin density, and the T2 relaxation time, on the active B_{1+}-map [43].
In 2007, Yarnykh presented the actual flip angle imaging (AFI) pulse sequence that is based on two identical RF-pulses with different repetition rates TR_1 and TR_2 [45], which he is also using for the fast bound pool fraction estimation from a single off-resonance measurement [14]. The schematically timing of the RF-pulses, and the two signals S_1 and S_2, is illustrated in Figure 2.13. The signals S_1 and S_2 are measured with a gradient echo readout. After the repetition rates the transverse magnetization is destroyed with spoiling gradients after both repetition rates.

Figure 2.13: Timing of the two identical RF-pulses with flip angle α and repetition rates TR_1 and TR_2 for the AFI method. S_1 and S_2 are the measured signal with gradient echo readout. Adapted from [45].

The actual flip-angle is derived from the pulsed-steady state signal and therefore the repetition rates have to be smaller than the T_1 relaxation rate ($TR_1 < TR_2 < T_1$) to achieve a pulsed steady state signal. Then an approximation for the actual flip-angle can be derived from the ratio of the signal intensities (r = S2/S1) and the ratio of the ratio of the repetition rates (n = TR_1/TR_2):

$$\alpha \approx \arccos \frac{rn - 1}{n - r} \tag{2.55}$$

An excellent comparison between the most prominent techniques can be found in [47].

3 Methods

This chapter is divided into five Sections that describe the simulations and measurements that were performed in this thesis. The first section describes the general implementation of the pulsed-MT model and the simulations that were carried out to validate the model. Further it describes how the parameter estimation of the pulsed-MT model was performed. The next section deals with the errors that arise with fast bound pool fraction estimation from one single off-resonance measurement [14]. Therefore a numerical error model is introduced, and compared with the error-model proposed by Yarnyh [14].
The last three sections explain the steps for the practical implementation of Yarnykh's approach [14] on the MRI scanner and its validation. First, the methods for the BSA phantom measurements are described, then the post mortem measurements, and in the last section the methods for the in vivo measurements are described.

3.1 General Implementations and Simulations

3.1.1 Coupled Bloch Equations and the Pulsed MT-Model

Coupled Bloch Equations

For the validation of the approximation of the pulsed-MT model by Yarnykh and Yuan [14], the coupled Bloch equations (2.13) were solved iteratively with Matlab (Mathworks Inc., Natick, USA) until the pulsed-steady was reached for the FLASH sequence with MT saturation. As solver, the ODE45 function of Matlab for nonstiff differential equations was chosen.
Similar to the deviation of the approximated equation for the pulsed-MT model the pulse sequence is divided into four parts, where for each part the solution of the coupled Bloch equations is estimated numerical. In Figure 3.1 a flow-chart of the implementation is illustrated.
The simulation starts with the equilibrium magnetization M_{eq} as initial value. During the

RF-saturation pulse, for each iteration of the solver, the values of the RF-pulse envelope $B_1(t)$ in Eqn. (2.13) has to be updated. Therefore, a separate function was implemented that returns the amplitude for that specific pulse envelope (i.e. a gaussian envelope). Furthermore, for estimating the absorption rate W^B of the bound pool the value of the super-Lorentzian function $g(\Delta, T_2^b)$ is determined by a separate function that solves the integral in Eqn. (2.17) numerical with the trapezoidal method, trapz(), in Matlab.
In the time interval t_s, before rotating the magnetization with the excitation RF pulse α, the coupled Bloch equations are simplified since $B_1(t) = 0$ (free precession). Hence, only cross-relaxation occurs according to the analytic solution of Eqn. (2.32). After the excitation RF pulse the same function is again used.
The effect of the excitation RF pulse is modelled by rotating the longitudinal magnetization of the free pool with the flip angle α. For the bound pool it is assumed that the excitation RF pulse does not affect the magnetization. Therefore, the readout pulse for the longitudinal magnetization is described by the matrix $\mathbf{C}$ in Eqn. (2.33).
The spoiling of the transverse magnetization is implemented by setting it to zero, before each saturation pulse and the readout pulse. To guarantee that the pulsed-steady is reached the simulations were carried out until the deviation of the current magnetization before the readout $M_{s,\,i}$, and before the last readout $M_{s,\,i-1}$, was smaller than 10^{-4}.

Approximated pulsed MT-Model

The approximations for the pulsed MT-model by Yarnykh and Yuan [13] were implemented in two different ways.
First, the approximated signal equation (2.38) was used to calculated the longitudinal magnetization immediately before the readout pulse in the pulsed steady state.
Second, similar to the numerical implementation of the coupled Bloch equations, also the approximated solution for the different time intervals was calculated in a function until the pulsed steady-state was reached. The second approach was used to verify the solution of Eqn. (2.38), and furthermore, to compare the agreement with the solution of the numerical implementation of the coupled Bloch equations at any point in time of the pulse sequence.

Validation of the pulsed MT-model

To validate the approximations of the pulsed MT-model by Yarnykh and Yuan [13] several simulations with different parameters of the two-pool model, and parameters of the pulse

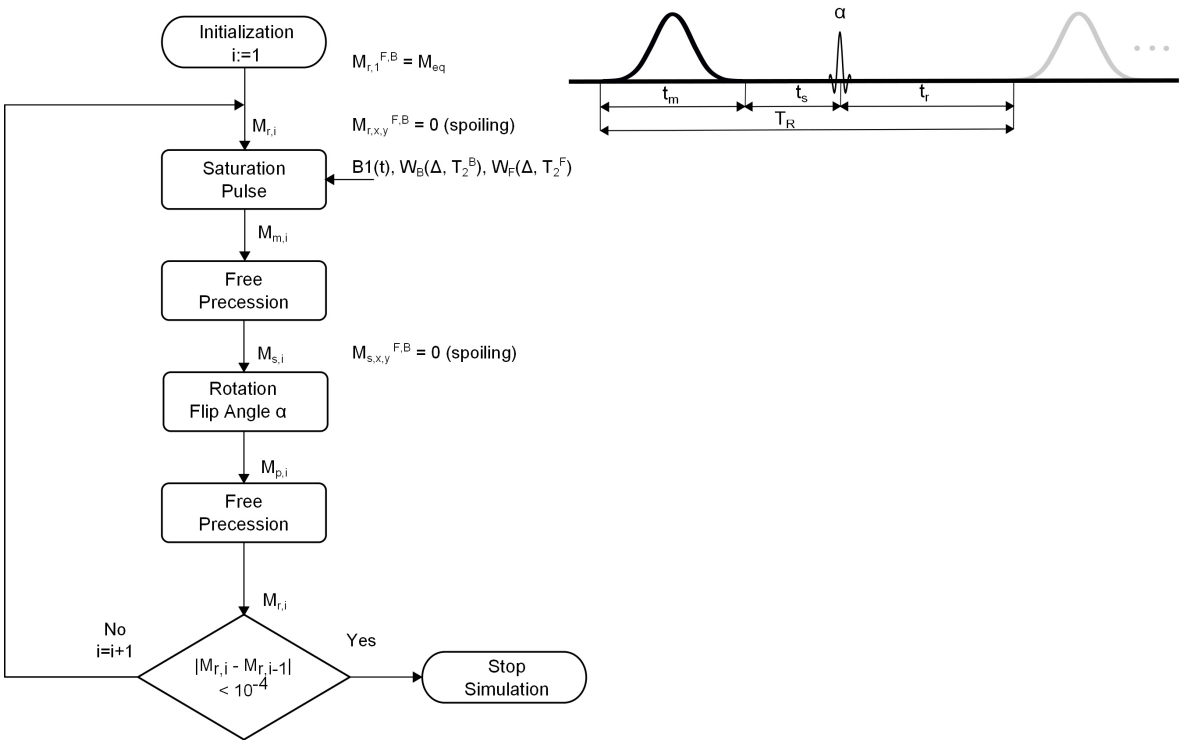

Figure 3.1: Flow chart of the numerical implementation of the coupled Bloch equations for one off-resonance saturation frequency. The pulse sequence of the pulsed MT-model is split up into four different time intervals, where for each time interval the coupled Bloch equations are solved numerically. The longitudinal magnetization of the free pool before the off-resonance saturation pulse is denoted with $M_{r,i}^F$, and immediately after the pulse with $M_{m,i}^F$. The magnetization before and after flip angle α is $M_{s,i}^F$ and $M_{p,i}^F$. Then, the input for the next iteration is the magnetization $M_{r,i}^F$ at the end of the sequence repetition time. The simulation stops when the deviation from the last iteration is less than 10^{-4}, otherwise the counter i is increased by 1 and the simulation is continued.

sequence, were carried out with the coupled Bloch equations and their approximation by Eqn. (2.38).

In Table 3.1 the results fro the four-parameter fit of Yarnykh [14] for WM are listed. With these parameters, and the sequence parameters of Yarnykh [14] in Table 3.2, several simulations has been performed.

Steady state solution: The derived steady-state solution M_{ss} in Eqn. (2.30) was compared with the numerical simulations of the coupled Bloch equations over a wide range of off-resonance saturation frequencies. For estimating the numerical solution of the steady-sate magnetization a CW experiment, with a 5s rectangular RF-pulse and an amplitude of $\omega_{1rms} = 634.6 rad/s$, was simulated. The parameters for the two-pool were set as listed in Table 3.1.

Pulsed Steady State: The evolution of the longitudinal magnetization over time was simulated for different off-resonance saturation frequencies until the pulsed-steady was reached.

Z-spectra: To show the influence of the parameters from the two-pool model, Z-spectra were estimated by varying each parameter in Table 3.1 in a physical reasonable range – whilst keeping the other parameters of Table 3.1 constant. To compare the results with the coupled Bloch equations the average deviation, denoted as σ_{1kHz}, of the approximated model and the coupled Bloch equation were calculated for values above an off-resonance saturation frequency of 1kHz.

Table 3.1: Two-pool parameter set for WM that was derived by Yarnykh [14] from a four-parameter fit of the Z-spectrum assuming that $R_1^F = R_1^F$.

R_1^F	R_1^B	T_2^F	T_2^B	k	f
$1.17s^{-1}$	$1.17s^{-1}$	21ms	$9.7\mu s$	$3.5s^{-1}$	14.8%

Table 3.2: Sequence parameter for the simulations.

ω_{1rms}	t_m	t_s	t_r	α
$634.6rad/s$	20ms	3ms	25.2ms	10°

3.1.2 Parameter Estimation of the Pulsed MT-Model

The problem for estimating the four parameters ($\mathbf{p} = [f, k, T_2^F, T_2^B]$) of the two-pool model can be considered as a non-linear least squares problem where the difference between the expected, or measured value $m_{z,exp}$, and the estimated value of the model $m_{z,model}(\mathbf{p})$ is minimized in the L_2-norm:

$$\min_{\Delta} \|m_{z,exp}(\Delta) - m_{z,model}(\Delta, \mathbf{p})\|_2 = \min_{\Delta} \sum_{i=1}^{N} \left(m_{z,exp}(\Delta_i) - m_{z,model}(\Delta_i, \mathbf{p})\right)^2 \quad (3.1)$$

where Δ_i are the different off-resonance saturation frequencies with a total number N. The minimization problem was solved with the lsqnonlin function of MATLAB which has two different algorithm implemented for estimating the parameters. The default algorithm of the lsqnonlin function is the Trust-region-reflective, and the second one is the Levenberg-Marquardt algorithm.

Quality of Fit

To asses the quality of the estimated parameters different methods were used. First, the residuals r_i for each measured off-resonance saturation frequency were calculated defined as the difference of estimated magnetization $m_z(\mathbf{p}, \Delta_i)$ $m_{z,exp}$ and the measured magnetization $m_{z,exp}(\Delta_i)$:

$$r_i = m_z(\mathbf{p}, \Delta_i) - m_{z,exp}(\Delta_i) \qquad i = 1, 2, ..., N \tag{3.2}$$

then the residual norm is defined as followed:

$$r_{norm} = \sqrt{\sum_{i=1}^{N} r_i^2} \tag{3.3}$$

The function lsqnonlin provides also the Jacobi matrix $\mathbf{J}$ as an additional output parameter from the last iteration of the solver. Assuming that the errors of the measured data points $m_{z,exp}$ are statistically uncorrelated, it is possible to approximate the covariance matrix of the parameters with the Jacobi matrix $\mathbf{J}$:

$$\mathtt{Cov}(\mathbf{p}) \approx \sigma^2(\mathbf{J}(\mathbf{p})^T\mathbf{J}(\mathbf{p}))^{-1} \tag{3.4}$$

where σ^2 is the variance of the noise of the measured data.

Further, with the covariance matrix an approximation of the confidence intervals can be made. The approximated confidence intervals are estimated as follows:

$$\mathbf{p}_\alpha = \mathbf{p} \pm t_{1-\frac{\alpha}{2}}(\nu)\sqrt{\mathtt{diag}(\mathtt{Cov}(\mathbf{p}))} \tag{3.5}$$

where $t_{1-\frac{\alpha}{2}}(\nu)$ is the student's t-distribution with a significance α and ν degrees of freedom.

3.2 Error Model of Yarnykh Compared with Numerical Error Simulations

For the error estimation of the single-point approach Yarnykh proposed an error model [14], which is also briefly described in Section 2.4.3. This model has been implemented in this work to estimate the mean absolute percentage error of the approach, and additionally numerical error simulation were carried out to validate the error-model of Yarnykh [14].

Numerical Errror Simulations

For the numerical error simulations the same formalism is used as in the error model of Yarnkyh [14], but instead of a first order approximation of the errors, the error due noise $\sigma_{i,j,k}$, and the bias $\beta_{i,j,k}$, are estimated numerical. In Figure 3.2 a sketch is shown that illustrates the numerical error-model for the single-point approach with the bias in the upper path and the error due noise in the lower path.

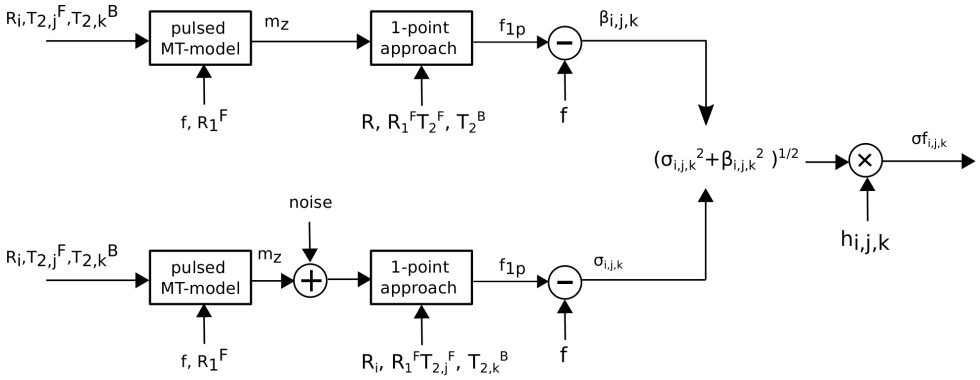

Figure 3.2: Numerical error simulations of the single-point approach with a synthetic data set. The upper path estimates the bias $\beta_{i,j,k}$, due constraining the parameters (R, $R_1^F T_2^F$ and T_2^B) from their actual value ($R_i, T_{2,j}^F and T_{2,k}^B$) for a specific f and R_1^F. The bias is estimated as the deviation from the true bound pool fraction f, and the estimated bound pool fraction f_{1p}. The error due noise $\sigma_{i,j,k}$ is estimated similar, except that noise is added after the estimation of the Z-spectrum, and that the constraints of the single-point approach are the input parameters of the pulsed MT-model. The final error is the root mean square error weighted with $h_{i,j,k}$.

To estimate the bias and the errors due noise of the single-point approach predefined parameter sets of the two-pool model are used as a reference. This simple approach has the advantage that the true values of the parameters are known.
In the first step for the current parameter set, $R_i, T_{2,j}^F$ and $T_{2,k}^B$, the Z-spectrum is calculate

with Eqn.(2.40) of the pulsed MT-model. Then with single-point approach the bound pool fraction f_{1p} is estimated by fitting the value of the magnetization m_z at a certain off-resonance saturation frequency and amplitude. After that, the bias is calculated as the deviation from the true value of the bound pool fraction f from the estimated one f_{1p}. For estimating the error due noise the numerical approach is similar, except that the constraints of the single-point model are the input parameters resulting in zero bias and that noise with a standard deviation $\sigma_{noise}(m_z)$ is added before estimating f_{1p}:

$$\sigma_{noise}(m_z) = \frac{\sqrt{1+m_z^2}}{SNR_{ref}} \tag{3.6}$$

assuming that the covariance of the noise in the reference image and the off-resonance images is zero.

After adding noise the bound pool fraction is estimated with the single-point approach, and then, the difference between the constrained value is calculated to estimate the error due noise.

To calculate deviation $\sigma_{f,i,j,k}$ of f for the given parameter set the resulting term of the root mean squared value of the bias and error due noise is multiplied with weighting factor a $h_{i,j,k}$. For the numerical simulations $h_{i,j,k}$ was derived from the multivariate normal probability density function of the parameter combinations. The multivariate normal probability density was estimated with the mvnpdf() function and then the result was normalized with its sum to achieve that the sum of all coefficient is 1. The input parameters of the function were the mean and standard deviation of the parameters. Furthermore it was assumed that the covariances of the parameters are zero.

Finally, the mean absolute deviation σ_f for the complete parameter set was estimated by summing up the individual error $h_{i,j,k}\sigma_h$.

Simulations

In the simulations the error model of Yarnykh [14] was compared with the numerical error simulations to evaluate the strength and weaknesses of each method. For that purpose a synthetic data set was generated with a total number of 500 parameter combinations. This synthetic data set consisted of different parameter combinations of the two-pool model, which serve as reference value for the error estimation. Similar to simulations of Yarnykh [14] the relative error of the single-point approach was simulated with an average brain. For the simulations it was assumed that the three parameters R, T_2^B, T_2^F of the two-pool model are normally distributed, and that the parameters are independent from each other. Note that the reverse rate R is constrained by $R = k(1-f)/f$, and

that f is fixed approximately on the average brain value, $f = 9\%$, which was found by Yarnykh [14]. Furthermore it is assumed that the observed longitudinal relaxation rate $R_1 = 0.9s^{-1}$ is constant for all data points. The constraints for the single-point approach were set to the values that were estimated by Yarnykh [14] for an average brain.
Table 3.3 summarizes the mean and the standard deviation of the parameters that were used to generate the synthetic data. Note that the standard deviations were approximated from the parameter histograms since their were no explicit value stated in [14].

Table 3.3: Mean and standard deviation of the parameters that were used to generated the synthetic data set to compare the error model of Yarnykh [14] and the numerical error simulations.

R	T_2^B	T_2^F
$19s^{-1} \pm 8s^{-1}$	$9.7\mu s \pm 2\mu s$	$244ms \pm 5ms$

For the error model of Yarnykh [14] two functions were implemented in MATLAB, which estimate the error term $\sigma_{i,j,k}$ due noise and the bias $\beta_{i,j,k}$ for a set of parameters $(R_i, T_{2,j}^F, T_{2,k}^B)$. The derivations in the error model were solved numerically with finite differences. To compare the results of the error-model with the numerical simulations the mean absolute percentage error δ_f was calculated by dividing the standard deviation of the estimated bound pool fraction by the average brain value (9%):

$$\delta_f = \frac{\sigma_f}{f} 100\% \tag{3.7}$$

To illustrate the influence of noise, several simulations with different SNR_{ref} were performed with the generated parameter set. Furthermore simulations with different effective flip angles were carried out.

3.3 BSA Phantom Measurements

In order to validate the pulsed MT-model by Yarnykh and Yuan[13], and furthermore the single-point approach by Yarnykh [14], measurements with cross-linked bovine serum albumin (BSA) were carried out. Therefore images were acquired with a 3T MRI scanner (MAGNETOM Prisma fit, Siemens Healthcare, Siemens, Erlangen, Germany) with a water phantom that contained 28 cuvettes with four different BSA concentrations ([BSA] = 14, 18, 22, and 26%), where each sample was doped with seven different ferritin (from equine spleen) concentrations ([Fe] = 0, 25, 50, 75, 100, 150, 175 and 200mg/kg). The different BSA concentrations were used to simulate the bound pool of the two-pool model. The purpose of the different ferritin concentrations for the same BSA concentration was to change the observed relaxation time $T_{1,obs}$ while keeping the bound pool fraction the same. A schematic sketch of the cross-section of the BSA-phantom is illustrated in Figure 3.3.

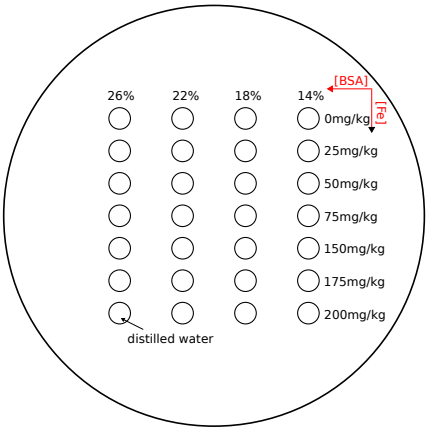

Figure 3.3: Schematic sketch of the cross-section of the BSA phantom. From right to left the BSA concentration increases and from top to bottom the iron concentration increases. The bottom-left cuvette is a sample which contains distilled water as a reference value a bound pool fraction of zero.

3.3.1 MRI Protocol and Image Preprocessing

MT-weighted images

MT-weighted images were acquired with FLASH sequence and a gaussian saturation pulse at fifteen resonance offsets (Δ =0.6, 1, 2, 3, 4, 5, 6, 7, 8, 9, 10, 12, 16, 20 and 96 kHz) with three different effective saturation saturation flip angles ($FA_{MT} = 600°, 800°$, and $1000°$). Every image was acquired four times so that the SNR could be increases by averaging. In Figure 3.4 a screenshot of the sequence for one repetition rate is shown and in Table

3.4 the detailed sequence parameters are summarized.

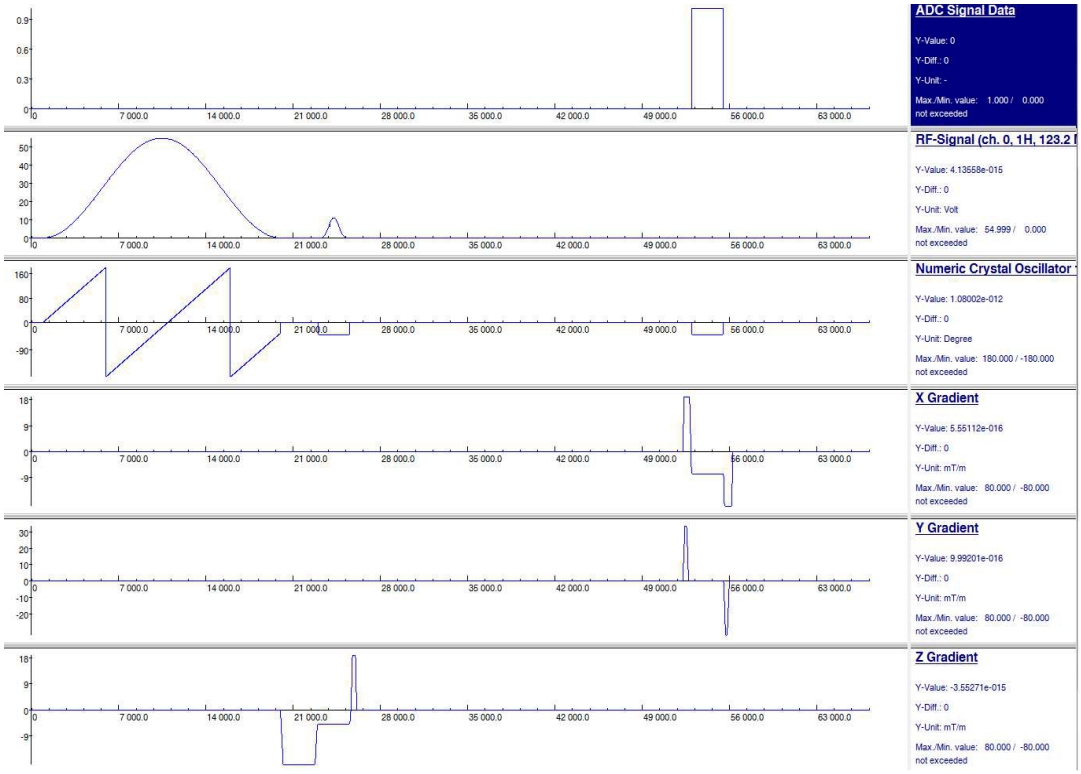

Figure 3.4: Screenshot of the FLASH sequence with MT saturation pulse for one repetition rate. A brief description of the sequence can be found in Section 2.3.2.

The acquired MT-weighted were normalized with the image acquired at 96kHz off-resonance saturation frequency, assuming that the pulse has no saturation effect, and therefore that the MT-pulse has no influence on the measured signal.

Table 3.4: Sequence parameter of the FLASH sequence with gaussian saturation pulse for the BSA phantom measurements.

FA_{MT}	t_m	t_s	t_r	α
600°/800°/1000°	19ms	4 ms	27ms	18°

For the three image series with different effective saturation flip-angles the same processing steps were carried out. First, the normalized magnetization $m_z(\Delta)$ was calculated by dividing the off-resonance images with the reference image that was acquired at 96 kHz. After the normalization voxel values that were greater than 1 were set to 1, and values that were not defined were set to 0.

T_1-map

For the reconstruction of the T_1-map a spin echo inversion recovery sequence was used. In this experiments six inversion images (TI = 100, 200, 400, 800, 1600 and 3200ms) were acquired with a repetition rate TR of 12s. The T_1 times were estimated by fitting a single exponential relaxation function for each voxel of the images with the LM-Fletcher algorithm.

B_1-map

For the estimation of the active field B_{1+}-map the Double Angle Method (DAM) [43] with EPI readout was used. The two double angle images ($\alpha_1 = 40°, \alpha_2 = 80°$) for the B_{1+}-map were acquired with the same FLASH sequence that was used for the MT-weighted images, but without MT-saturation pulse and with a T_R of 12s. After the calculation of $\alpha_1(\mathbf{x})$ the resulting image was normalized with 40° and filtered with a gaussian filter with a kernel size of 41 pixels and a standard deviation of 21.

B_0-map

For the estimation of the B_0 field map the phase difference method was used. Therefore two GRE images ($\alpha = 30°, TR = 50ms$) with $T_{E,1} = 4.1ms$ and $T_{E,2} = 6.1ms$ were acquired to calculate the B_0-map from the phase shifts between both echos.

3.3.2 Estimation of the Reference Bound Pool Fractions

The purpose of the phantom measurements was to examine four major points that have influence on the results of the fast bound pool fraction estimation from a single off-resonance measurement: the selected off-resonance saturation frequency with different amplitudes, the noise and the bias due to constraining the parameters. Therefore a reference value was estimated with a four parameter fit of the pulsed MT-model [13] that was as accurate as possible the true value of the bound pool fraction for each BSA concentration.
For each saturation pulse amplitude all four image series of each off-resonance frequencies were averaged, and then further, the voxels in each ROI were averaged to get the best signal to noise ratio for each ROI. Finally, the signal values for each BSA concentration and off-resonance saturation frequency were normalized with the averaged value at the off-resonance saturation frequency of 96kHz. Then final results of the averaging were

three Z-spectra for each BSA concentration with the three different effective saturation flip angles FA_{MT}.
With the Z-spectra the two-pool parameters of the BSA concentrations were estimated with two different fitting approaches. In the first approach the Z-spectra for the three saturation pulse amplitudes were fitted separate for each BSA concentration resulting in three parameter sets. Whereas in the second approach a global fit was performed by minimizing the cost-function of the three spectra for one BSA concentration resulting in one parameter set.
Before fitting the Z-spectra the flip angle of excitation RF pulse α and the effective saturation flip angle were corrected by multiplying it with the normalized B_{1+}-map. Furthermore the off-resonance saturation frequency of the saturation pulse was corrected by calculating the frequency shift Δf with the B_0-map ($\Delta f = \frac{\gamma \Delta B_0}{2\pi}$).
To compare the results of the fits, and to choose the most reasonable fit, the confidence intervals for $\alpha = 0.05$, defined in Eqn. (3.5), were calculated. Then linear regressions with the estimated bound pool fractions as function of the BSA concentrations were carried out to asses the quality of the different fits.
For the evaluation it was assumed that in each curvette the BSA concentration is homogeneous, and that signal deviation within the cuvette are only due to field bias.

3.3.3 Evaluation of the Single-Point Approach

For the estimation of the bound pool fraction from a single off-resonance measurement [14] the three constraints of the the remaining parameters (R, $T_2^F R_1^F$, T_2^B) had to be defined of the pulsed MT-moded. These constraints were estimated by calculating the weighted mean of the previous estimated reference values. The number of voxels within a ROI were chosen as weights to account for the different number of voxels within the ROIs. In order to get different SNR, the four acquired image series, for each off-resonance saturation frequency and saturation pulse amplitude, were averaged from one to four resulting in four image series with different SNR. Then with each image the bound pool fraction was estimated in the first four BSA ROIs (without iron) with the single-point approach. Like for the estimation of the reference values, the flip angle and the effective flip angle were corrected with the normalized B_{1+}-map and the off-resonance saturation frequency was corrected with the B_0-map.
To compare the estimated bound pool fraction f_{1p,vx,ROI_x} from a single off-resonance measurement the mean absolute error $\delta_{f_{ROI_x}}$ was estimated with the previous estimated

reference value f_{ref,ROI_x} for each ROI:

$$\delta_{f_{vx,ROI_x}} = \frac{1}{N_{vx}} \sum_{vx=1}^{N_{vx}} |\frac{f_{1p,vx,ROI_x} - f_{ref,ROI_x}}{f_{ref,ROI_x}}| \tag{3.8}$$

where the vx stands for voxel with a total number N_{vx}, and x in ROI_x denotes ROI 1 to 4. Then, the mean absolute percentage error was calculated for the total number N_{ROI} of the ROIs:

$$\delta_f = 100\% \frac{1}{N_{ROI}} \sum_{x=1}^{N_{ROI}} \delta_{f_{vx,ROI_x}} \tag{3.9}$$

Furthermore, the estimated mean absolute percentage errors were compared with the predicted error from numerical error simulations.
A synthetic image was generated where each voxel within the ROIs has the same two-pool parameters and R_1^F as the estimated reference values of the four parameter. With this data set numerical error simulations of the single-point approach were carried out with the same sequence parameters described in Section 3.3.1. The numerical error simulations are similar to the once carried out in Section 3.2 with the only difference that R_1^F and f were input parameters for each voxel. Therefore the Z-spectrum was calculated with five parameters (f, k, T_2^F, T_2^B and R_1^F) rather than with average values for f and R_1^F. The weighting $h_{i,j,k}$ was set to 1 since the complete parameter distribution was simulated.

3.3.4 Influence of $T_{1,obs}$

To evaluate the influence a varying observed relaxation time $T_{1,obs}$ on the pulsed MT-model, while the bound pool fraction is constant, the remaining BSA samples with iron were analysed. Therefore the first six rows, which had the same iron concentration, were examined separate with the same methods described before in section 3.3.2, expect that only a global fit was performed. Plots were created with the estimated bound pool fraction as a function of the BSA concentration for each iron concentration to asses the influences of different $T_{1,obs}$.

3.4 Post Mortem Measurements

With a slice of a fresh post mortem brain, embedded in Galden (proton free solution), the four-parameters of the two-pool model and the bound fraction from a single off-resonance measurement were carried.

For estimating the four two-pool parameter MT-weighted images with three different effective saturation flip angles ($FA_{MT} = 600°, 800°$, and $1000°$) at fifteen off-resonance saturation frequency (Δ =0.6, 1, 1.5, 2, 2.5,3, 4, 5, 6, 7, 8, 10, 12, 16, 32 and 96 kHz) and 6 signal averages were acquired, resulting in 45 data points for each voxel. The images were normalized with the image acquired at 96 kHz off-resonance saturation frequency.

The B_1-, B_0-, and T_1-map were estimated with the same methods as for the BSA-phantom measurements described in Section 3.3.1. All images were acquired with a resolution of $1x1x1mm^3$.

Then, with the Z-spectra a global fit was performed for each voxel where the flip angle and effective saturation flip angle were corrected with normalized B_{1+}-map and the off-resonance saturation frequency was corrected with the B_0-map. To asses the quality of the estimated parameters the confidence intervals estimated were estimated with Eqn. (3.5) ($\alpha = 0.05$). The standard deviation of the noise was approximated by the mean value of Eqn.(2.46) for the measured data points.

The estimated parameters for WM, GM and the whole brain (WM + GM) were analysed. Therefore a WM and GM mask was generated by windowing the T_1-map: $WM_{T1} = [0.8, 1.1]s^{-1}$ and $GM_{T1} =]1.1, 8]s^{-1}$.

3.5 In Vivo Measurements

In the last step of the thesis the fast bound pool fraction estimation from a single measurements [14] was performed with in vivo measurements. Similar to the BSA-phantom and post mortem measurements the method was compared with the four-point fit results of the pulsed MT-model. Therefore a separated MRI-protocol was designed which allows to estimate the four two-pool model parameters within tolerable in vivo scan times.
Then the MRI-protocol was changed to a high resolution MRI-protocol, which allows to calculate high resolution f-maps with the single-point approach.

3.5.1 Parameter Estimation Pulsed MT-Model

In order to find the best constraints for the fast bound pool fraction estimation, the two-pool model parameters were estimated by fitting the pulsed MT model to seven off-resonance saturation frequencies (Δ =0.6, 1, 2, 4, 8, 12, and 96 kHz) and two amplitudes ($FA_{MT} = 600°, 1000°$) with an excitation flip angle $\alpha = 18°$ and a repetition rate $T_R = 50ms$. All images were normalized with the image acquired at 96 kHz off-resonance saturation frequency.
Analogous to the BSA phantom and the post-mortem measurements the Double Angle Method [43] and the phase difference method was used for the estimation of the B_{1+}-map and B_0-map, respectively. To decrease the scan time for the Double Angle Method the B_{1+}-map was estimated with a 2D EPI read out with flip angles $\alpha(\mathbf{x}) = 60/120°$ and a repetition rate of $T_R = 12s$. For the B_0-map the echo times of the 3D GRE were set to $T_{E,1} = 4.1ms$ and $T_{E,2} = 5.1ms$. For the T_1-mapping a MP2RAGE [39], wich is illustrated in Figure was selected.
All images were acquired with the same in-plane resolution of 1.5x1.5mm^2 and a slice thickness of 5mm.
The scan time was about 2min 25s for each MT-weighted image, 2min 30s for images of the B_0 calculation, 2min 20s for images for the B_{1+}-map, and 4min 30s for the MP2RAGE image, resulting in total scan time for the entire protocol of 45min.
Before starting the image processing the MT-weighted images and the T_1-map were registered with the eddy current correction implemented in FSL [1] [48]. The brain, WM and GM were extracted from the T_1-map using SIENAX[2] [49, 50] with the following parameters: sienax T1map.nii.gz -d -B "-f 0.35 -R -S -B" -r -d.
With the normalized Z-spectra images the four two-pool model were estimated by a voxel

[1] http://fsl.fmrib.ox.ac.uk/fsl/fslwiki/FDT/UserGuide
[2] http://fsl.fmrib.ox.ac.uk/fsl/fslwiki/SIENA

based fit of the pulsed MT-model. The quality of the parameters for each voxel was evaluated by calculating the confidence intervals with Eqn. (3.5) with $\alpha = 0.05$. For each voxel the standard deviation of the noise was approximated by measuring the SNR of the reference image SNR_{ref} and taking the mean of the standard deviations estimated with Eqn. (2.46) for all the data points of the voxel.
With the estimated maps parameter histograms were generated and the median of the parameter histograms was used to define the constraints of the single-point approach. Furthermore with the numerical error-model, described in Section 3.2, simulations were carried out to find the best sampling point for estimation the bound pool fraction from a single off-resonance measurement.

3.5.2 Single-Point Approach

With the results from the four parameter fit the constraints were estimated for the estimation of high resolution f-maps with the single-point approach. Therefore MT-weighted images with a resolution of $1x1x2.5mm^3$ were acquired with three different off-resonance frequencies (Δ =4, 6, 96 kHz) at one saturation pulse amplitude ($FA_{MT} = 600°$). The two images at 4kHz and 6kHz were normalized with the one acquired at 96kHz off-resonance saturation frequency. The T1-map was acquired with MP2RAGE, which was acquired at the same resolution as the MT-weighted images and, the field correction images were acquired with a lower resolution of $2x2x5mm^3$.
After interpolation of the B_0-map and B_{1+}-map to the size of the MT-weighted images the f-maps were calculated with the single-point approach as described in Section 3.3.3.

4 Results

4.1 General Implementations and Simulations

4.1.1 Coupled Bloch Equations and the Pulsed MT-Model

Steady State Solution

In Figure 4.1 the simulation results with the two-pool parameters of Table 3.1 for the steady state solution M_{ss} for different off-resonance saturation frequencies Δ is shown. The solid line represents the solution of the numerical simulation of the coupled Bloch equations (2.13), and the dashed line the analytic solution of Eqn. (2.30). It can be seen that the numerical and the analytical solution are identical.

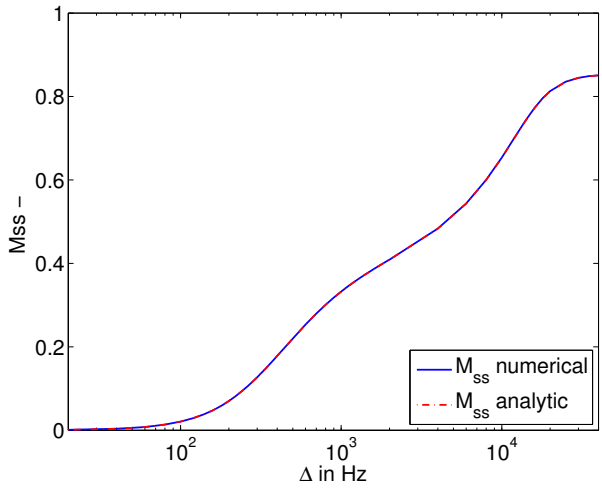

Figure 4.1: Comparision of the numerical simulation of the steady state solution M_{ss} (solid line) with the analytic solution (dashed line). Numerical solution were estimated with a 5s rectangular CW with an amplitude of $\omega_{1rms} = 634.6 rad/s$. The parameters of the two-pool model are listed in Table 3.1.

Pulsed Steady State

Simulations of the evolving magnetization for the free pool M^F are shown in Figure 4.2 with an off-resonance saturation frequency of 100 Hz (a) and 4kHz (b). The solid lines represent the numerical solution of the coupled Bloch equations, and the dashed lines are the approximation of the pulse sequence with Eqn. (2.25), (2.32) and (2.33).
The simulation results show that with lower off-resonance saturation frequency the magnetization of the free-pool is faster in the pulsed steady state and that the amplitude goes nearly to zero. The agreement between the coupled Bloch equations and their approximation is excellent for the simulation for 4kHz, whereas for 100Hz the results differ, especially during the off-resonance saturation pulses.

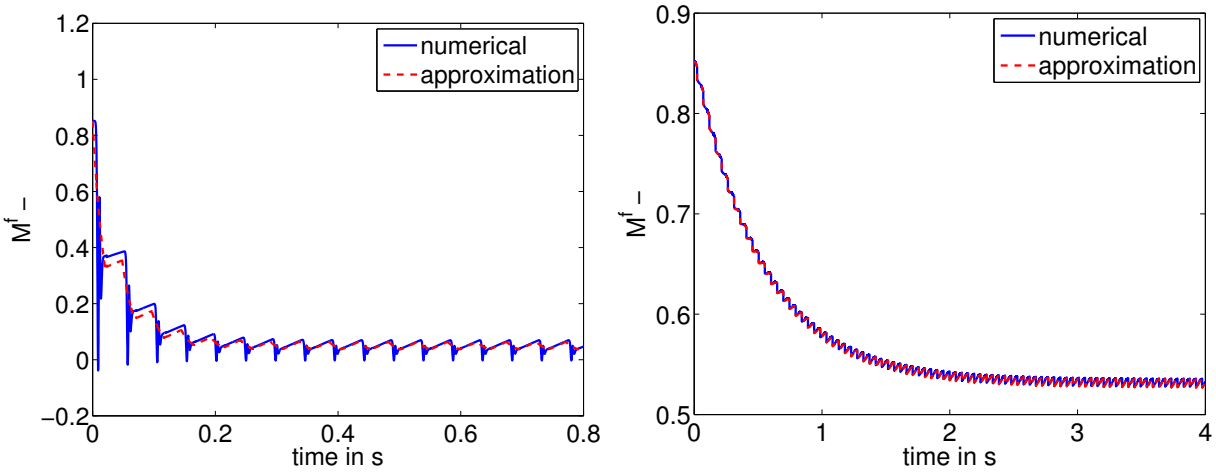

(a) $\Delta = 100Hz$ (b) $\Delta = 4kHz$

Figure 4.2: Evolving of the magnetization M^f of the free pool with two different off-resonance saturation frequencies Δ until pulsed steady state is reached. The solid lines in (a) and (b) are the results of the numerical simulation of the coupled Bloch equations, and the dashed lines the approximated solutions for the different time intervals.

Z-Spectra with different Parameters

In Figure 4.3 simulated Z-spectra with the coupled Bloch equations (2.13) and the signal equation (2.40) are shown. In each plot three simulations were carried out where one parameter was changed, and the others were fixed as listed in Table 3.1.

The results in Figure 4.3 show that mean average deviation σ_{1kHz} is for all simulations smaller than 0.4%. The lowest deviation has the simulations for $R_1^F = 5s^{-1}$ with a deviation of 0.12%.

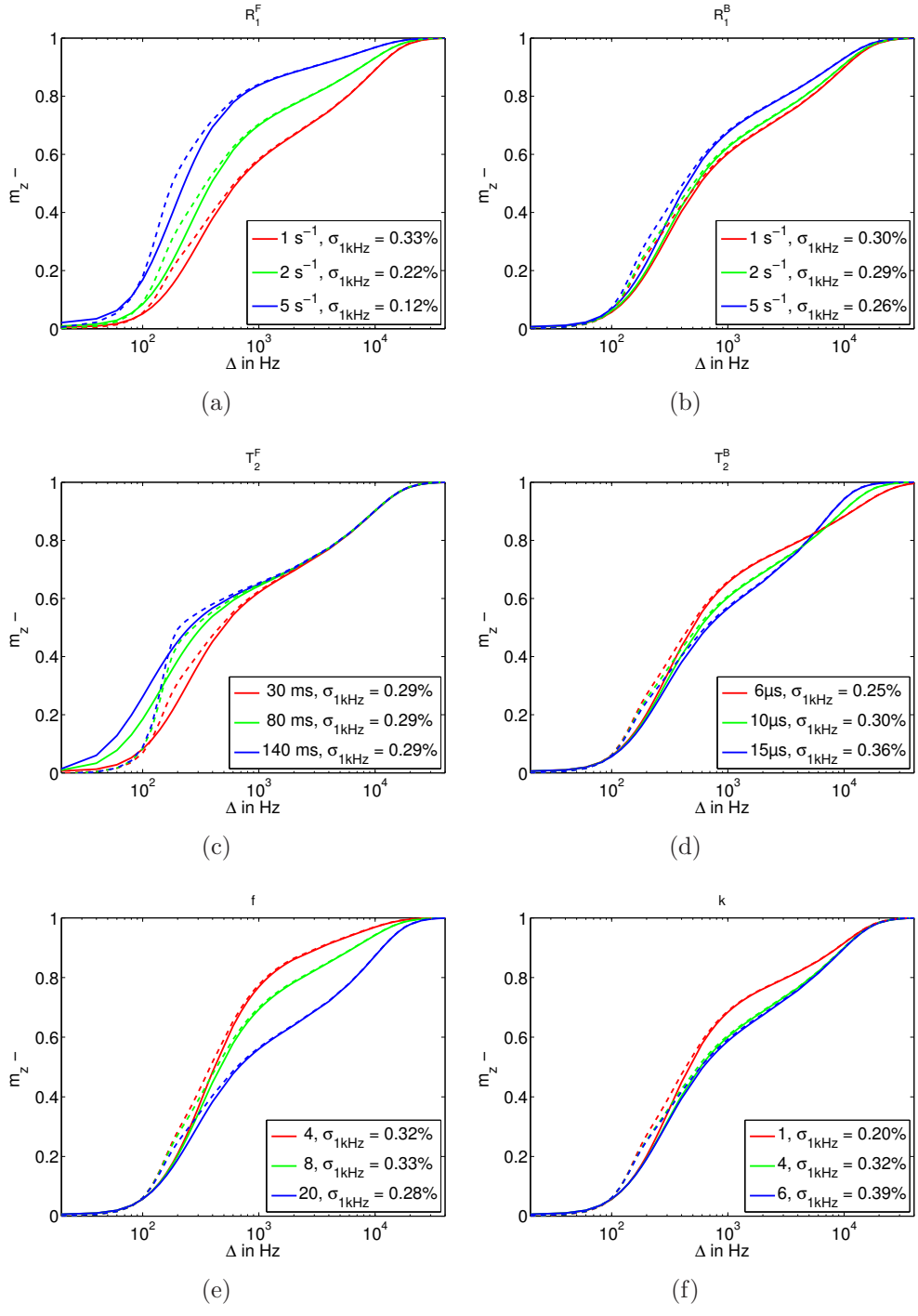

Figure 4.3: Numerical simulations of Z-spectra with the coupled Bloch equations (2.13) *(solid lines) and its approximation (dashed line) by Eqn.* (2.38)*. In each plot one parameter of the two-pool model is changed three times, and the other five parameters were kept constant. The constant parameters and sequence parameters are listed in Table 3.1 and Table 3.2, respectively.*

4.2 Error Model of Yarnykh Compared with Numerical Error Estimation

In Figure 4.4 (a)-(c) the parameter histograms of the synthetic data set are illustrated with the resulting Z-spectra in Figure 4.4 (d).

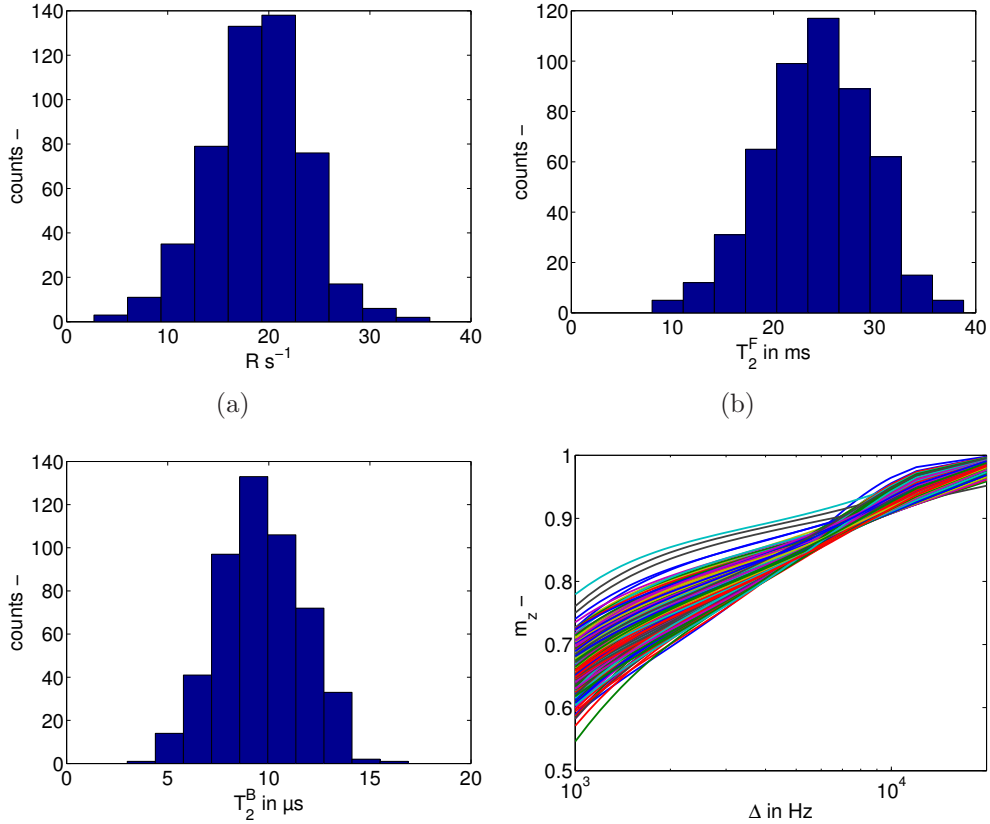

Figure 4.4: Parameter histograms (a)-(c) of the synthetic data set that was used for the comparison of the numerical error estimation and the error model of Yarnykh [14] with the resulting Z-spectra in (d). Parameters are normal distributed with mean and standard deviation as listed in Table 3.3.

In Figure 4.5 (a) the bias of the single-point approach due constraining the parameters R, T_2^F, and T_2^B is shown. The influence of the noise for different signal to noise ratios of the reference image SNR_{ref}, without the bias ($\beta_{i,j,k} = 0$), is presented in Figure 4.5 (b). In Figure 4.5 (a) and Figure 4.5 (b) can be seen that the numerical simulation (dashed lines) differ from the results of the error model (solid lines). For both cases the error model overestimates the error compared to the numerical simulations.

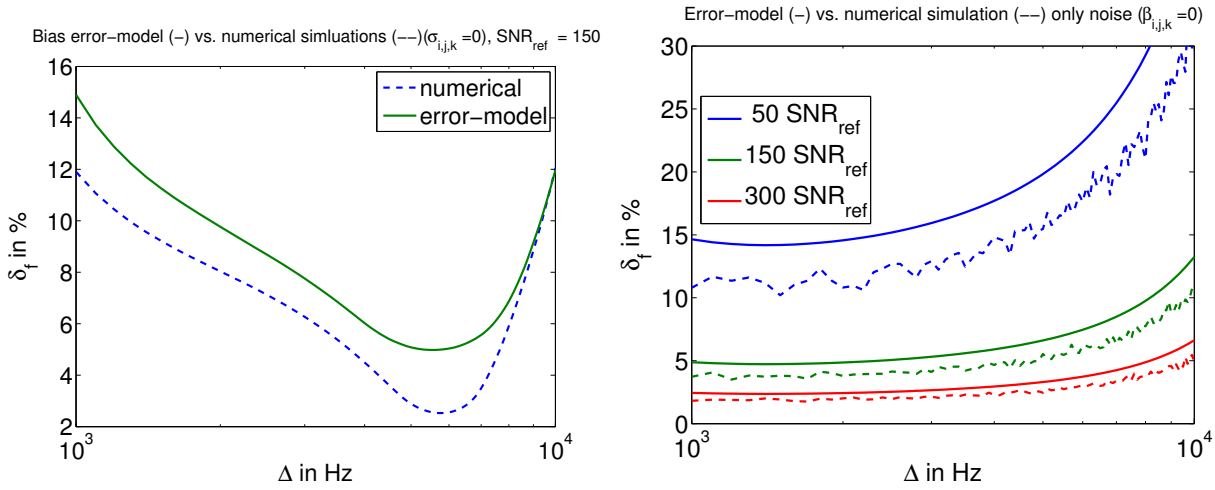

(a) (b)

Figure 4.5: Comparison of the numerical error simulation and the error model with the synthetic data set for different off-resonance saturation frequencies Δ with $SNR_{ref} = 150$. In (a) and (b) the influence of the bias and the influence of the noise, respectively, is shown on the total relative error δ_f. The dashed line represents the numerical estimated error and solid lines the results with the error model.

To illustrate the influence of the bias and the error due to noise on the mean absolute percentage error δ_f both errors were potted in Figure 4.6. It can be seen that the bias (dotted line) has a minimum at around 5kHz, whereas the error due to noise (dash-dot line) is monotonically increasing with higher off-resonance saturation frequency. The resulting mean absolute percentage error (dashed line) has a minimum at 4kHz.
The influence of different SNR_{ref} on the mean absolute percentage error is illustrated in Figure 4.6 (b), estimated with the numerical simulations (dashed line) and the error model (solid line). The simulations show that the numerical error simulations (dashed line) and the error-model (solid line) differ and that with increasing SNR_{ref} the error decreases.

In Figure 4.7 (a) the influence of effective saturation flip angle FA_{MT} on the bias was simulated with the error model (solid lines) and the numerical error simulations (dashed lines) is presented. The minimum of the mean absolute percentage error increases with the effective flip and is shifted towards the right sight of the spectrum. Again, the results of numerical error simulations show smaller errors compared to the error model.
The influence of FA_{MT} on the error due to noise is illustrated in Figure 4.7 (b). The results of the numerical simulations (solid lines) as well as the error model (dashed) indicate that the error approaches a limit with increasing FA_{MT}.

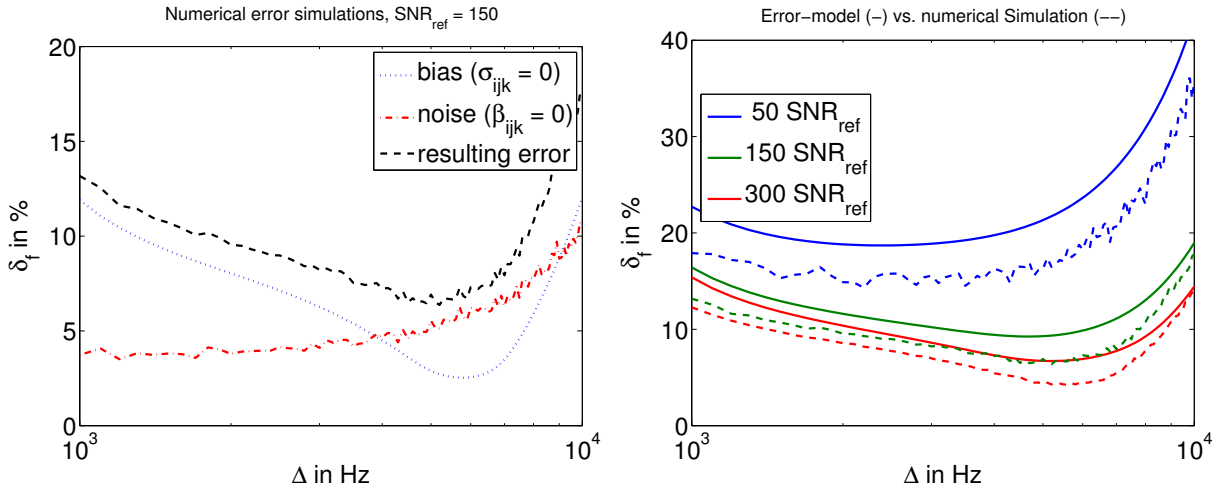

(a) (b)

Figure 4.6: Total relative error simulations with the synthetic data set. In (a) the total relative error (solid line) was estimated numerically for $SNR_{ref} = 150$ and $FA_{MT} = 600°$. Furthermore the bias (dash-dot line), and the error due to noise (dotted line), are plotted separately. The total relative error of the numerical error simulation (dashed lines) and the error model (solid lines) were plotted in (d) for different SNR_{ref}

The mean absolute percentage error of the bias term and the noise term combined is plotted in Figure 4.8. It shows that the mean absolute percentage error gets smaller with increasing effective saturation flip angle. Furthermore both approaches indicate that the error converges a fix limit for effective saturation flip angles great than 1000°.

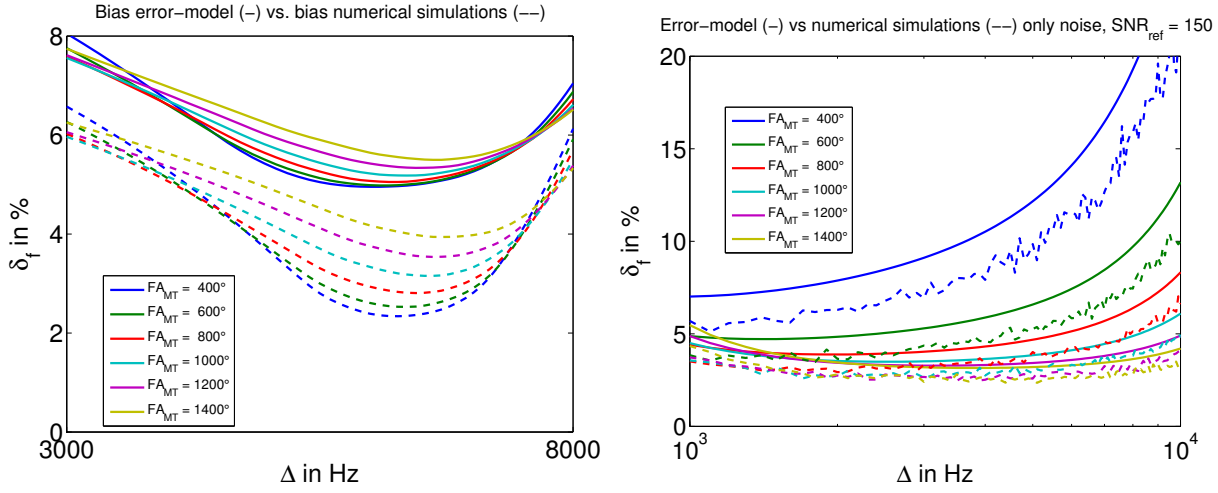

(a) (b)

Figure 4.7: Comparison of the bias estimated with the error model (solid lines) and the numerical error estimations (dashed lines) for different effective saturation flip angles FA_{MT}. In (b) a detailed view of the minimum is shown.

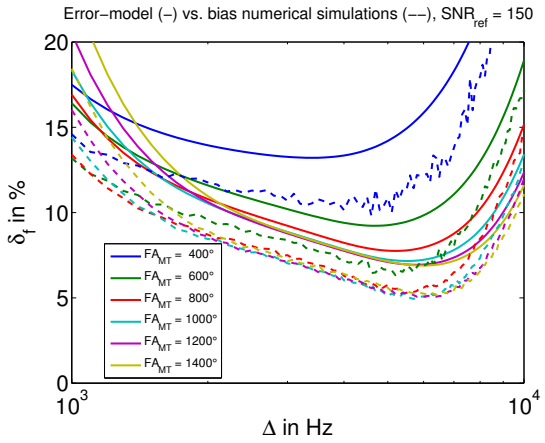

(a)

Figure 4.8: Mean absolute percentage error of the synthetic data estimated with the error model (solid lines) and numerical simulations (dashed lines) for different effective saturation flip angles FA_{MT}.

For the validation of the error model of Yarnykh [14] first-order approximation were calculated for the means of the synthetic data set. In Figure 4.9 the results for an off-resonance frequency of 4kHz are illustrated. One can see that the approximation for f, T_2^F and T_2^B are close to the true value over a wide range of the specific parameter, whereas the approximation for R is only valid for small changes of R.

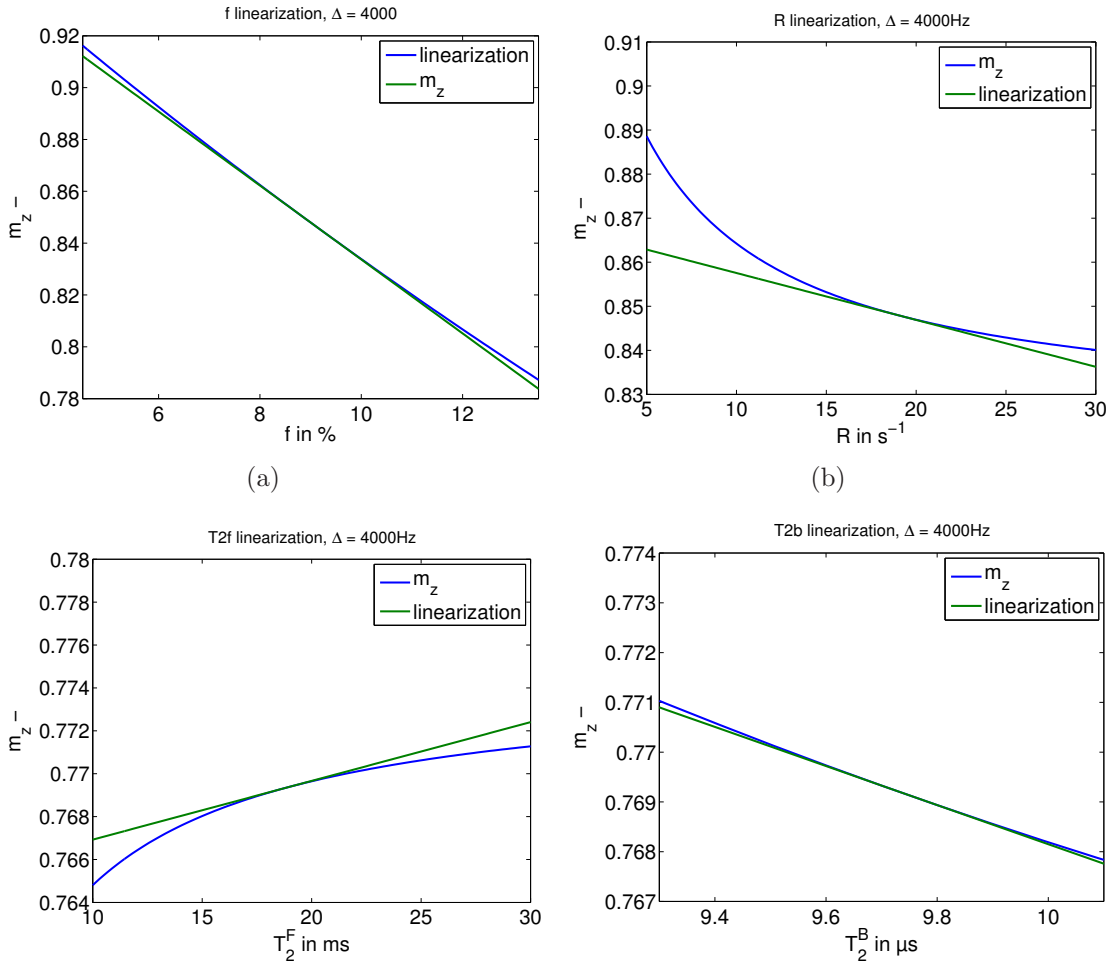

Figure 4.9: Plots of the first-order approximation for an off-resonance frequency $\Delta = 4kHz$ with four parameters (f, R, T_2^F and T_2^B) developed at the means of the synthetic data set.

4.3 BSA Phantom

4.3.1 MT-Images, Correctio-Images, and T_1-map

In Figure 4.10 examples of the acquired BSA phantom images with the FLASH sequence with MT saturation pulse are shown. Each row represents effective flip angle FA_{MT} with increasing off-resonance saturation frequency from left to right. In the top row FA_{MT} is 600°, then in the middle row it is 800°, and in the last one the amplitude is 1000°. The off-resonance saturation frequencies Δ are 600Hz, 2kHz, 4kHz, 8kHz, 8kHz and 96kHz from left to right.

For all investigations the acquired images were normalized with the reference image at 96kHz off-resonance frequency. An example of a normalized image is given in the left image of Figure 4.11 for an off-resonance saturation frequency of 4kHz with an effective saturation flip angle of 600° the saturation pulse . The ROIs, which were used in the analyses, are shown in an overlay in the right image of Figure 4.11 starting with ROI 1 in the top right corner of the image. In the normalized image it can be seen that the BSA cuvettes in top row have less signal intensity (~ 0.7) than the remaining cuvettes (~ 0.9), which have iron added, and also that the intensity in water is nearly identical over the whole volume.

The B_{1+}-map that was used for correction of the excitation angle and the effective saturation flip angle is shown in Figure 4.13 (a), which was dervied from the images with an angle of 40° (b) and 80° (c), respectively. It can be seen that the normalized B_{1+} magnitude increases circular to the middle of the phantom starting with about 0.9 outside and 1.2 in the middle of the phantom.

The $\Delta\omega$-map, and the two phase images with different echo times, are shown in Figure 4.12. In the map one can see two residuals on the left and right side of the phantom. Furthermore it can be observed that in the cuvettes in the top row nearly no frequency shift, whereas with increasing iron concentration the frequency shift increases.

The estimated T_1-map is presented in Figure 4.14 and the estimated mean values within the ROIs are summarized in Table 4.1. The results indicate that water has the highest T_1-times at around 3s followed by the T_1-times of BSA without iron (top row). Then there is a strong decrease of the T_1-times of the BSA cuvettes containing iron starting at around 300ms.

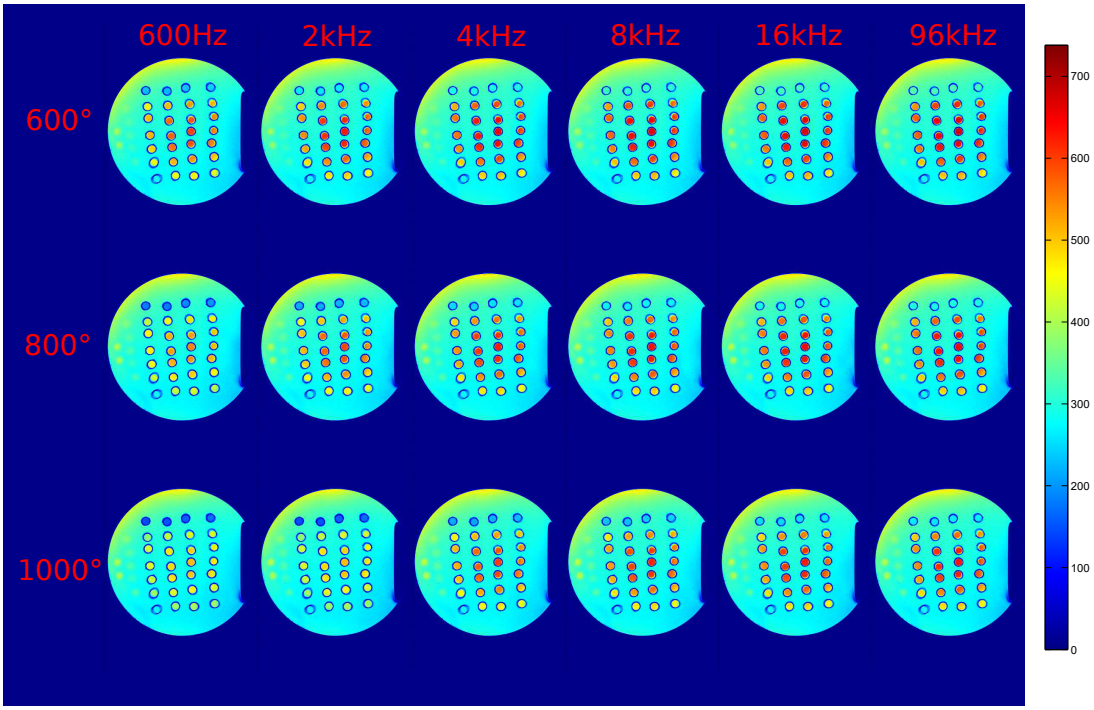

Figure 4.10: Examples of the acquired BSA phantom images. From left to right the off-resonance saturation frequency Δ increases (0.6kHz, 2kHz, 4kHz, 8kHz, 16kHz and 96kHz), and from top to bottom the effective saturation flip angle FA_{MT} increases (600°, 800° and 1000°).

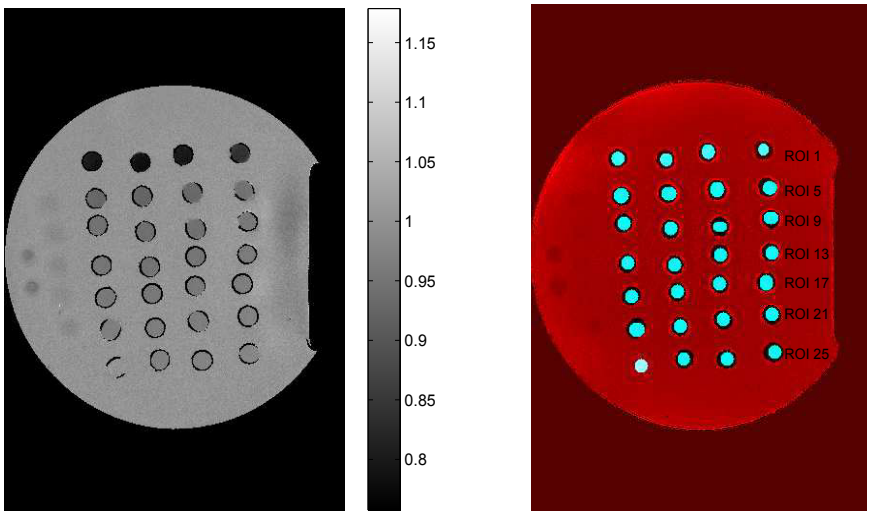

Figure 4.11: The left image shows an example of a normalized image ($\Delta = 4kHz$, $FA_{MT} = 600°$) of the BSA phantom and the right image an overlay of ROIs, which were used for all investigations starting with ROI 1 in the top right cuvette.

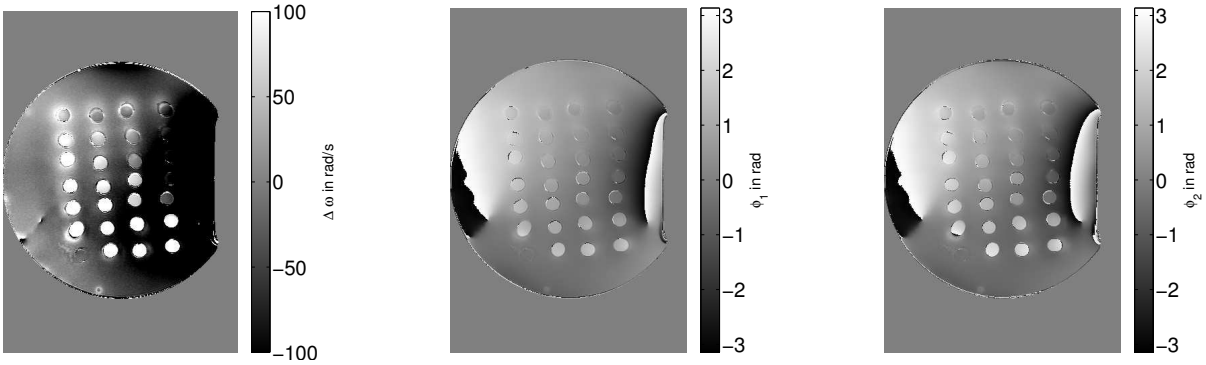

(a) (b) (c)

Figure 4.12: Estimated $\Delta\omega$-map (a) of the BSA phantom. In (b) the phase image with $T_E = 4.1ms$ and in (c) the phase image with $T_E = 6.1ms$ is shown.

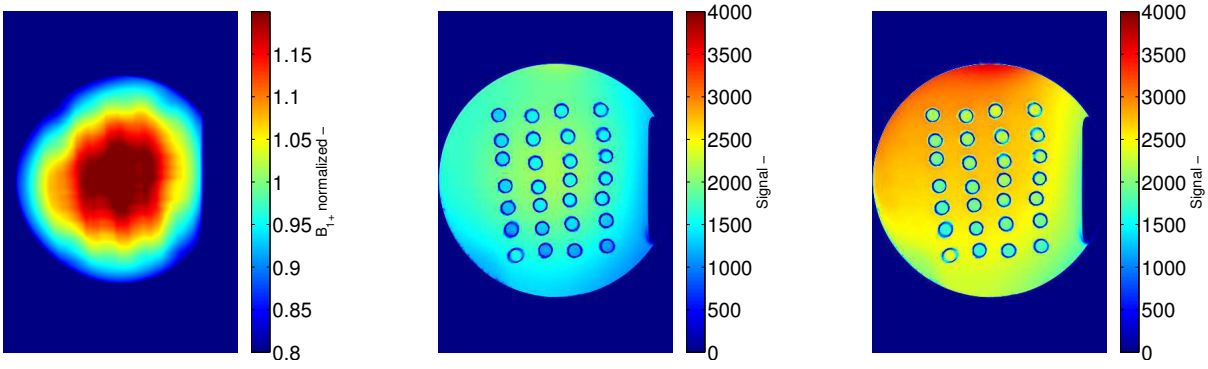

(a) (b) (c)

Figure 4.13: Resulting normalized B_{1+}-map (a) derived from the images with an flip angle of 40° (b) and 80° (c) from BSA-phantom.

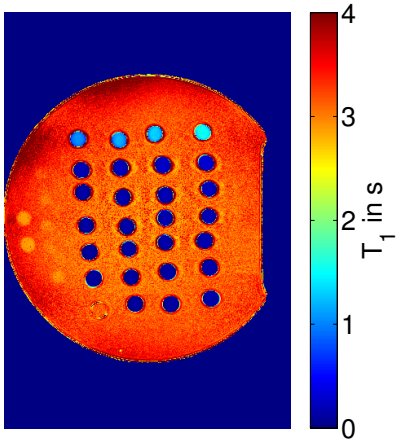

Figure 4.14: Estimated T_1-map of the BSA phantom.

Table 4.1: List of the estimated mean T_1 times within the ROIs of the BSA-phantom.

ROI	[BSA](%)	[Fe](mg/kg)	T_1 (ms)	ROI	[BSA](%)	[Fe](mg/kg)	T_1 (ms)
1	14	0	1529	13	14	75	190
2	18	0	1283	14	18	75	168
3	22	0	1152	15	22	75	144
4	26	0	1020	16	26	75	117
5	14	25	302	17	14	100	175
6	18	25	256	18	18	100	152
7	22	25	251	19	22	100	125
8	26	25	187	20	26	100	101
9	14	50	226	21	14	150	158
10	18	50	195	22	18	150	131
11	22	50	160	23	22	150	109
12	26	50	128	24	26	150	101

4.3.2 Estimation of the Reference Parameters

In this Section the results of the parameter estimation of the pulsed MT-model by fitting the Z-spectra for each off-resonance saturation pulse amplitude and all three off-resonance saturation pulse amplitudes in one global fit are compared.
The results of the four parameter estimations for the BSA cuvettes without iron are listed in Table 4.2 where the parameter are presented as estimated parameter ± the estimated standard deviation of the parameter calculated with Eqn.(3.5). In the last column the residual norm, which is defined in Eqn.(3.3), of the estimated and measured magnetization is listed for each fit.
The results of Table 4.2 indicate that there are major differences between the four approaches for estimating the parameters of the pulsed MT-model. For all BSA concentrations the estimated bound pool fraction is always smaller in the single spectrum fits than with the global fit. When comparing the results for T_2^F one can see that for each of the four approaches the relaxation times decreases with the BSA concentration. However, for each concentration the estimated relaxation times have strong variation depending on the spectrum that was fitted. It can be seen that the T_2^F relaxation times increase with the effective saturation flip angle and that the global fit results are similar to the one with 600°. One thing that have the four fitting approaches in common is that the T_2^B relaxation time is stable for all BSA concentrations ranging from $6.3\mu s$ to $7.1\mu s$.
The most significant difference in the estimated parameters can be seen for the exchange rate k. In the parameter fits with one spectrum the estimated parameter has a range from about $7s^{-1}$ to $2 \cdot 10^5 s^{-1}$ with a standard deviation of the parameters in a similar range. By contrast, with the global fit, k is ranging from $3.1s^{-1}$ to $5.2s^{-1}$ and it can be observed that it increases with the BSA concentration. However, the estimated standard deviation for all four exchange rates is ranging form about 60% to 100% of its fitted value.
With the estimated parameters in Table 4.2 the Z-spectra were calculated for all BSA concentration and effective saturation flip angels. In Figure 4.15 the Z-spectra on the left side were calculated with the estimated parameters from the single spectrum fit, whereas the Z-spectra on the right side were calculated from the global fit results. The circles in the plots indicate the measured data points.
When comparing the Z-spectra of the left side with the right Z-spectra only little differences are noticeable. From the calculated spectra one can see that with increasing FA_{MT} the normalized magnetization m_z decreases. Furthermore that the estimated spectra for 14% BSA have the greatest amplitude over the whole off-resonance frequency range. The lowest amplitudes have the 22% BSA spectra and the spectra of 18% BSA 26% have similar amplitudes, which lie between the amplitudes of the spectra of 14% and 22% BSA.

For the assessment of the quality of the estimated bound pool fraction a linear regression was performed. In Figure 4.16 the linear regression of f for different FA_{MT} is shown in (a)-(c), and in (d) the result of the global fit are illustrated. For all four regressions the resulting line equation of the regression is given in the box of the plots in Figure 4.16. The greatest difference was found to be the slope of the line equation. For the single spectrum fit the slope is between 0.43 and 0.52, which is smaller than the slope of the global fit with 0.58. The offset for all linear regression is similar, ranging from $\sim 3\%$ to $\sim 4\%$.

Table 4.2: Results of the parameter estimation for the BSA cuvettes without iron. Parameters were estimated from the spectrum of effective saturation flip angle FA_{MT} and from a global fit of all three spectra. The last column indicates the residual norm r_{norm} between the estimated and measured normalized magnetization.

BSA(%)	Fitted Spectrum/a	f(%)	k(s^{-1})	T_2^F(ms)	T_2^B(μs)	r_{norm}(-)
14	$FA_{MT} = 600°$	$9.7 \pm 6.2{\cdot}10^{-2}$	$2.1{\cdot}10^{2} + 7.3{\cdot}10^{2}$	$40.4 \pm 7.0{\cdot}10^{-1}$	$6.5 \pm 6.6{\cdot}10^{-2}$	$1.3{\cdot}10^{-4}$
	$FA_{MT} = 800°$	$9.5 \pm 4.9{\cdot}10^{-2}$	$5.4{\cdot}10^{1} \pm 2.4{\cdot}10^{1}$	$53.6 \pm 9.8{\cdot}10^{-1}$	$6.3 \pm 4.3{\cdot}10^{-2}$	$2.7{\cdot}10^{-5}$
	$FA_{MT} = 1000°$	$9.6 \pm 5.0{\cdot}10^{-2}$	$7.2 \pm 6.3{\cdot}10^{-1}$	$59.2 \pm 9.4{\cdot}10^{-1}$	$6.5 \pm 3.7{\cdot}10^{-2}$	$2.3{\cdot}10^{-5}$
	Global Fit	$10.6 \pm 1.5{\cdot}10^{-2}$	3.1 ± 3.1	42.3 ± 0.2	$7.2 \pm 1.4{\cdot}10^{-2}$	$8.7{\cdot}10^{-4}$
18	$FA_{MT} = 600°$	$12.7 \pm 3.0{\cdot}10^{-2}$	$5.7{\cdot}10^{3} \pm 4.0{\cdot}10^{4}$	$31.3 \pm 2.5{\cdot}10^{-1}$	$6.4 \pm 1.9{\cdot}10^{-2}$	$9.3{\cdot}10^{-5}$
	$FA_{MT} = 800°$	$12.0 \pm 3.9{\cdot}10^{-2}$	$1.1{\cdot}10^{3} \pm 4.3{\cdot}10^{3}$	$44.2 \pm 6.2{\cdot}10^{-1}$	$6.2 \pm 2.8{\cdot}10^{-2}$	$5.4{\cdot}10^{-5}$
	$FA_{MT} = 1000°$	$12.2 \pm 4.7{\cdot}10^{-2}$	$1.1{\cdot}10^{1} \pm 7.0{\cdot}10^{-1}$	$45.9 \pm 5.5{\cdot}10^{-1}$	$6.5 \pm 2.6{\cdot}10^{-2}$	$4.8{\cdot}10^{-5}$
	Global Fit	$13.9 \pm 1.4{\cdot}10^{-2}$	3.7 ± 2.3	31.1 ± 0.1	$7.3 \pm 9.5{\cdot}10^{-3}$	$1.2{\cdot}10^{-3}$
22	$FA_{MT} = 600°$	$14.6 \pm 1.9{\cdot}10^{-2}$	$1.5{\cdot}10^{4} \pm 1.1{\cdot}10^{5}$	$25.5 \pm 2.0{\cdot}10^{-1}$	$6.5 \pm 2.4{\cdot}10^{-2}$	$5.0{\cdot}10^{-5}$
	$FA_{MT} = 800°$	$13.8 \pm 1.4{\cdot}10^{-2}$	$7.8{\cdot}10^{3} \pm 4.1{\cdot}10^{4}$	$36.5 \pm 3.2{\cdot}10^{-1}$	$6.3 \pm 2.0{\cdot}10^{-2}$	$3.2{\cdot}10^{-5}$
	$FA_{MT} = 1000°$	$14.1 \pm 5.8{\cdot}10^{-2}$	$1.2{\cdot}10^{1} \pm 7.3{\cdot}10^{-1}$	$36.0 \pm 4.3{\cdot}10^{-1}$	$6.6 \pm 2.6{\cdot}10^{-2}$	$4.1{\cdot}10^{-5}$
	Global Fit	$16.0 \pm 1.8{\cdot}10^{-2}$	4.3 ± 2.9	25.4 ± 0.1	$7.3 \pm 9.8{\cdot}10^{-3}$	$1.1{\cdot}10^{-3}$
26	$FA_{MT} = 600°$	$16.0 \pm 4.0{\cdot}10^{-2}$	$3.7{\cdot}10^{4} \pm 9.6{\cdot}10^{4}$	$19.5 \pm 1.4{\cdot}10^{-1}$	$6.7 \pm 2.6{\cdot}10^{-2}$	$9.3{\cdot}10^{-5}$
	$FA_{MT} = 800°$	$15.5 \pm 3.9{\cdot}10^{-2}$	$1.5{\cdot}10^{4} \pm 2.3{\cdot}10^{5}$	$25.0 \pm 1.8{\cdot}10^{-1}$	$6.4 \pm 3.4{\cdot}10^{-2}$	$2.7{\cdot}10^{-5}$
	$FA_{MT} = 1000°$	$14.7 \pm 5.0{\cdot}10^{-2}$	$1.5{\cdot}10^{3} \pm 5.9{\cdot}10^{3}$	$32.5 \pm 4.3{\cdot}10^{-1}$	$6.2 \pm 2.7{\cdot}10^{-2}$	$7.1{\cdot}10^{-5}$
	Global Fit	$17.5 \pm 2.0{\cdot}10^{-2}$	5.2 ± 4.6	20.2 ± 0.1	$7.2 \pm 9.7{\cdot}10^{-3}$	$1.0{\cdot}10^{-3}$

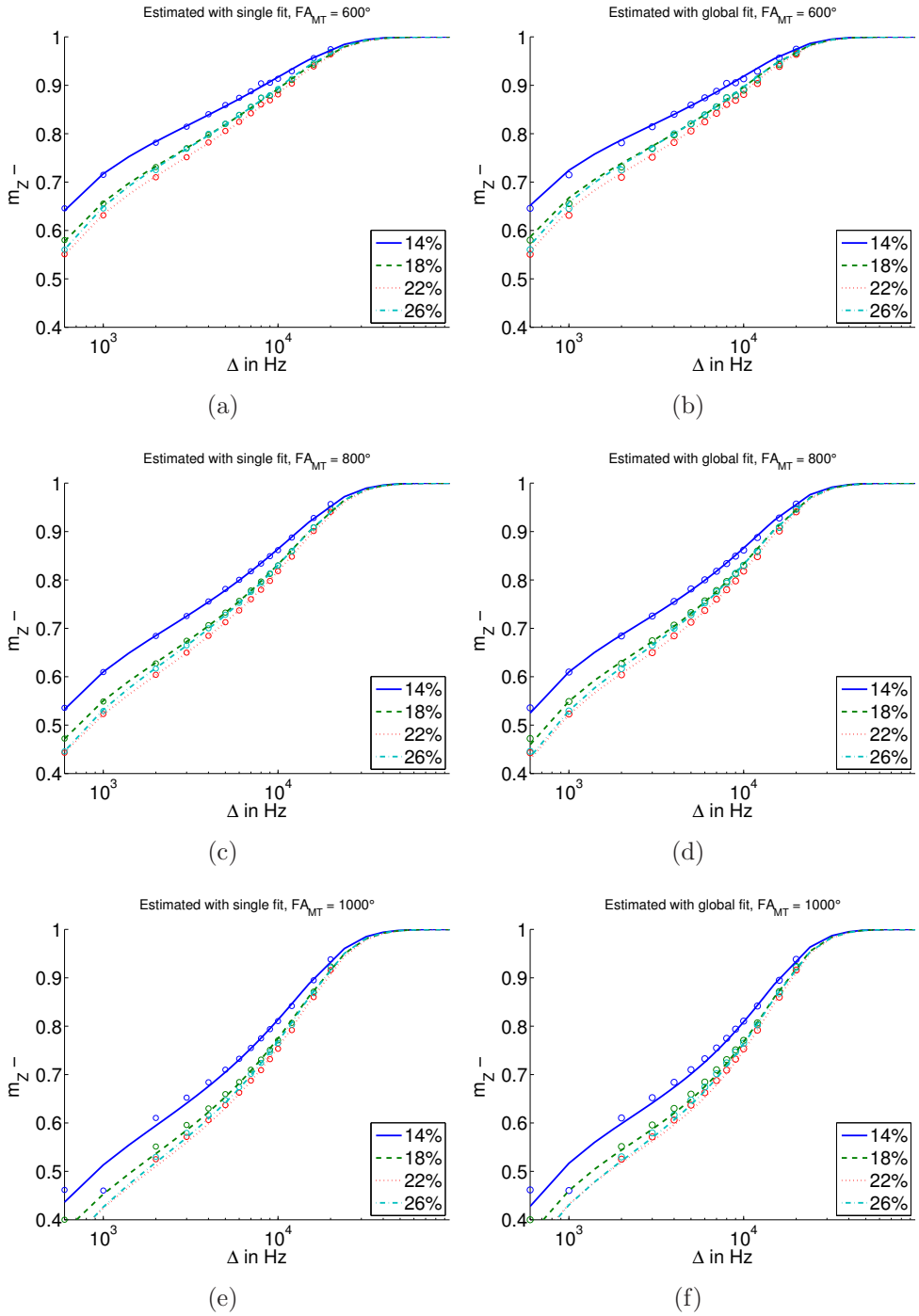

Figure 4.15: Comparison of the fitted spectra for four different BSA-concentrations (14%, 18%, 22% and 26%) with the parameters estimated from measured data points (circles). The plots on the left side (a),(c) and (e) were fitted by a single spectrum fit and on the right side (b), (d) and (f) the global fit results are shown. From the top to bottom the effective saturation flip angle FA_{MT} increases (600°, 800° and 1000°)

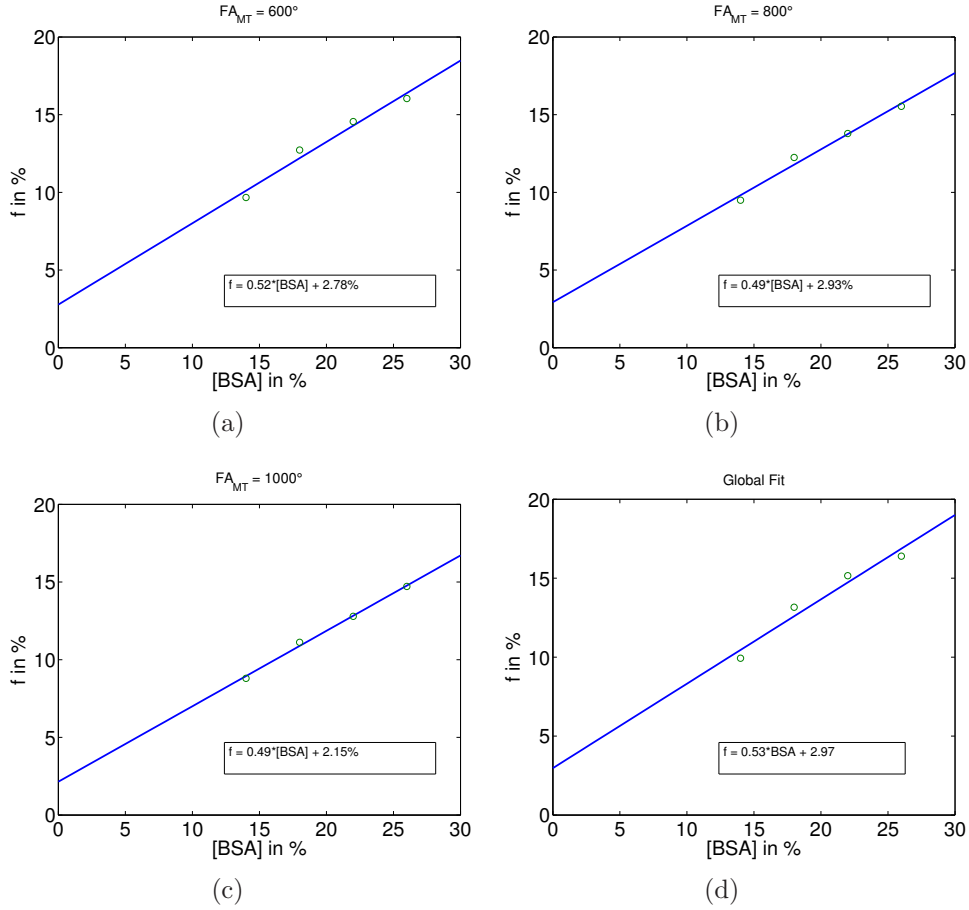

Figure 4.16: Linear regression of the estimated bound pool fraction f from the Z-spectra as a function of the BSA concentration. In (a)-(c) the parameters were estimated by fitting the spectra of each effective saturation flip angle FA_{MT} and in (d) a global fit was performed with the three spectra acquired at the three saturation pulse amplitudes.

4.3.3 Evaluation Single-Point Approach

With the results from the previous Section it was possible to estimate the bound pool fraction from a single off-resonance measurement [14]. In the first step the constrains of the pulsed MT-model were set to the weighted average of the estimated parameters from the global fit listed in Table 4.2, resulting in the follwing values: R = $23.8s^{-1}$, $T_2^F R_1^F = 0.0236$ and $T_2^B = 7.3\mu s$. Then the bound pool fraction was estimated for all off-resonance saturation frequencies with the single-point approach.

In Figure 4.17 results of the single-point approach for the first four ROIs without iron and different BSA concentration are shown. The influence of the effective saturation flip angle is shown in (a) where from top to bottom the estimated images for the three saturation pulses, $FA_{MT} = 600°/800°/1000°$, are illustrated and from left to right the results for the different off-resonance saturation frequencies of the MT pulse from $\Delta = 0.6kHz$ to

$\Delta = 20kHz$ are shown. All these images were estimated with four averages.
In contrast to the saturation pulse amplitude, in Figure 4.17 (b) the influence of the averages on the parameter estimation is shown for $FA_{MT} = 600°$. From left to right the images at different off-resonance saturation frequencies are shown and from top to bottom the influence of averaging on the estimated bound pool fraction is illustrated starting with N = 1 to N = 4 averages.
For all estimated images the mean absolute percentage errors were calculated for all BSA concentrations and number of averages as function of the off-resonance frequency and number of averages N. These results are plotted in the left plots of Figure 4.18. On the right side of Figure 4.18 the results of the numerical error simulations are illustrated. The numerical error simulations indicate similar trends compared with estimated error of the single-point approach. However, it seems that estimated error is a little bit higher than the error predicted by the numerical error simulations.
In Figure 4.17 (a) one can see that the noise level in the lower and higher frequency range is higher than in the middle, especially for 26% BSA. This effect can also be seen in the plots of the mean absolute percentage error in Figure 4.18. Furthermore the results indicate that the error decreases with the number of averages, which can be seen in the images as well as in the error plots.
The minimum of the mean absolute percentage error and the corresponding off-resonance frequency is summarized in Table 4.3 for each measurement. The best result could be achieved with 4 averages and a saturation pulse amplitude of 1000° at a frequency of 3kHz.

Table 4.3: Minimum of the mean total relative error δ_f for the different number of averages N and saturation pulse amplitudes from the BSA-phantom measurements.

N	FA_{MT}	$\delta_f(\%)$	Δ_{min} (kHz)	FA_{MT}	$\delta_f(\%)$	Δ_{min} (kHz)	FA_{MT}	$\delta_f(\%)$	Δ_{min} (kHz)
1	600°	6.2	2	800°	5.4	3	1000°	4.4	3
2		4.6	2		4.12	3		3.7	3
3		4	3		3.7	3		3.3	3
4		3.7	3		3.3	3		3	3

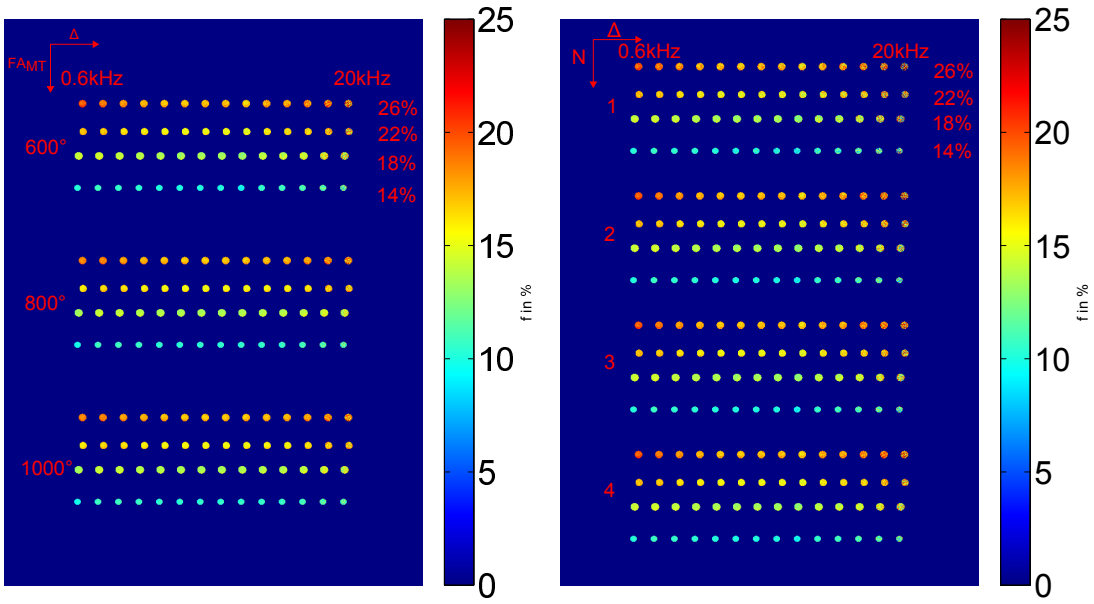

Figure 4.17: Estimated bound pool fraction from the BSA cuvettes (concentrations: 14%, 18%, 22% and 26%) from a single off-resonance measurement. In (a) the influence of the saturation pulse amplitude, FA_{MT} (from top to bottom) and the off-resonance frequency, Δ, (left to right) is shown. The influence of the averages N is shown in (b) from top to bottom for a saturation pulse amplitude of 600°.

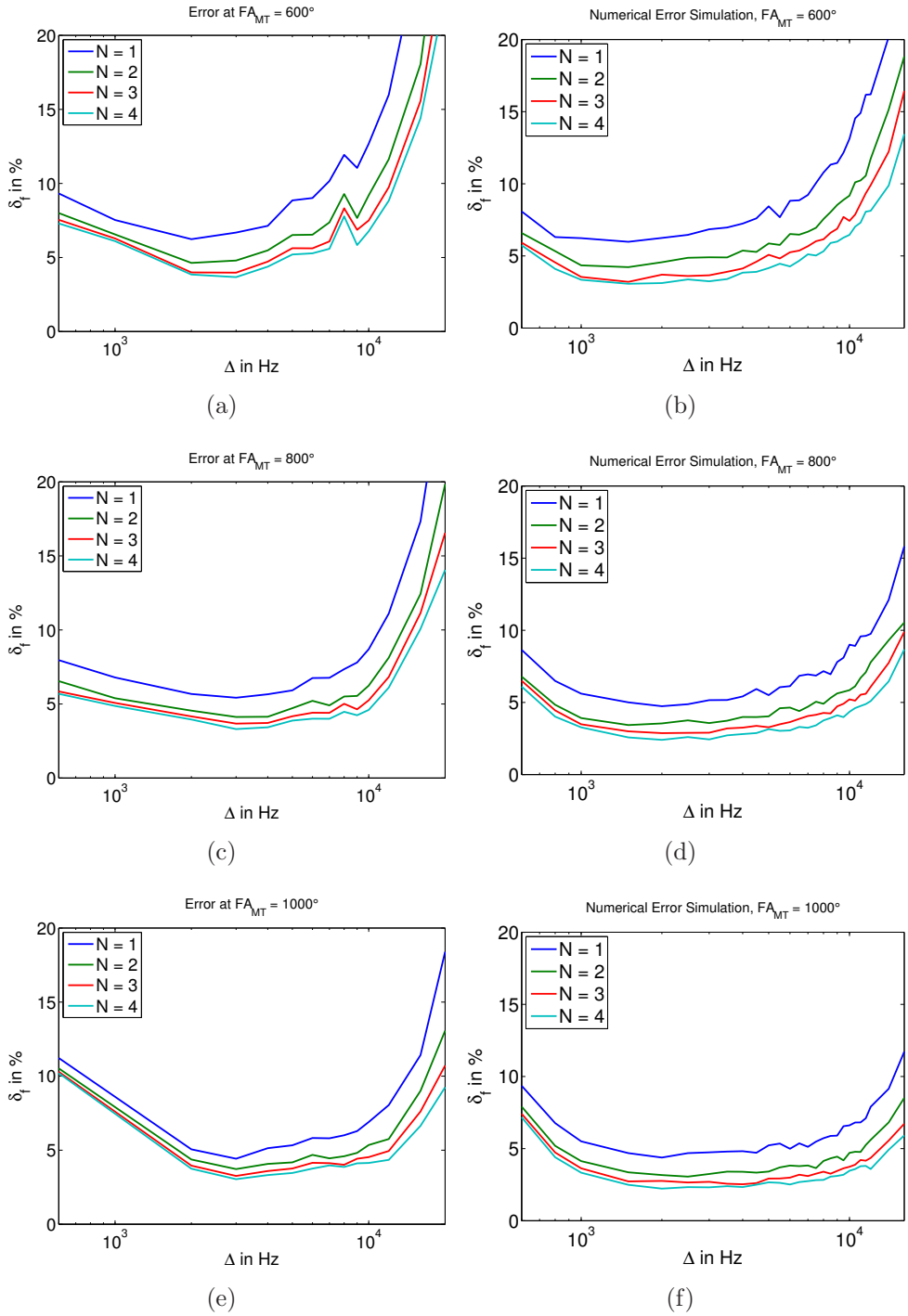

Figure 4.18: Comparison of the estimated (images (a), (c), (e)) and predicted (images (b), (d) and (f)) mean absolute percentage error δ_f of the bound pool fraction estimation from a single off-resonance measurement as a function of the off-resonance frequency Δ. The error was estimated for all three saturation pulse amplitudes FA_{MT} and different number of averaging N.

4.3.4 Influence of the Field Correction Images

In Figure 4.19 the influence of the B_1- and B_0-correction is illustrated. In (a) the reference is shown where both corrections were performed. The other images (b)-(d) show the estimation without B_1-correction, B_0-correction, each and without both.
The greatest influence on the result has the B_1-correction, whereas the B_0-correction has little influence.

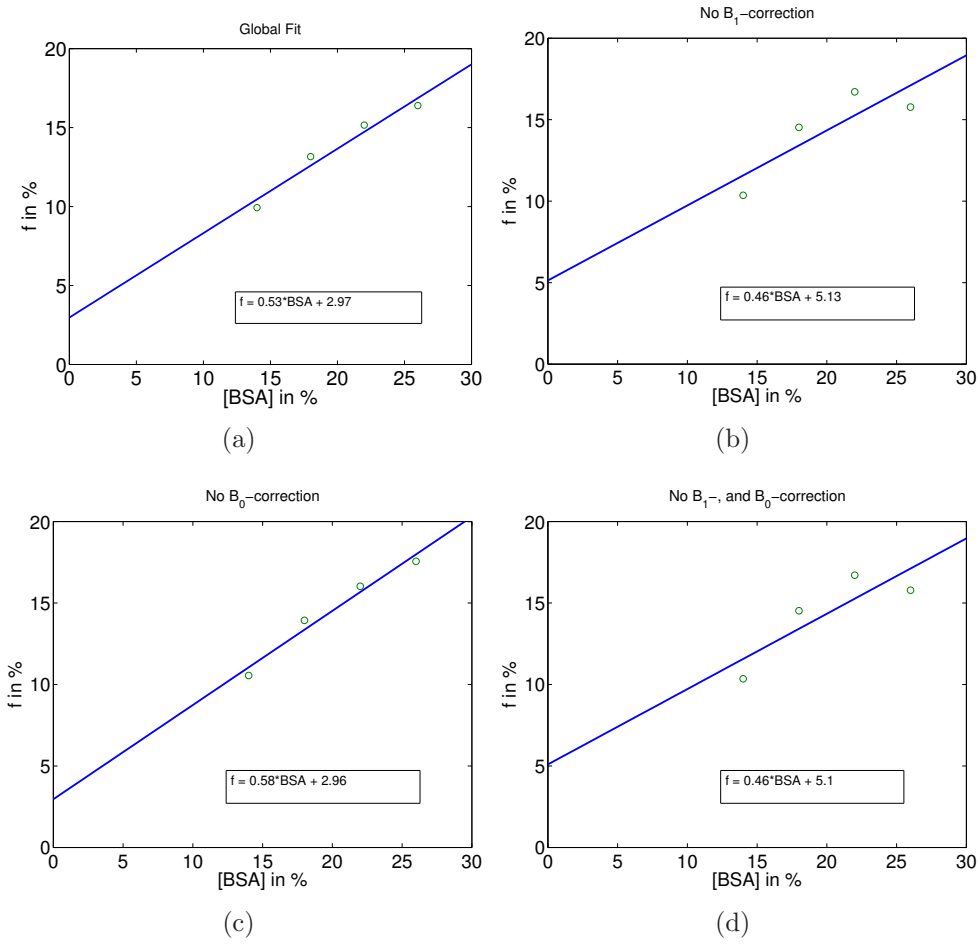

Figure 4.19: Influence of the B_1, and B_0-correction on the estimated bound pool fraction f with the four parameter fit as a function of the BSA concentration. In (a) the f values with B_1-, and B_0-correction are shown for comparison. In (b)-(c) the results without B_1-correction and B_0-correction are illustrated and in (d) the result without B_1-correction and B_0-correction is presented.

4.3.5 Influence of $T_{1,obs}$

The results from the BSA-cuvettes that contain iron are shown in this Section. In Figure 4.20 the estimated bound pool fraction as a function of the BSA concentration is illustrated for six different iron concentrations starting with the cuvettes without iron in the top left corner. From the slope of the functions one can see that there is a trend that the estimated bound pool fraction is lower than in the cuvettes without iron. In the cuvette without iron the slope is 0.54, whereas in the cuvette with the highest iron concentration (shortest $T_{1,obs}$) the slope is 0.37.

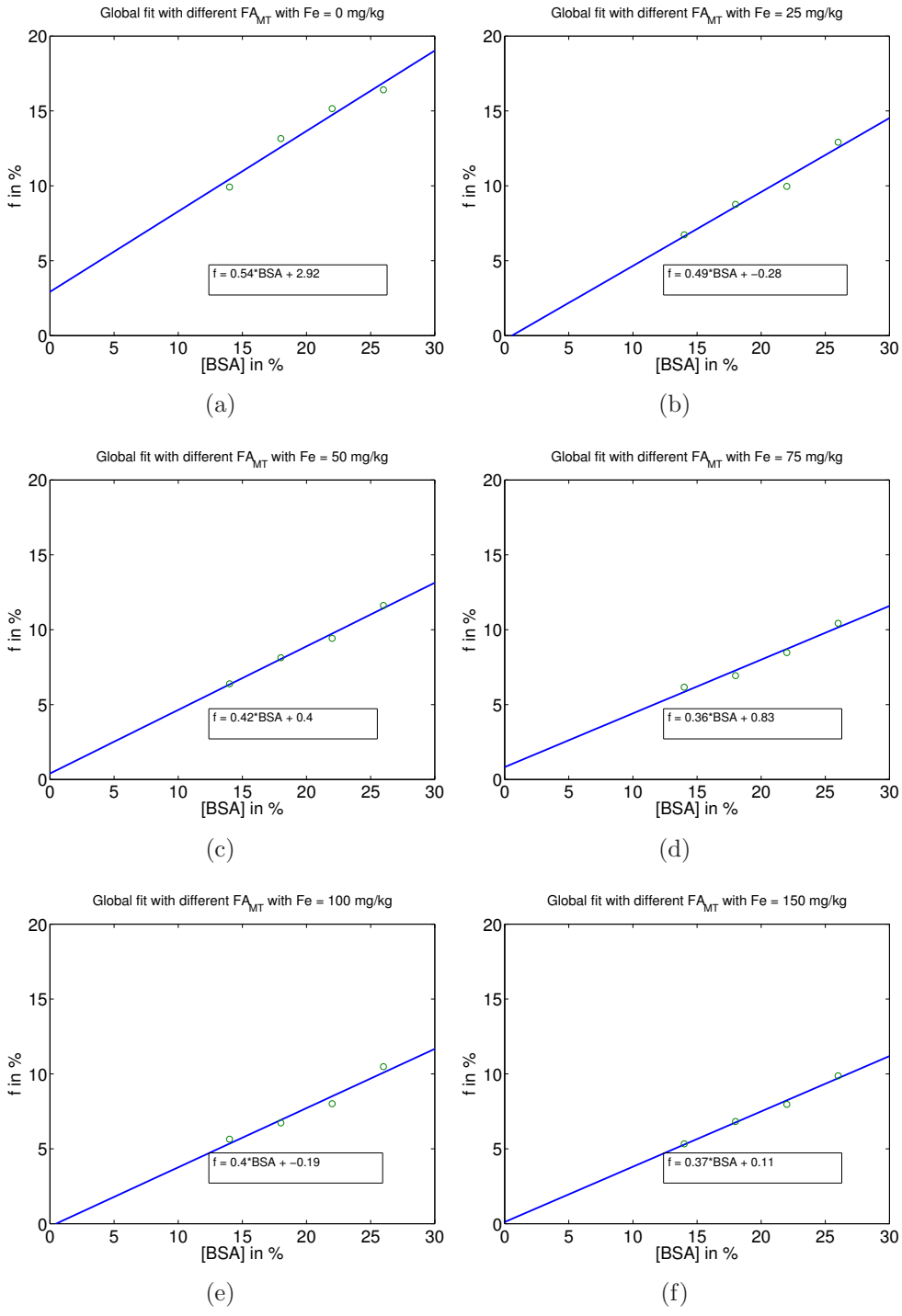

Figure 4.20: Results from the four parameter fit of BSA-cuvettes that contain iron. Each plot represents the estimated bound pool fraction as function of the BSA concentration for one iron concentration.

4.4 Post Mortem Measurements

In Figure 4.21 (a) and (b) field correction images with the estimated normalized B_{1+}-map and the $\Delta\omega$-map are shown. The T_1-map is illustrated in (c), and in (d) one example of a normalized MT images at $FA_{MT} = 600°$ and $\Delta = 4kHz$ is presented.
The parameter maps estimated with the four parameter fit of the acquired post mortem brain images are illustrated in Figure 4.23 and the relative confidence intervals of the estimated parameters are presented in Figure 4.25. Despite for the exchange rate k, where the relative confidence interval is ± 10% of the estimate value in WM, the confidence intervals indicate a good quality of fit.
In Table 4.4 the median values of the parameters and the estimated T_1-times of the brain, in WM, and in GM are summarized. Values were evaluate with a WM and GM mask shown in Figure 4.22. One can see that the f-map has a good WM to GM contrast, which is also represented in the median values of the bound pool fraction where WM has a higher bound pool fraction f (18.1%) than GM (11.7%). With the k-map it is also possible to distinguish WM and GM, but the contrast is not as good as with the f-map since the median values are closer together. Little contrast between WM and GM can be seen in the T_2^F-map. The highest values were found to be in the gyri of the fresh PM brain. From WM to GM T_2^F decreases from about 26ms to 21ms.
The T_2^B-map shows only little variation in the brain regions, which are hardly visible in the image. The median values in Table 4.4 indicate that the T_2^B in WM ($9.7\mu s$) is slightly higher than in GM ($8.4\mu s$).
A comparison of the estimated f-map and an image of the PM sample is illustrated in Figure 4.24. It shows that the f-maps has a better contrast compared with the image of the PM sample.

Table 4.4: Estimated parameters and T_1-times of the fresh post mortem brain slice in the brain (defined as mask from WM + GM), WM and GM. Values are presented as: MEDIAN (1st quartile, 2nd quartile)

	f (%)	k (s^{-1})	T_2^F (ms)	T_2^B (μs)	T_1 (ms)
Brain	13.5 (10.5, 17.7)	2.1 (1.5, 2.9)	22.4 (19, 27.9)	8.8 (7.6, 9.6)	1253 (973, 1467)
WM	18.1 (15.8, 19.5)	3.1 (2.6, 3.5)	20.5 (18.6, 22.1)	9.7 (9.2, 10.2)	918 (876,1000)
GM	11.7 (9.7, 14.1)	1.8 (1.2, 2.2)	25.9 (20.5, 30.8)	8.4 (7, 9)	1391 (1260,1533)

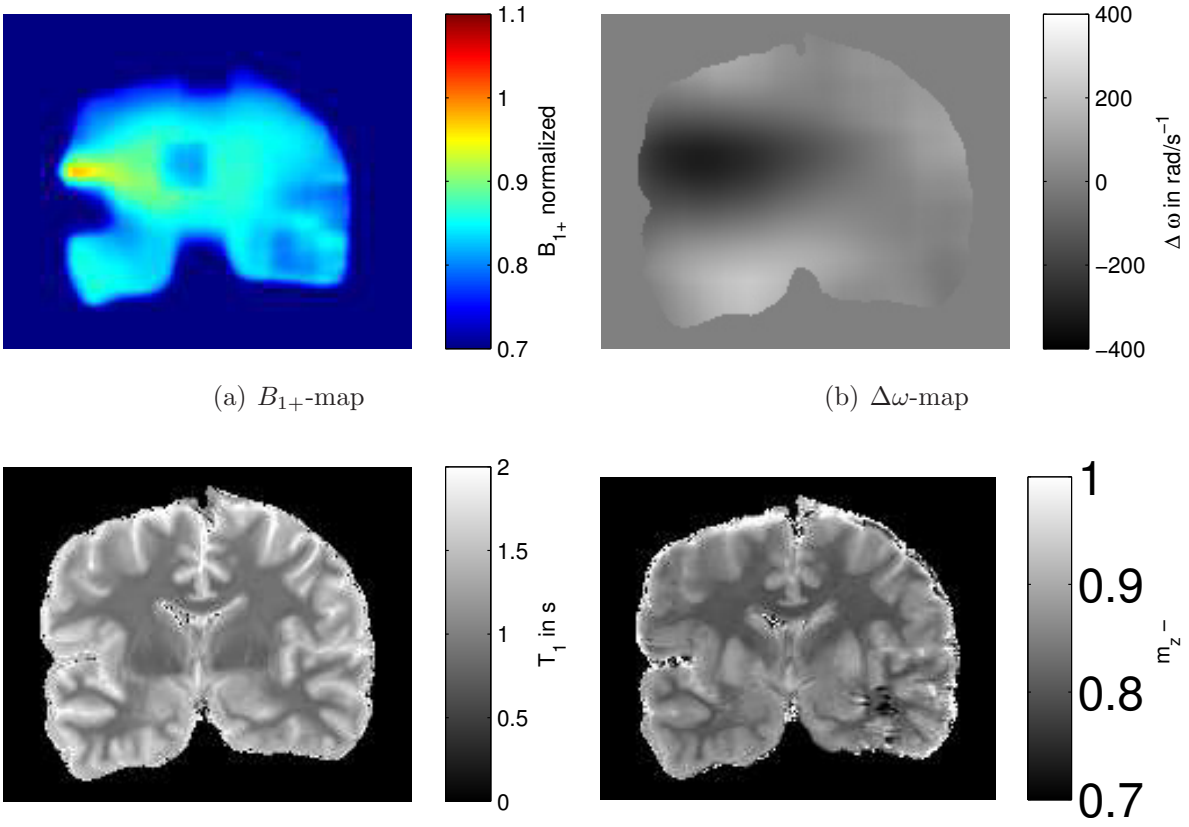

(a) B_{1+}-map (b) $\Delta\omega$-map

(c) T_1-map (d) m_z

Figure 4.21: Calculated normalized B_{1+}-map in (a) and $\Delta\omega$-map in (b) for the field corrections within the post mortem brain. T_1-map is shown in (c), and an example of a normalized image at $FA_{MT} = 600°$ and $\delta = 4kHz$ is illustrated in (d).

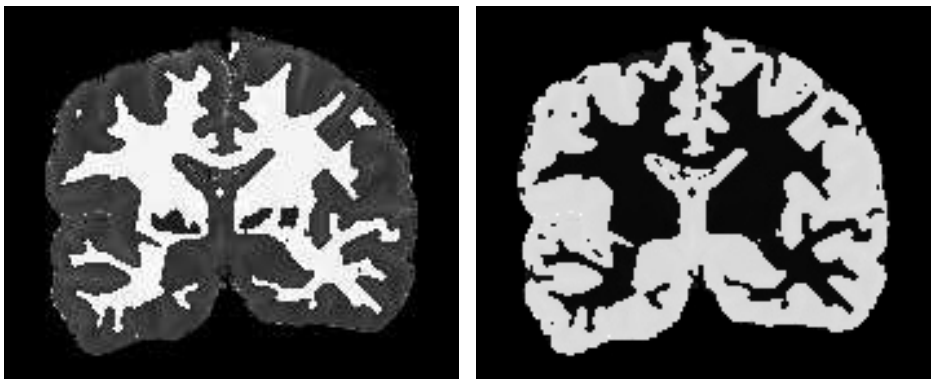

(a) (b)

Figure 4.22: Overlay of the WM-mask (a) and GM (b) with the T_1-map that were used for the analyses.

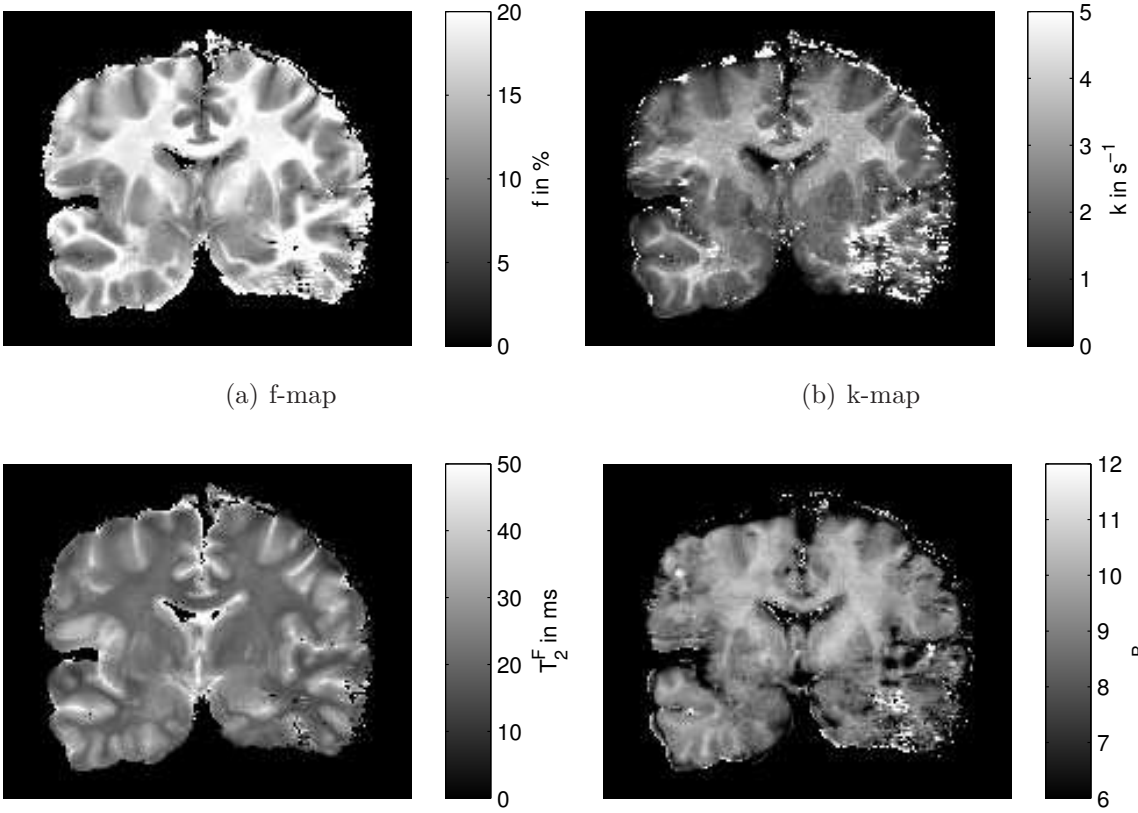

(a) f-map (b) k-map

(c) T_2^F-map (d) T_2^B-map

Figure 4.23: Estimated parameter maps of the fresh post mortem brain.

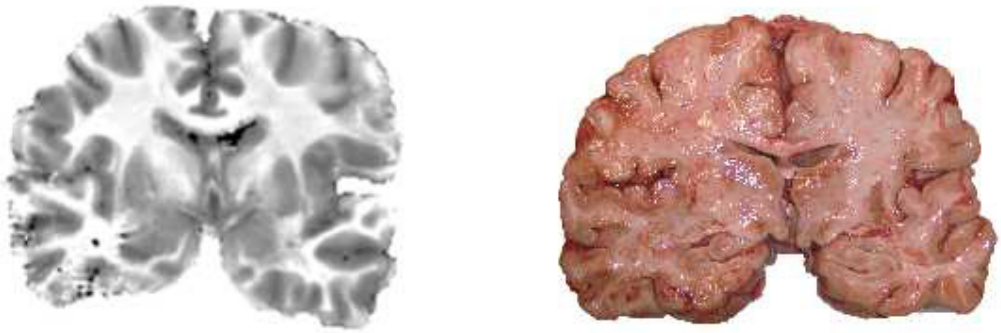

(a) f-map (b) fresh PM sample

Figure 4.24: Estimated f-map (a) from the four parameter fit compared with a picture of the fresh PM sample (b).

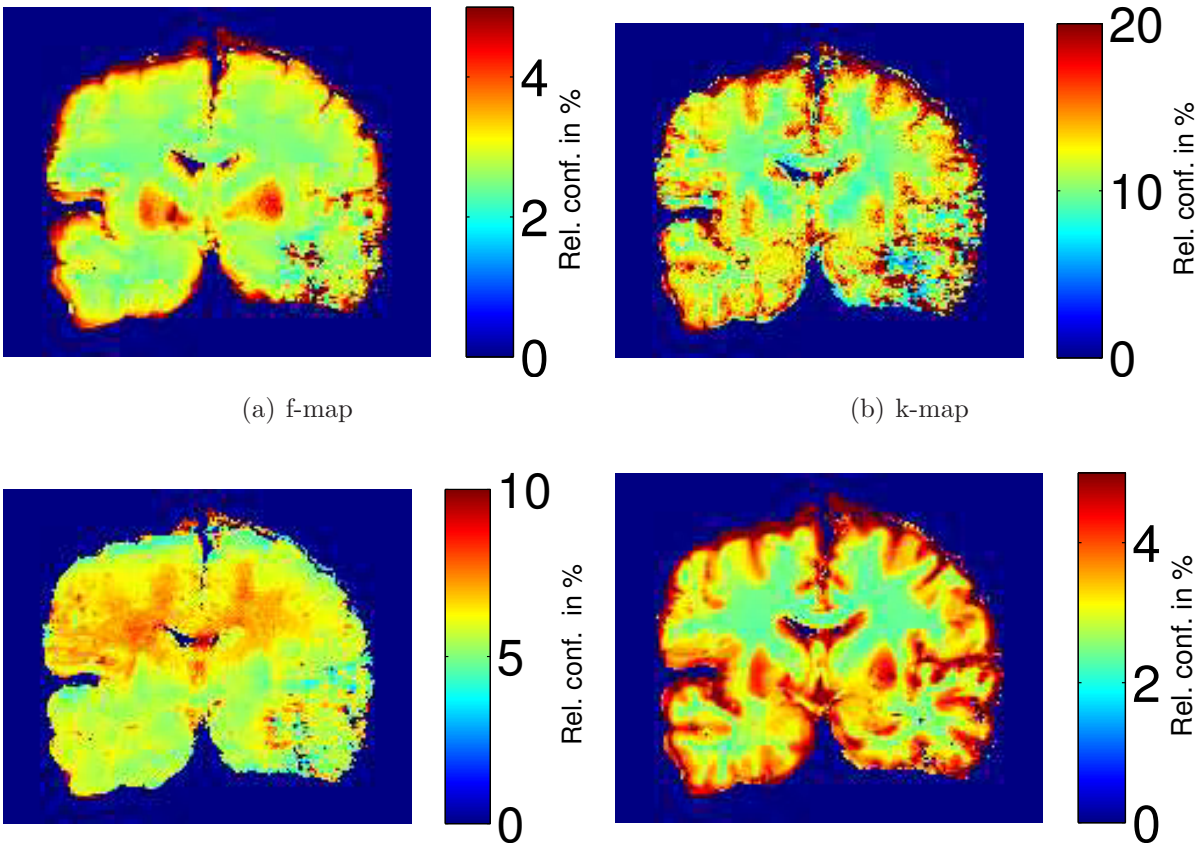

(a) f-map

(b) k-map

(c) T_2^F-map

(d) T_2^B-map

Figure 4.25: Relative confidence intervals for the estimated parameter maps.

4.4.1 Single-Point Approach

Before performing the fast bound pool fraction estimation the constrains were set to the results of the four parameter fit of the fresh post mortem brain listed in Table 4.4.
The mean absolute percentage error and the results of the numerical error simulations for the different effective saturation flip angles, off-resonance saturation frequencies and number of averages are illustrated in Figure 4.26. In each row the calculated error in the left plot is compared with the numerical error simulations in the right plot for the same effective saturation flip angle. It can be seen that the minimum of the simulated error function is at higher off-resonance saturation frequencies and furthermore that the error is slightly higher than the minimum of the estimated error. Moreover that for the estimated error, as well as the simulated error, decreases with the number of measurements. A detailed listing of the estimated error at the minimum is given Table 4.5.
It indicates that the greatest error is 4.25% and the smallest is 3.11% at an off-resonance saturation frequency of 4kHz and an effective flip angle of 600° with 4 averages. Furthermore the results indicate that the error increases slightly with higher effective saturation flip angle.
In Figure 4.27 difference images, with the reference f-map from four parameter fit, for several off-resonance saturation frequencies are shown. They indicate that until an off-resonance saturation frequencies of 3kHz brain structures are visible, which is in accordance with the high mean absolute percentage error in the error plots. In the images between 4kHz to 6kHz visual there is no difference noticeable and then the error increases with higher off-resonance saturation frequencies.
The influence of the different number of averages is illustrated in Figure 4.28 where the estimated f-map with the four-point approach (d) is compared with the images estimated with the single-point approach with 1, 2 and 4 averages (a)-(c) for $\Delta = 4kHz$ and $FA_{MT} = 600°$. Between the f-map with 4 averages and the reference map (d) is visual no difference recognizable, whereas the images with 1 averages and 2 averages are somewhat noisier than the others.

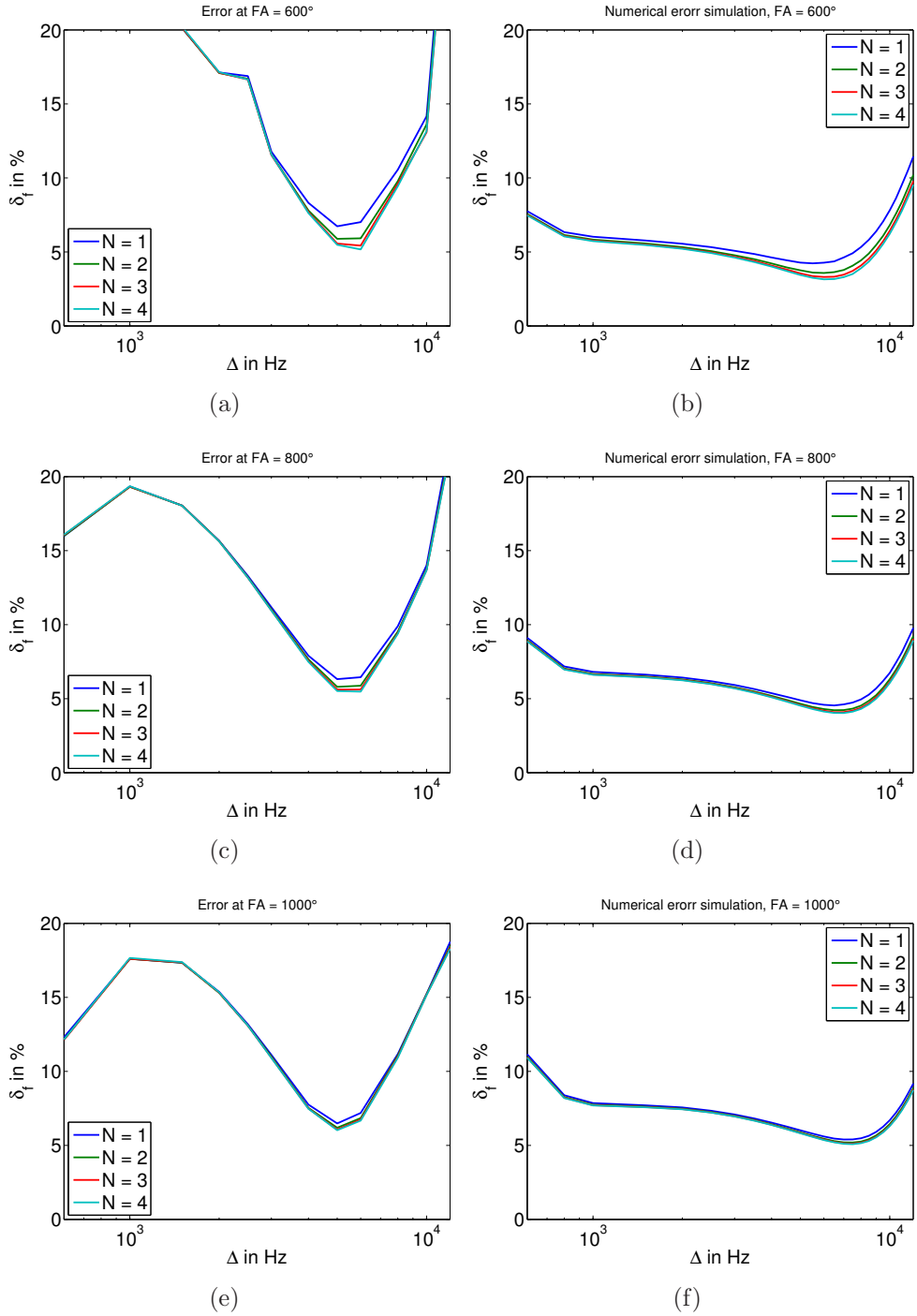

Figure 4.26: Comparison of the estimated error δ_f form the bound pool fraction estimation from a single off-resonance measurement (left images) with the numerical simulations (right images). Each row represents the results for one saturation pulse amplitude FA with four different number of averages N. SNR_{ref} at N=1 was approximately 240.

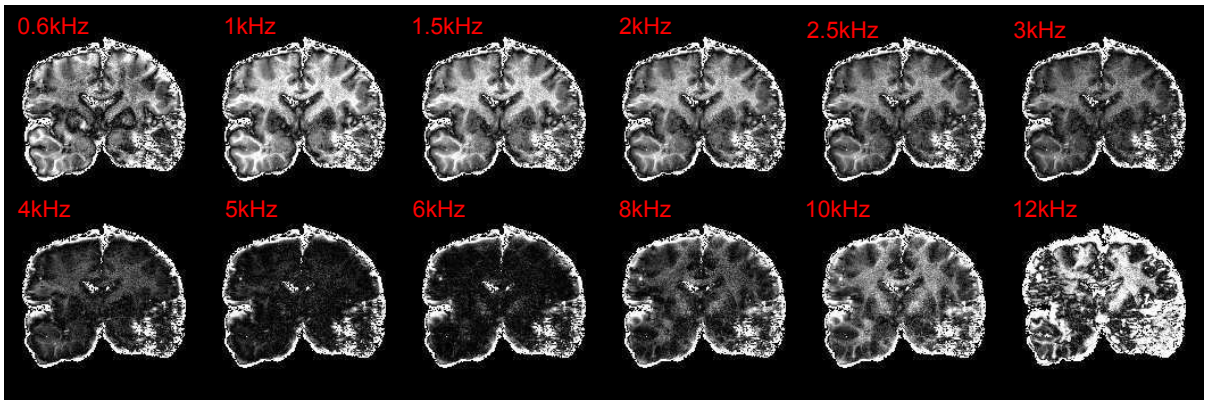

Figure 4.27: Difference maps of the single-point maps ($FA_{MT} = 600°$, 4 averages) and the reference map estimated with the four parameter fit for different off-resonance saturation frequencies (indicated in the top-left of every image).

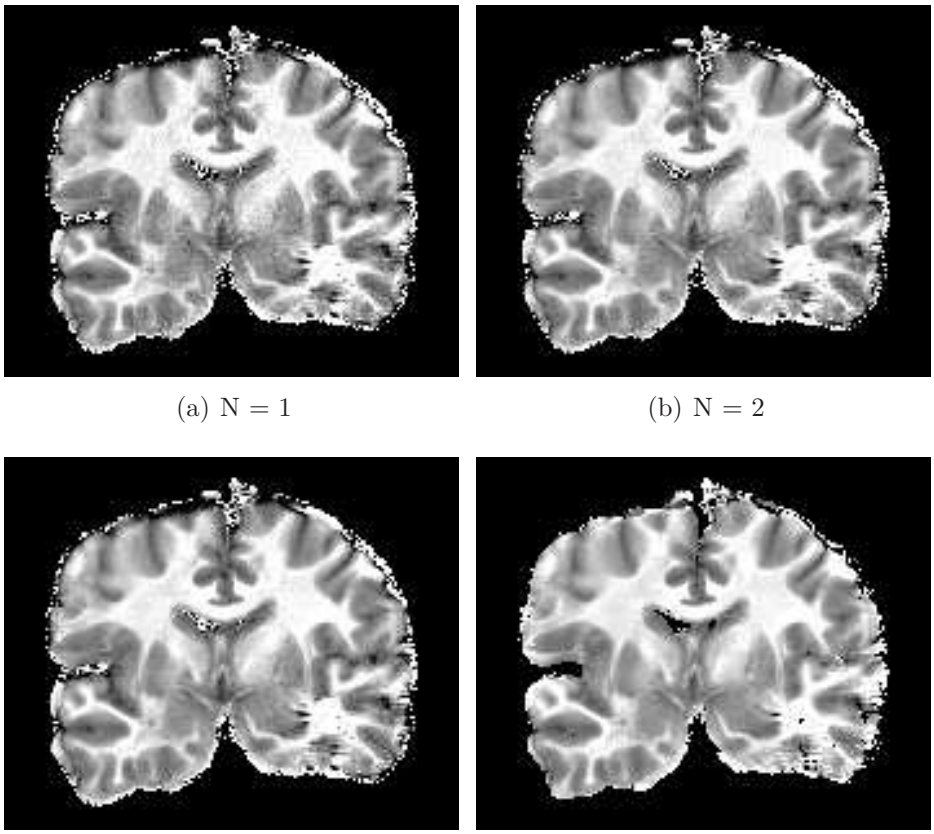

(a) N = 1 (b) N = 2

(c) N = 4 (d) Reference

Figure 4.28: Comparison of f-maps estimated with the single-point approach for 1,2 and 4 averages (a)-(c) and the reference map (d) from the four parameter fit.

Table 4.5: Minimum of mean absolute percentage error δ_f for the different number of averages N and effective saturation flip angles of post mortem brain measurements for the fast bound pool fraction estimation.

N	FA_{MT}	$\delta_f(\%)$	Δ_{min} (kHz)	FA_{MT}	$\delta_f(\%)$	Δ_{min} (kHz)	FA_{MT}	$\delta_f(\%)$	Δ_{min} (kHz)
1	600°	6.6	5	800°	6.3	5	1000°	6.5	5
2		5,8	6		5.8	5		6.2	5
3		5.3	6		5.6	5		6.1	5
4		5.1	6		5.5	5		6	5

4.5 In Vivo Measurements

4.5.1 Parameter Estimation of the Pulsed MT-Model

In Figure 4.29 one slice of the normalized B_{1+}-map (a), the $\Delta\omega$-map (b), the T_1-map (c) and of one normalized MT-weighted image (d) is shown. One can see that most values of normalized B_{1+}-map lie between 0.9 and 1.1 and that $\Delta\omega$ has only small fluctuations from the static magnetic field from about -50 rad/s frontal and about 20 rad/s occipital. With these maps and the remaining normalized off-resonance saturation images the parameter maps of the pulsed MT-model were estimated. An example of the parameter maps is illustrated in Figure 4.30. It can been seen in the Figure that the best WM to GM contrast is given in the f-map. Then the k-map provides only little contrast between WM and GM. Similar to the k-map only little contrast is given in the T_2^F, expect within the gyri and the CSF where the values for T_2^F are greater than 60ms. In the T_2^B map only small differences can be observed between WM and GM.
The normalized confidence intervals of the estimated parameters maps are shown in Figure 4.31. Only small variations of the relative confidence intervals were found for the estimated k-map and in the remaining maps no significant variations in the estimated parameters were observed.
In Table 4.6 the median of the estimated parameter and the T_1-times for WM, GM and the brain are listed. Examples of the masks that were used for the calculations are illustrated in Figure **??** . The results indicate that f is higher in WM (15.5%)than in GM (10.3%) and furthermore that k decreases from WM to GM and that T_2^F increases from 28ms to 35.4ms. No real difference was observed for T_2^B.

Table 4.6: Estimated parameters and T_1-times of the volunteer's brain, WM and GM. Values are presented as: MEDIAN (1st quartile, 2nd quartile)

	f (%)	k (s^{-1})	T_2^F (ms)	T_2^B (μs)	T1 (s)
WM	15.5 (13.9, 17.5)	2.5 (2.1, 2.9)	27.8 (23.3, 31.7)	11.9 (11.1 12.5)	0.8 (0.8, 0.9)
GM	10.3 (8.1, 12.8)	1.4 (1.0, 1.9)	35.4 (28.6, 46.3)	11.0 (10.1 12.0)	1.4 (1.2, 1.6)
Brain	12.5 (9.2, 15.5)	1.9 (1.2, 2.5)	31.5 (26.1, 39.7)	11.4 (10.4 12.3)	1.2 (0.9, 1.5)

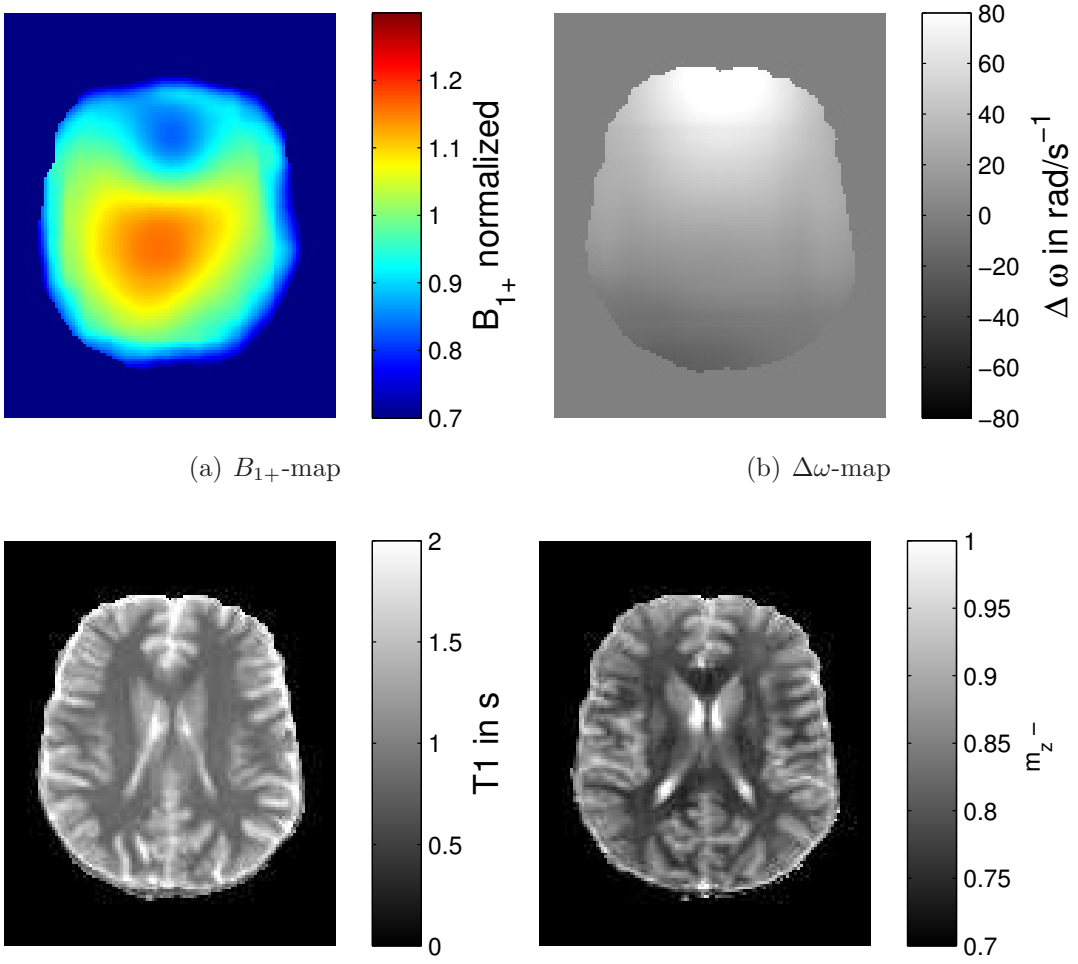

(a) B_{1+}-map (b) $\Delta\omega$-map

(c) T_1-map (d) m_z

Figure 4.29: Calculated normalized B_{1+}-map in (a) and $\Delta\omega$-map in (b) for the field corrections within the brain. T_1-map is shown in (c), and an example for a normalized MT-weighted image is illustrated in (d) with $FA_{MT} = 600°$ and $\delta = 4kHz$.

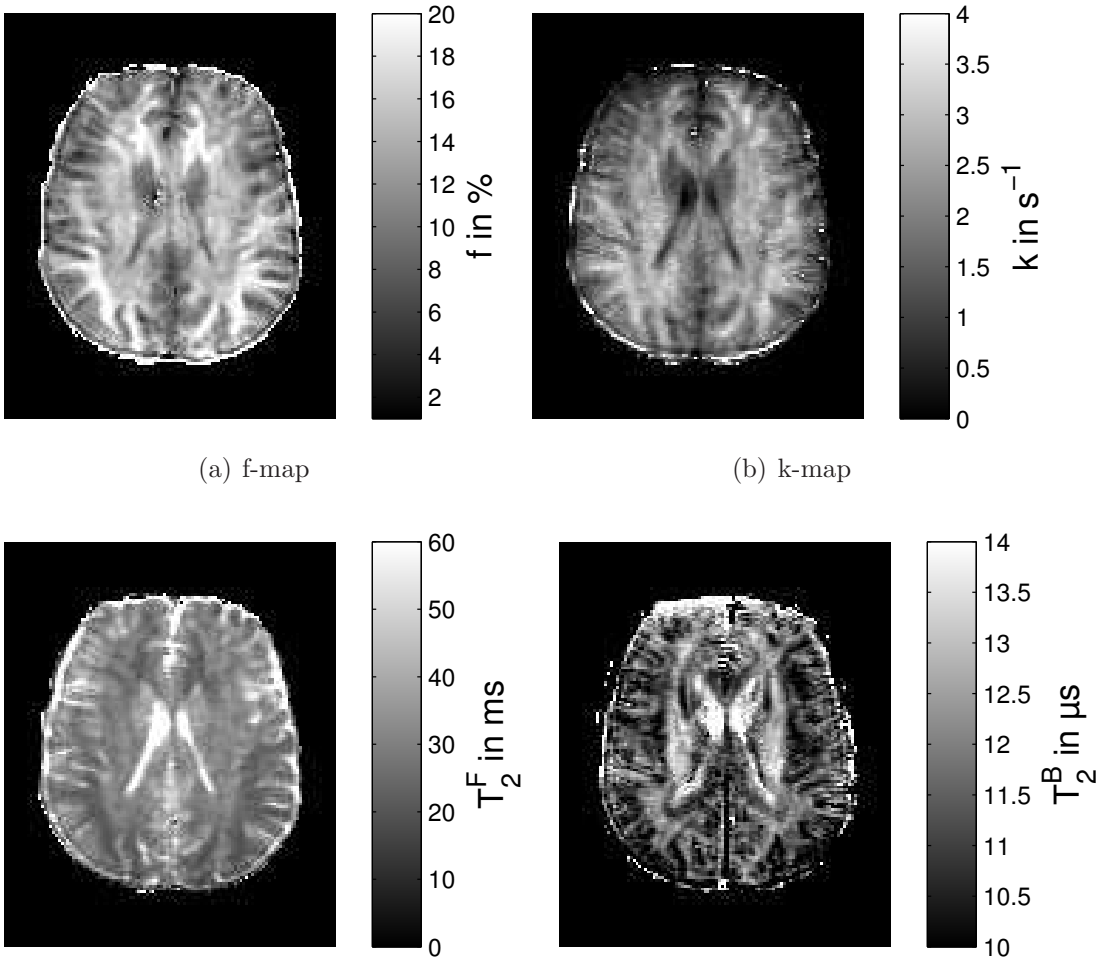

(a) f-map

(b) k-map

(c) T_2^F-map

(d) T_2^B-map

Figure 4.30: Example of the estimated parameter maps from of the volunteer's brain.

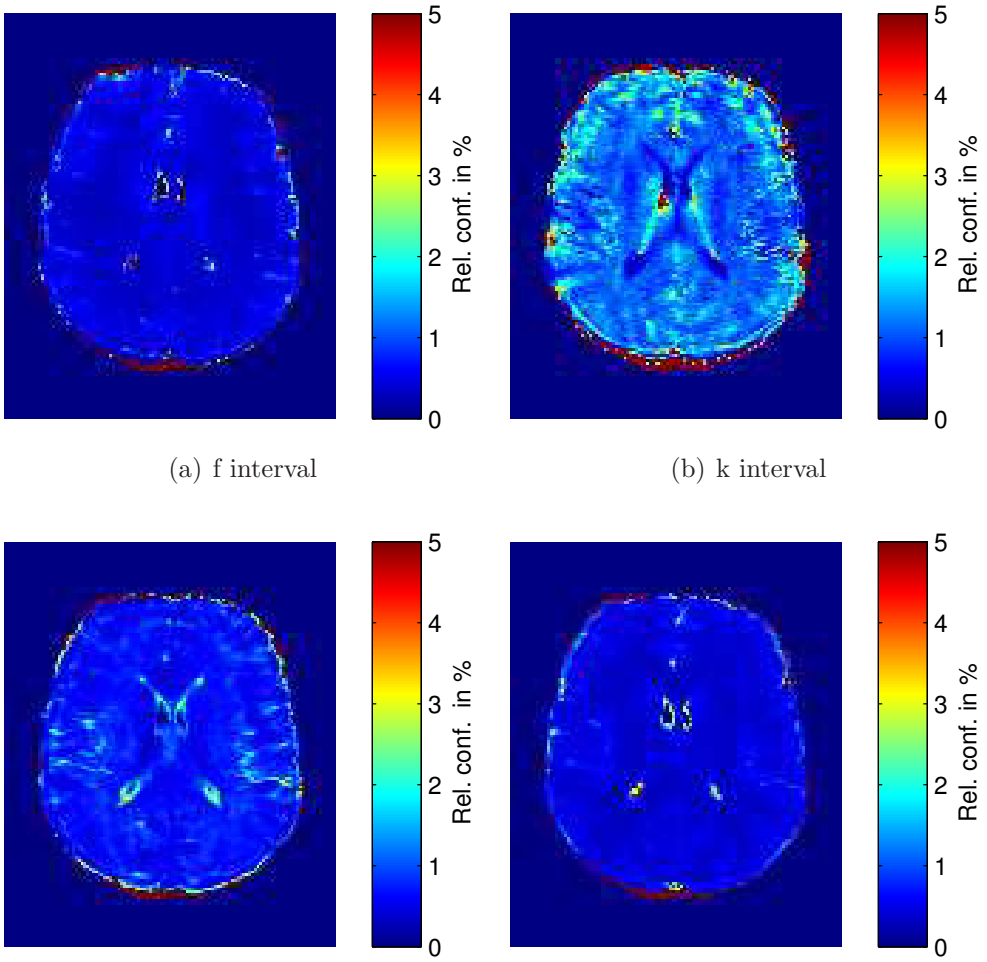

(a) f interval (b) k interval

(c) T_2^F interval (d) T_2^B interval

Figure 4.31: Relative confidence intervals of the parameter fits.

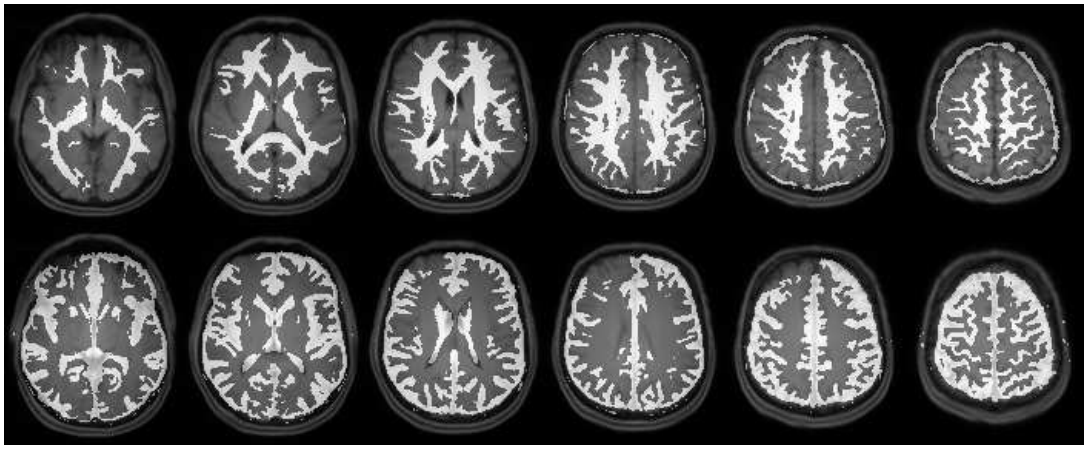

Figure 4.32: Overlay of the WM-mask (top) and GM (bottom) for selected slices (2,4,6,8,10 and 12) with the MPRAGE image that were used for the analyses.

Optimal Sampling Point Single-Point Approach

With the results of the four-point fit from the previous section numerical error simulations were carried out to find the optimal off-resonance saturation frequency and amplitude. For the simulations a complete slice of the estimated parameter maps was used with following constraints: $R = 14s^{-1}$, $T_2^F R_1 = 0.0223$ and $T_2^B = 11\mu s$.
The results of the error simulations for different SNR_{ref} and effective saturation flip angles FA_{MT} are shown in Figure 4.33. The influence of FA_{MT} on the bias and on the error due to noise are plotted in Figure 4.34. It can be seen that the bias increase with FA_{MT} and the errors due to noise decrease with FA_{MT}.
The simulations indicate that the minimum of the mean absolute percentage is at 600° for all different noise levels and furthermore that the minimum of the mean absolute percentage error increases slightly with higher FA_{MT}.
At 600° the smallest error was found at an off-resonance saturation frequency of 4kHz with a SNR_{ref} of 200.

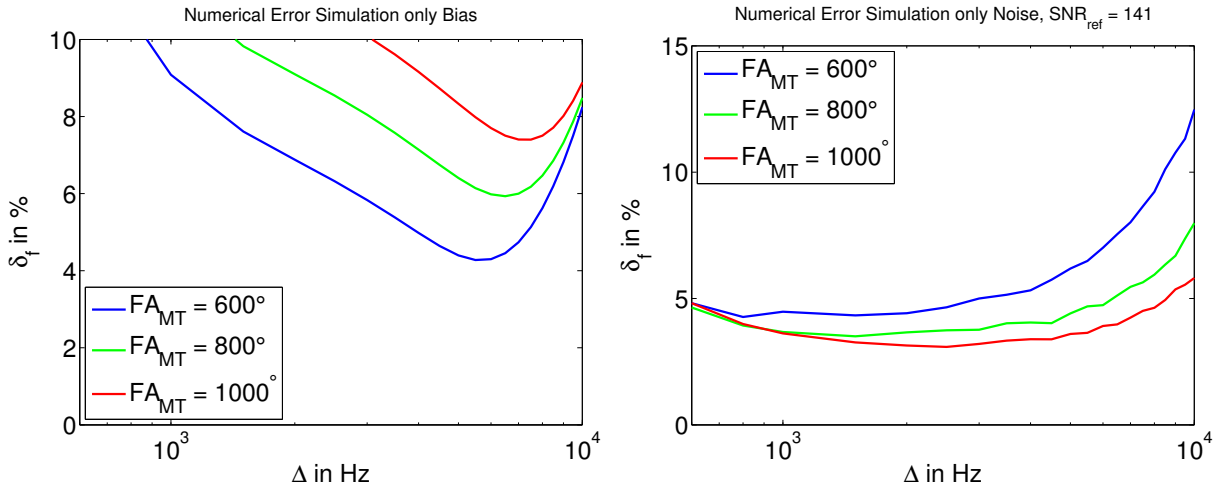

(a) (b)

Figure 4.33: Numerical error simulation results for the single-point approach resulting from one slice of the four parameter fit. In (a) only the simulation results for the bias were plotted (noise is zero) and in (b) only the error due to noise is plotted (bias is zero).

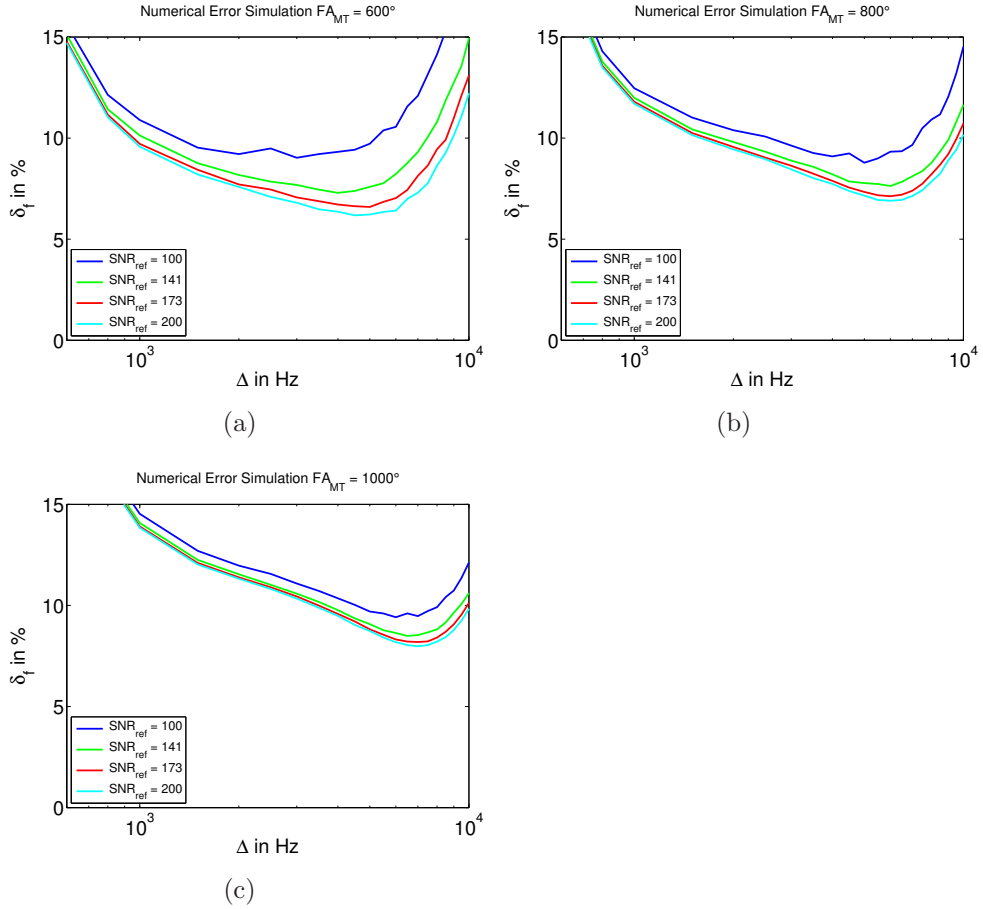

Figure 4.34: Numerical error simulations with different SNR_{ref} and effective saturation flip angle FA_{MT} to find the best sampling point for the single-point method. Simulations were carried out with the parameters estimated in one slice of the four parameter fit result.

4.5.2 Single-Point Approach

With the constraints that were estimated with the four parameter fit in the previous section and the constraints that were found by Yarnykh [14] the single-point approach was used to reconstruct bound pool fraction maps.

In Figure 4.35 f-maps are presented that were reconstructed with the constraints found in this work from the images acquired with $\Delta = 4kHz$ and $FA_{MT} = 600°$. Another example is shown in Figure 4.37 where the same slices of the f-map estimated at 4kHz and 6kHz are compared.

In Table 4.7 the f values of the brain, WM and GM reconstructed with the different constraints are compared. It can be seen that there are small differences in the estimated bound pool fractions. First, the results with the constraints of Yarnykh [14] are smaller for WM, GM and the whole brain compared to the values estimated with the constraints

of the four parameter fit. Second, there are small differences between the off-resonance saturation frequencies. It seems that the estimated f-values are lower at 6kHz with the constraints of Yarnykh [14], whereas with the constraints of this work no common trend could be observed between the two off-resonance saturation frequencies.

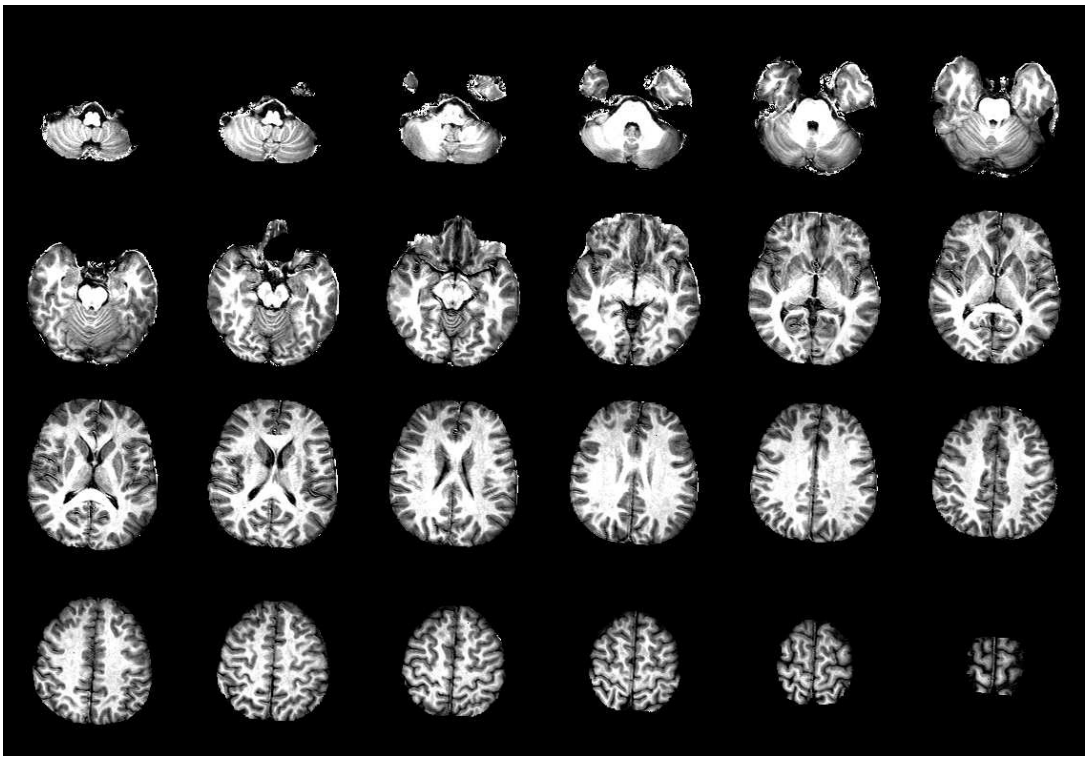

(a) f-map

Figure 4.35: Example of a reconstructed f-map with the single-point approach ($\Delta = 4kHz$, $FA_{MT} = 600°$). constraints of the reconstruction were set to the results the four parameter fit of the previous Section.

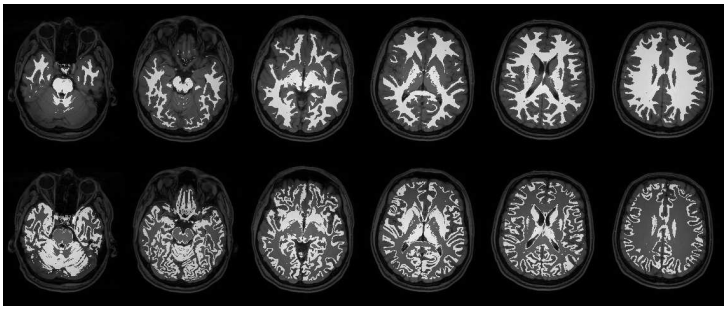

(a) 4 kHz

Figure 4.36: Overlay of the WM-mask (top) and GM (bottom) with the MPRAGE image for selected slices (12,16,20,24,28 and 32) that were used for the analyses.

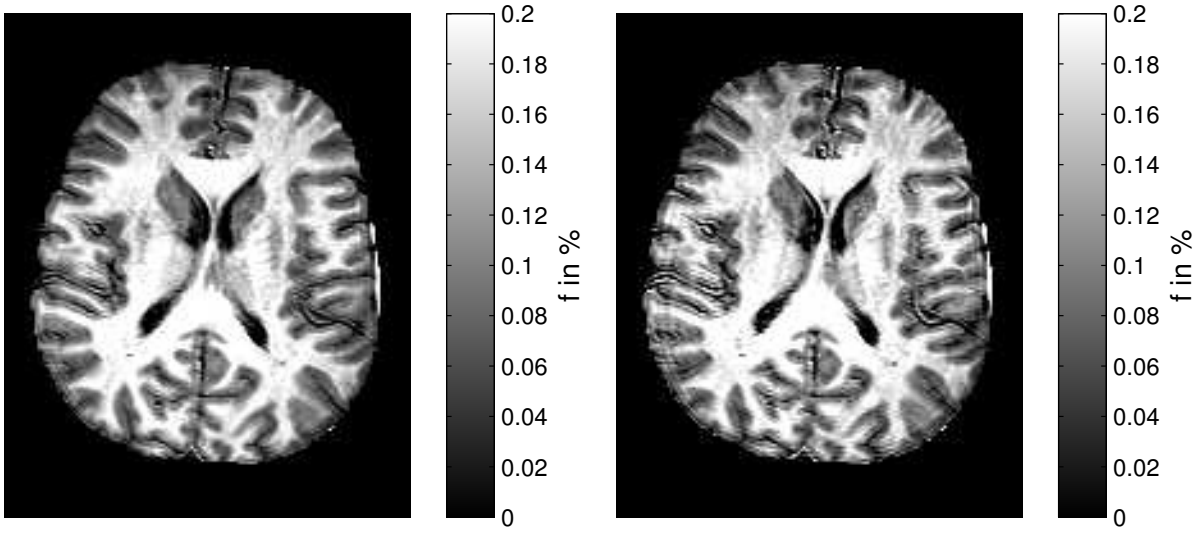

(a) 4 kHz (b) 6 kHz

Figure 4.37: Example of f-maps ($\Delta = 4kHz$, $FA_{MT} = 600°$) estimated with the constraints of the four parameter fit of the previous Section.

Table 4.7: Estimated f-values of the volunteer's brain with the constraints estimated from the four parameter fit and the once recommended by Yarnykh [14]. MT-weighted images were acquired with Delta $= 4kHz, 6kHz$ and $FA_{MT} = 600°$. Values are presented as: MEDIAN (1st quartile, 2nd quartile)

constraints		Δ (kHz)	f (%)	Δ (kHz)	f (%)	T1 (s)
4 parameter fit	WM	4	19.1 (17.2, 21.3)	6	19.0 (16.8, 21.6)	0.8 (0.8, 0.9)
	GM		12.0 (9.7, 14.6)		12.4 (9.7, 15.3)	1.2 (1.1, 1.3)
	Brain		15.8 (11.7, 19.3)		16.0 (11.8, 19.4)	1.0 (0.8, 1.2)
Yarnykh	WM	4	18.8 (16.9, 21.0)	6	18.2 (16.0, 20.8)	0.8 (0.8, 0.9)
	GM		11.9 (9.6, 14.4)		11.8 (9.3, 14.7)	1.2 (1.1, 1.3)
	Brain		15.6 (11.5, 19.0)		15.3 (11.3, 18.6)	1.0 (0.8, 1.2)

5 Discussion

5.1 Coupled Bloch Equations and the Pulsed MT-Model

In the first part of the thesis MT simulations were carried out with the pulsed MT-model proposed by Yarnykh and Yuan [13], which were compared with the results of the coupled Bloch equations, in order to validate the simplifications of the pulsed MT-model. In general the results of this work indicate a good agreement between the coupled Bloch equations and the pulsed MT-model for off-resonance frequencies greater than 1kHz for all physiological reasonable parameter combinations (see Figure 4.3).
However, it seems that there are a small systematic errors since the average deviation between the simulations for off-resonance saturation frequencies greater than 1kHz are in a similar range for all parameter combinations ($\sim 0.1\%$ to $\sim 0.4\%$). The reasons for this small deviation could not be identified, but it is very like that it is due to the modeling of the off-resonance saturation pulse. In Figure 4.2 it can be seen that there is a constant offset of the numerical simulations and the pulsed MT-model during the evolving of the magnetization to the pulsed steady state for each saturation pulse. Furthermore time intervals with free precession, and the solution of the steady state magnetization M_{ss}, can be excluded since analytic solutions of the coupled Bloch equations for both exist.
In literature, no simulations with the pulsed MT-model by Yarnykh and Yuan [13] were found. In 2007, Portnoy and Stanisz [51], performed similar simulations with several different pulsed MT-model including the model of Yarnykh [11]. The earlier model of Yarnykh [11] does not include the direct saturation of the water compared with the model of Yarnykh and Yuan [13]. When comparing the results of Portnoy and Stanisz the smallest average residual deviation for above 1kHz was found to be 0.67%, whereas in this work all average residual deviations are smaller than 0.39%. The slight improvement could be due the additional term for the direct saturation in the model of Yarnykh and Yuan [13]. The influence of the direct saturation is obvious when looking at the Z-sepctra in Figure 4.3 (c) where simulations for three different T_2^F were carried out. Here one can see that the normalized magnetization of the approximations is higher than the result of the

numerical simulations between off-resonance saturation frequencies of 100Hz and 1kHz, which is due neglecting the rotation of the magnetization at low off-resonance saturation frequencies [13]. Therefore the model does not reflect the proper approximation for the coupled Bloch equations for off-resonance saturation frequencies $< 1kHz$.

One critical assumption of the model is the complete spoiling of the transverse magnetization before and after the saturation pulse. Care must be taken if this assumption is valid for the given MRI squence – especially at high repetition rates.

The simulations provided a useful tool to study the complex relations of the two-pool model parameters. In the simulation results for different R_1^F in Figure 4.3 (a) one can see that the normalized magnetization increases with higher R_1^F. This is due to the faster recovery of the longitudinal magnetization within one repetition rate resulting in a greater signal in the pulsed steady state.

Another important aspect for the parameter estimation of the two-pool model indicate the result for the simulations of R_1^B in Figure 4.3 (a). It shows that there is only little difference in the simulations for different R_1^B which supports the approach to set $R_1^B = R_1^F$ for the parameter estimation of the other four two-pool parameters since it is not possible to determine R_1^B from the Z-spectrum [8]. Similar effects can be observed for T_2^B, which supports the constrain for setting T_2^B constant for the fast bound pool fraction estimation from a single off-resonance frequency [14].

When looking at the parameter k and f it is noticeable that with increasing f or k similar trends were observed in Z-spectra, which may results in potential identification problems when estimating the parameters from measured Z-spectra.

5.2 Error Model of Yarnykh Compared with Numerical Error Simulations

A comparision between the error model of Yarnykh [14] and numerical error-estimation reveals some differences between these two methods, although similar trends in both models were observed.
Figure 4.5 (a) illustrates that the estimated bias of the numerical simulations is smaller for all off-resonance saturation frequencies than the predicted error from the error model. In the numerical error simulation the true values (synthetic data) are known, which means that the bias of the numerical error-simulations is correctly estimated, whereas the bias predicted by error model of Yarnykh [14] has small deviations due to the first-order error propagation. To illustrate this issue the first order approximations of the four parameters are shown in Figure 4.9. For the reverse exchange rate R the first-order approximation is only valid for small changes resulting in an error due to the approximation that propagates into the error model. The practical meaning of the approximation error is that the actual bias is smaller than the predicted value of the error model and that the minimum shifts to the right when looking at Figure 4.5 (a).
The simulations results for the influence of noise in Figure 4.5 (b) show that the error model of Yarnykh [14] and the numerical error simulations are different, but the trends of the two curves are similar for different SNR_{ref}. The reason for this deviation remains unclear. One possibility is that the deviation is also due to the first-order approximation.
In the simulations also the influence of the effective saturation flip angle FA_{MT} was investigated. Despite the deviations between the error model and the numerical error simulations similar behavior was observed. As one can see in Figure 4.7 the bias increases with the effective flip angle. This is due to the scaled sensitivity of the parameters, which increases for all four parameters of the model with the effective flip angle (see Figure 2.11) [14]. Therefore a deviation from the actual parameters and the constraints is higher weighted with increasing FA_{MT}.

The purpose of the error model and the numerical error simulations is to choose the best off-resonance saturation frequency and effective flip angle that minimizes the error for the estimation of the bound pool fraction from a single off-resonance measurement. The findings in this work suggest that the numerical error simulation shifts the minimum to the right, mainly due to the bias from deviation of the actual parameters from the constraints, and therefore it could be that f-maps calculated at the optimal off-resonance frequency estimated with the error model of Yarnykh [14] have a greater mean absolute

percentage error, than f-maps estimated at the off-resonance frequency with the numerical simulations.
One limiation of the error model of Yarnykh [14] is that it uses predefined values of f and R_1 for the error estimation, which does does not reflect the biological variability of these parameters. This issue could be easily overcome by extending the numerical error simulations for R_1 and f as well.
Another important aspect for both approaches is that variations in the B_{1+}-field and B_0-field were neglected. A possible extension for both models would be to included this effects with an additional variance in the error estimation.

5.3 BSA Phantom Measurements

The BSA-phantom measurements provided a perfect possibility for the validation of the pulsed MT-model [13] as well as for the estimation of the bound pool fraction from a single off-resonance measurement [14] since acquistion time did not play a crucial role. Compared to the results that were presented by Yarnykh [14] in this work the results provide more information since the validation was performed with more data points and the influence of different SNR was studied more in detail.

5.3.1 Estimation of the Reference Values

In the first step of the evaluation with the BSA-phantom reference values of the bound pool fractions were estimated for the cuvettes. due to the averaging of each ROI and the four images series, it was guaranteed that the best signal to noise ratio was given for the estimation of the reference values, which was used for the validation of the single-point approach.
For the correct estimation of the four parameters of the pulsed MT-model some issues had to be overcome. In the first approach the estimation of the parameters was performed by fitting one Z-spectrum out of the three acquired spectra (one for each effective saturation flip angle) resulting in three parameter set for the same BSA-concentration listed in Table 4.2. At first glance the estimated bound pool fractions for the BSA concentration seemed to be reasonable since they are scaled with increasing BSA concentrations. However, the estimated exchange rates were not reasonable and furthermore the estimated values are not comparable with estimated values for BSA found in the literature [52]. The immense standard deviations of the exchange rates indicate an ill-conditioned problem with the consequence that it is not possible to identify the parameter by fitting just a single

spectrum. The problem could be finally solved by performing a global fit with the three spectra resulting in one parameter set for one BSA-concentration.
Another aspect why it took a while to overcome this issues is illustrated in Figure 4.15 where the fitting results with estimated parameters are plotted. When comparing the Z-spectra of the global fit with the other spectra, derived with the parameters fitted with one spectrum, it is not possible to determine the true parameters for the four BSA concentrations. The only way to determine the most likely solution is to compare the estimated confidence intervals of the fitted parameters. Although the estimated confidence interval with the global fit for the exchange rate are still nearly 100% of the estimated values, but the results are at least stable and reasonable with values smaller than $10s^{-1}$.
The final estimated reference values with the global fit for the four BSA-concentration indicate a good fit. The linear regression of Figure 4.16 (d) shows that the estimated bound pool fraction has a linear dependency, which is to be expected since the fraction of macromolecules increases with BSA concentration. A similar argumentation can be given for the exchange rate, which also increases with the BSA concentration. The decrease of the T_2^F relaxation times is also in agreement with the theory that the mobility of the free proton decreases with the BSA concentration. Compared to the other parameters T_2^B is nearly constant for all concentrations. The only issue is that the linear regression should be zero for pure water. This result might indicate a bias in the pulsed MT-model.
The reference values of the BSA cuvettes from the global fit have similar trends as reported by Mossahebi [52]. Anyway, direct quantitative comparison makes little sense since the BSA concentrations that were used in this experiments are nearly 5 years old.
In these results one interesting linkage between the MTR and the quantitative MT approach can be found. When taking a closer look at the Z-spectra in Figure 4.15 one can see that the curve for 26% BSA has a greater amplitude than the one with 22% BSA, which would result in lower MTR for this sample. This contradicts with the theory that with higher BSA concentration also the MT effect increases. However, the calculated B_{1+}-map, illustrated in Figure 4.13, indicates that the field in the inner (ROI 3) and outer sample (ROI 4) is different. With the correction for the B_{1+}-field within the pulsed MT-model the estimated f value for 26% BSA, is as expected, higher than the value for 22%.
To show the importance of the B_{1+}- and B_0-correction, in Figure 4.19 the corrected results and uncorrected results were compared. The plots point out that the slope of the linear regression changes and also the quality of the linear-regression decreases without B_1-correction. This indicates the importance of a correct B_1-map. The correction of the off-resonance saturation frequency with the B_0-map has little to no influence on the

estimated f-values, which is not surprising since the the B_0-field is nearly homogeneous in the area of BSA-cuvettes without ferritin.

5.3.2 Single-Point Approach

Results of the bound pool fraction estimation from single off-resonance measurement are in agreement with the trends of mean absolute percentage error that have been previously reported by Yarnkyh [14] for brain tissues. In Table 4.3 one can see that the mean absolute percentage error decrease due to the improvement of the SNR.
For all three saturation pulses the error-plots on the left side of Figure 4.18 have a broad minimum over a wide range of off-resonance saturation frequencies and only small differences in the mean absolute percentage error. On the right side of Figure 4.18 the results of the error simulations indicate a good agreement with estimated errors. The simulations predict also a broad minimum of the mean absolute percentage error for a wide range of off-resonance saturation frequencies and amplitudes. The absolute values of the simulations slightly differ form the estimate error, which may result from inaccurate estimation of the SNR of the reference image. The SNR was estimated by diving the mean of a ROI and the standard deviation of the noise in the background. Maybe more accurate methods [53] for the SNR estimation would improve the agreement.
When looking at the error plots in detail of Figure 4.18 (e) for $FA_{MT} = 1000°$ it should be noted that the values at 1kHz off-resonance frequency were excluded from our analyses since this point was recorded with a off-resonance saturation frequency 0.6kHz. This does not affect the results since the mean absolute percentage error has no minimum at 1 kHz. In Figure 4.18 (a) there is a point of discontinuity at 8kHz that could not be explained, but this point is also far away from the minimum.

5.3.3 Influence of $T_{1,obs}$

The findings in Figure 4.20 indicate that the estimated bound pool fraction of the same BSA concentration decreases slightly with decreasing $T_{1,obs}$. However, the two-pool model should compensate the influence of a changing $T_{1,obs}$ as a result from the ferritin.
One explanation might be that due to the high ferritin content the estimation of the T_1-times is not accurate any more. It is know that with higher ferritin concentration T_1 decreases [54], which is in agreement with our results in Table 4.1. One explanation could be that not enough sampling points were acquired in the time interval between excitation of the magnetization and complete relaxation ($\approx 5T_1$) due to the shortening of the T_1. Another aspect is that the short component of the bi-exponential relaxation is measured

rather than the observed relaxation rate $T_{1,obs}$, which also might bias the estimation of the bound pool fraction.
In summary it is very likely that the deviation of the slope of the bound pool fraction as a function of the BSA concentration was induced by measurement errors. Further research has to be done, for example with lower lower ferritin concentrations, to asses the error exactly.

5.4 Post Mortem Measurements

With measurements of the fresh post mortem brain slice it was possible to fit high quality parameter maps of the pulsed MT-model that never have been reported elsewhere.
The analyses of the maps in WM, GM and the whole brain in Table 4.4 shows in general increased two-pool model parameters compared with in vivo data [13, 14]. There are several potential explanations for these results. The imaging of the fresh PM sample was performed with ambient temperature and therefore the relaxation properties of the brain are different compared in vivo measurements [55]. However, it is expected that the T_1-times of WM and GM are smaller compared with body temperature, which is not the case in our results. The reason for the higher relaxation times stays unclear, especially since a IR sequence for T_1-mapping was used with a sufficient long repetition time ($T_R = 12s$).
Besides the temperature, and measurement conditions, autolysis of the brain could also have changed the MRI properties.
The fresh PM measurements provided also a good possibility for the validation of the single point approach. Therefore numerical error simulations were performed and compared with the results of the single-point approach shown. The numerical error simulations are not identical with the estimated error but the same trends could be observed.
The most important aspect of the results of the numerical error simulations is that the minimum of the simulated error and the estimated error is in the same frequency range of $\approx 6kHz$ and also that the predicted error and the measured error have similar magnitude ($\approx 6\%$). Therefore the numerical error simulations are well suited to predict the optimal sampling point for the estimation of the bound pool fraction from a single off-resonance measurement.

5.5 In Vivo Measurements

In the last step of the thesis MRI protocols for the the parameters estimation of the pulsed MT-model and the fast bound pool fraction estimation from a single off-resonance measurement were implemented.

The greatest issue that had to be overcome for the estimation of the pulsed MT-model parameters in vivo was to generate a MRI protocol that allows to estimate the parameters sufficiently good within a moderate scan time. It was found that with seven different off-resonance saturation frequencies (Δ =0.6, 1, 2, 4, 8, 12, and 96 kHz) at two effective saturation flip angles (FA_{MT} = 600°, 1000°) the parameters could be reasonable identified. In the beginning the same sequence parameters as in the work of Yarnykh [14] were chosen, which had a third effective flip saturation flip angle with 800° and the same off-resonance saturation frequencies. However, this led to a protocol with a total scan time greater than 1h. Therefore it was decided to adapt the protocol to just two effective saturation flip angles. One important thing about the choice of the FA_{MT} is that their magnitudes are not close together, otherwise the identification of f and k from the data is not not reliable. Yarnkyh [14] reported shorter scan times for the entire MRI protocol with three effective saturation flip angles with the drawback that the SNR is worse compared to our protocol. Therefore it is believed that in total our results have the same quality as the parameter maps reported by Yarnkyh [14]. Also the results of the relative confidence interval maps from the estimated parameters indicate that the quality of the fit is sufficient good. Despite of the relative confidence intervals for k, all the other maps show no noticeable variations. The variations for k can be exampled due to an identification problem of f and k. The confidence intervals of k are still small and therefore these scan parameters can be recommended for the estimation of the two-pool parameters in vivo since the total scan time was about 45min for the entire protocol.

The two-pool parameters that were found in this work indicate considerable differences to values found by Yarnkyh [14]. It seems that in our work the values for the bound pool fraction are higher. For example in WM we report a median of 15.7%, whereas Yarnykh [14] estimated a mean value of 14.2% and even more significant is the difference for GM, where we report 10.4% and Yarnykh [14] estimated 7.6%. Furthermore the exchange rate k is also not in accordance with the literature. In the work of the Yarnykh and Yuan [13] an exchange rate of $3.3s^{-1}$ and $1.6s^{-1}$ was reported for WM and GM, whereas in our work the values are $2.5s^{-1}$ and $1.4s^{-1}$. Also the T_2^F values seem to be a little lower for WM and GM compared with the results of Underhill [56]. The only parameter that is in the same order as in the literature is T_2^B [11, 57].

One possible explanation could be that differences in the T_1 estimation propagated into the parameter maps. Yanykh [14] reports a T_1 relaxation time of 0.9s for WM, whereas we estimated 0.8s. On the other hand in GM the estimated T_1 relaxation times are approximately equal ($1.4s$).

The purpose of the two-pool parameter estimation was to validate the constraints and the optimal sampling for the bound pool fraction estimation from a single off-resonance measurement. As mentioned above the parameter distribution is different in this work, which results also in different constraints compared with the findings of Yarnykh [14]. Anyway, although the parameter distributions are different, the numerical error simulations led to similar results as recommended by Yarnykh [14] for the single-point approach. The optimal FA_{MT} was found in this work at $\approx 600°$ with the minimum error, depending on the SNR of the reference image, between 3kHz to 7kHz off-resonance saturation frequency. Therefore two MT-weighted images with an off-resonance saturation frequency of 4kHz and 6kHz at an effective saturation flip angle of were acquired.

Although the estimate f-maps in Figure 4.37 have good WM versus GM contrast, the quantitative values of the f-maps are not satisfying. For example, the estimated bound pool fractions are much higher than the ones reported by Yarnkyh [14] with 19.1% in WM and 12% in GM. These values exceed also the values estimated with the four parameter fit in this work. These deviations are somewhat surprising since the same MRI sequences were used for the four parameter fit with the only difference that the resolution was better. Furthermore the results from the BSA-phantom and fresh PM measurements show that the single-point approach works. One thing that can be excluded are wrong constraints because the f-maps were also reconstructed with the constraints of Yarnykh [14]. In Table 4.7 one can see that the f values are slightly different due to the constraints. However, also with the constraints of Yarnykh [14] the f-values are much higher than in the literature. Therefore the deviation can not be explained by the constraints.

6 Conclusion

The present work investigated in detail the pulsed-Model [13] and further on the fast bound pool fraction estimation from a single off-resonance measurement [14].
The validation of both methods was performed with three different types of measurements (BSA-phantom, fresh pm sample and in vivo measurement) that led to the same results.
The bound pool fraction estimation from a single off-resonance measurement is possible, within acceptable error tolerances, if the following points have been carefully considered. The single-point approach uses constraints that are derived form the parameters of the pulsed MT-model. Therefore inaccurate estimation of the parameters propagates into the error of the fast bound pool fraction estimation due to bad constraints. Once the parameters of a specific tissue have been wrongly identified, it is not possible to determine the correct error of the single-point approach. Therefore the two-pool model parameter has to be measured as accurate as possible. To find the best off-resonance saturation frequency and effective saturation flip angle the numerical error simulations, which were presented in this work, provide a reliable and simple approach to predict the minimal error of the single-point approach.
One crucial finding of the thesis is that the estimated f-maps from a single off-resonance differ from literature [14]. It is very likely that this is due to the different T_1-mapping approach that was used in this work. Therefore the choice of a proper T_1 mapping technique is essential for an accurate estimation of the bound pool fraction.
Compared with the MTR the fast bound pool fraction from a single off-resonance measurement has a longer scan time, which is mainly due to the T1-mapping. The advantage of the single-point approach is that it is more reliable than the MTR due to the independence of T_1. Therefore for a short extension of scan time one get a better quantitative marker for the myelin density.
In conclusion the fast bound pool fraction estimation from a single off-resonance measurement is a method that allows to acquire high resolution f-map within clinical acceptable scan times. Special care must be taken when comparing the absolute values of f-maps when different T_1-mapping approaches are used.

Bibliography

[1] S. D. Wolff and R. S. Balaban, "Magnetization transfer contrast (MTC) and tissue water proton relaxationin vivo," 1989.

[2] E. E. Odrobina, T. Y. J. Lam, T. Pun, R. Midha, and G. J. Stanisz, "MR properties of excised neural tissue following experimentally induced demyelination," *NMR in Biomedicine*, vol. 18, no. 5, pp. 277–284, 2005.

[3] J. H. van Waesberghe, W. Kamphorst, C. J. De Groot, M. A. van Walderveen, J. A. Castelijns, R. Ravid, G. J. Lycklama à Nijeholt, P. van der Valk, C. H. Polman, A. J. Thompson, and F. Barkhof, "Axonal loss in multiple sclerosis lesions: magnetic resonance imaging insights into substrates of disability.," *Annals of neurology*, vol. 46, pp. 747–54, Nov. 1999.

[4] K. Schmierer, F. Scaravilli, D. R. Altmann, G. J. Barker, and D. H. Miller, "Magnetization transfer ratio and myelin in postmortem multiple sclerosis brain," *Annals of Neurology*, vol. 56, no. 3, pp. 407–415, 2004.

[5] N. Tambasco, P. Nigro, M. Romoli, S. Simoni, L. Parnetti, and P. Calabresi, "Magnetization transfer MRI in dementia disorders, Huntington's disease and parkinsonism," *Journal of the Neurological Sciences*, 2015.

[6] M. Garcia, M. Gloor, O. Bieri, E. W. Radue, J. M. Lieb, D. Cordier, and C. Stippich, "Imaging of Primary Brain Tumors and Metastases with Fast Quantitative 3-Dimensional Magnetization Transfer," *Journal of Neuroimaging*, vol. 25, no. 6, pp. 1007–1014, 2015.

[7] I. Berry, G. J. Barker, F. Barkhof, A. Campi, V. Dousset, J. M. Franconi, A. Gass, W. Schreiber, D. H. Miller, and P. S. Tofts, "A multicenter measurement of magnetization transfer ratio in normal white matter," *Journal of Magnetic Resonance Imaging*, vol. 9, no. 3, pp. 441–446, 1999.

[8] R. M. Henkelman, X. Huang, Q. S. Xiang, G. J. Stanisz, S. D. Swanson, and M. J. Bronskill, "Quantitative interpretation of magnetization transfer.," *Mag. Res. Med.*, vol. 29, no. 6, pp. 759–66, 1993.

[9] J. G. Sled and G. B. Pike, "Quantitative interpretation of magnetization transfer in

spoiled gradient echo MRI sequences.," *Journal of magnetic resonance (San Diego, Calif. : 1997)*, vol. 145, no. 1, pp. 24–36, 2000.

[10] J. G. Sled, "Quantitative imaging of magnetization transfer parameters in vivo using MRI," 2000.

[11] V. L. Yarnykh, "Pulsed Z-spectroscopic imaging of cross-relaxation parameters in tissues for human MRI: Theory and clinical applications," *Magnetic Resonance in Medicine*, vol. 47, no. 5, pp. 929–939, 2002.

[12] a. Ramani, C. Dalton, D. H. Miller, P. S. Tofts, and G. J. Barker, "Precise estimate of fundamental in-vivo MT parameters in human brain in clinically feasible times," *Magnetic Resonance Imaging*, vol. 20, no. 10, pp. 721–731, 2002.

[13] V. L. Yarnykh and C. Yuan, "Cross-relaxation imaging reveals detailed anatomy of white matter fiber tracts in the human brain," *NeuroImage*, vol. 23, no. 1, pp. 409–424, 2004.

[14] V. L. Yarnykh, "Fast macromolecular proton fraction mapping from a single off-resonance magnetization transfer measurement," *Magnetic Resonance in Medicine*, vol. 68, no. 1, pp. 166–178, 2012.

[15] H. R. Underhill, R. C. Rostomily, A. M. Mikheev, C. Yuan, and V. L. Yarnykh, "Fast bound pool fraction imaging of the in vivo rat brain: Association with myelin content and validation in the C6 glioma model," *NeuroImage*, vol. 54, no. 3, pp. 2052–2065, 2011.

[16] A. K. Smith, R. D. Dortch, L. M. Dethrage, and S. a. Smith, "Rapid, high-resolution quantitative magnetization transfer MRI of the human spinal cord," *NeuroImage*, vol. 95, pp. 106–116, 2014.

[17] V. L. Yarnykh, J. D. Bowen, and L. K. J. Henson, "dimensional Macromolecular Proton Fraction Mapping in Multiple Sclerosis 1," vol. 274, no. 1, 2015.

[18] E. Liepinsh and G. Otting, "Proton exchange rates from amino acid side chains–implications for image contrast.," *Magnetic resonance in medicine : official journal of the Society of Magnetic Resonance in Medicine / Society of Magnetic Resonance in Medicine*, vol. 35, no. 1, pp. 30–42, 1996.

[19] T. A. Fralix, T. L. Ceckler, S. D. Wolff, S. A. Simon, and R. S. Balaban, "Lipid bilayer and water proton magnetization transfer: Effect of cholesterol," *Magnetic Resonance in Medicine*, vol. 18, pp. 214–223, Mar. 1991.

[20] S. H. Koenig and R. D. Brown, "Field-cycling relaxometry of protein solutions and tissue: Implications for MRI," *Progress in Nuclear Magnetic Resonance Spectroscopy*, vol. 22, pp. 487–567, Jan. 1990.

[21] R. M. Henkelman, G. J. Stanisz, and S. J. Graham, "Magnetization transfer in MRI: A review," *NMR in Biomedicine*, vol. 14, no. 2, pp. 57–64, 2001.

[22] X. Wu and J. Listinsky, "Effects of Transverse Cross Relaxation on Magnetization Transfer," *Journal of Magnetic Resonance, Series B*, vol. 105, pp. 73–76, Sept. 1994.

[23] G. Caines, T. Schleich, and J. M. Rydzewski, "Incorporation of magnetization transfer into the formalism for rotating-frame spin-lattice proton NMR relaxation in the presence of an off-resonance-irradiation field," *Journal of Magnetic Resonance (1969)*, vol. 95, no. 3, pp. 558–566, 1991.

[24] C. Morrison and R. M. Henkelman, "A model for magnetization transfer in tissues," *Magnetic Resonance in Medicine*, vol. 33, no. 4, pp. 475–482, 1995.

[25] J. G. Li, S. J. Graham, and R. M. Henkelman, "A flexible magnetization transfer line shape derived from tissue experimental data," *Magnetic Resonance in Medicine*, vol. 37, no. 6, pp. 866–871, 1997.

[26] G. B. Pike, G. H. Glover, B. S. Hu, and D. R. Enzmann, "Pulsed magnetization transfer spin-echo MR imaging.," *Journal of magnetic resonance imaging : JMRI*, vol. 3, no. 3, pp. 531–539, 1993.

[27] S. J. Graham and R. M. Henkelman, "Transfer," *Journal of magnetic resonance imaging : JMRI*, no. 5, pp. 903–912, 1997.

[28] S. Ropele and F. Fazekas, "Magnetization Transfer MR Imaging in Multiple Sclerosis," *Neuroimaging Clinics of North America*, vol. 19, no. 1, pp. 27–36, 2009.

[29] M. Soellinger, C. Langkammer, T. Seifert-Held, F. Fazekas, and S. Ropele, "Fast bound pool fraction mapping using stimulated echoes," *Magnetic Resonance in Medicine*, vol. 66, no. 3, pp. 717–724, 2011.

[30] D. F. Gochberg, R. P. Kennan, and J. C. Gore, "Quantitative Studies of Magnetization Transfer by Selective Excitation and TI Recovery," *Magn Reson Med*, vol. 38, no. 11, pp. 224–231, 1997.

[31] D. F. Gochberg, R. P. Kennan, M. D. Robson, and J. C. Gore, "Quantitative imaging of magnetization transfer using multiple selective pulses.," *Magnetic Resonance in Medicine*, vol. 41, no. 5, pp. 1065–72, 1999.

[32] D. F. Gochberg and J. C. Gore, "Quantitative imaging of magnetization transfer using an inversion recovery sequence," *Magnetic Resonance in Medicine*, vol. 49, no. 3, pp. 501–505, 2003.

[33] R. D. Dortch, K. Li, D. F. Gochberg, E. B. Welch, A. N. Dula, A. a. Tamhane, J. C. Gore, and S. a. Smith, "Quantitative magnetization transfer imaging in human brain at 3 T via selective inversion recovery," *Magnetic Resonance in Medicine*, vol. 66, no. 5, pp. 1346–1352, 2011.

[34] M. Gloor, K. Scheffler, and O. Bieri, "Quantitative magnetization transfer imaging using balanced SSFP.," *Magnetic resonance in medicine : official journal of the Society of Magnetic Resonance in Medicine / Society of Magnetic Resonance in Medicine*, vol. 60, no. 3, pp. 691–700, 2008.

[35] M. Gloor and B. Ag, "Magnetization Transfer Imaging Using Steady-State Free Precession MR Sequences," 2010.

[36] A. Haase, J. Frahm, D. Matthaei, W. Hanicke, and K.-D. Merboldt, "FLASH imaging. Rapid NMR imaging using low flip-angle pulses," *Journal of Magnetic Resonance (1969)*, vol. 67, pp. 258–266, Apr. 1986.

[37] E. M. Haacke, R. W. Brown, M. R. Thompson, and R. Venkatesan, *Magnetic Resonance Imaging: Physical Principles and Sequence Design*. 1999.

[38] D. C. Look, "Time Saving in Measurement of NMR and EPR Relaxation Times," *Review of Scientific Instruments*, vol. 41, no. 2, p. 250, 1970.

[39] J. P. Marques, T. Kober, G. Krueger, W. van der Zwaag, P.-F. Van de Moortele, and R. Gruetter, "MP2RAGE, a self bias-field corrected sequence for improved segmentation and T1-mapping at high field.," *NeuroImage*, vol. 49, pp. 1271–81, Jan. 2010.

[40] J. P. Mugler and J. R. Brookeman, "Three-dimensional magnetization-prepared rapid gradient-echo imaging (3D MP RAGE).," *Magnetic resonance in medicine*, vol. 15, pp. 152–7, July 1990.

[41] E. K. Fram, R. J. Herfkens, G. Johnson, G. H. Glover, J. P. Karis, A. Shimakawa, T. G. Perkins, and N. J. Pelc, "Rapid calculation of T1 using variable flip angle gradient refocused imaging," *Magnetic Resonance Imaging*, vol. 5, pp. 201–208, Jan. 1987.

[42] G. H. Glover and E. Schneider, "Three-point dixon technique for true water/fat decomposition withB0 inhomogeneity correction," *Magnetic Resonance in Medicine*, vol. 18, pp. 371–383, Apr. 1991.

[43] R. Stollberger and P. Wach, "Imaging of the activeB1 fieldin vivo," *Magnetic Resonance in Medicine*, vol. 35, pp. 246–251, Feb. 1996.

[44] G. R. Morrell, "A phase-sensitive method of flip angle mapping.," *Magnetic resonance in medicine*, vol. 60, pp. 889–94, Oct. 2008.

[45] V. L. Yarnykh, "Actual flip-angle imaging in the pulsed steady state: A method for rapid three-dimensional mapping of the transmitted radiofrequency field," *Magnetic Resonance in Medicine*, vol. 57, no. 1, pp. 192–200, 2007.

[46] L. I. Sacolick, F. Wiesinger, I. Hancu, and M. W. Vogel, "B 1 mapping by Bloch-Siegert shift," *Magnetic Resonance in Medicine*, vol. 63, no. 5, pp. 1315–1322, 2010.

[47] R. Pohmann and K. Scheffler, "A theoretical and experimental comparison of different techniques for B_1 mapping at very high fields.," *NMR in biomedicine*, vol. 26, pp. 265–75, Mar. 2013.

[48] J. L. Andersson and S. N. Sotiropoulos, "An integrated approach to correction for off-resonance effects and subject movement in diffusion MR imaging," *NeuroImage*, vol. 125, pp. 1063–1078, Jan. 2016.

[49] S. M. Smith, Y. Zhang, M. Jenkinson, J. Chen, P. Matthews, A. Federico, and N. De Stefano, "Accurate, Robust, and Automated Longitudinal and Cross-Sectional Brain Change Analysis," *NeuroImage*, vol. 17, pp. 479–489, Sept. 2002.

[50] S. M. Smith, M. Jenkinson, M. W. Woolrich, C. F. Beckmann, T. E. J. Behrens, H. Johansen-Berg, P. R. Bannister, M. De Luca, I. Drobnjak, D. E. Flitney, R. K. Niazy, J. Saunders, J. Vickers, Y. Zhang, N. De Stefano, J. M. Brady, and P. M.

Matthews, "Advances in functional and structural MR image analysis and implementation as FSL.," *NeuroImage*, vol. 23 Suppl 1, pp. S208–19, Jan. 2004.

[51] S. Portnoy and G. J. Stanisz, "Modeling pulsed magnetization transfer," *Magnetic Resonance in Medicine*, vol. 58, no. 1, pp. 144–155, 2007.

[52] P. Mossahebi, V. L. Yarnykh, and A. Samsonov, "Analysis and correction of biases in cross-relaxation MRI due to biexponential longitudinal relaxation," *Magnetic Resonance in Medicine*, vol. 71, no. 2, pp. 830–838, 2014.

[53] O. Dietrich, J. G. Raya, S. B. Reeder, M. F. Reiser, and S. O. Schoenberg, "Measurement of signal-to-noise ratios in MR images: Influence of multichannel coils, parallel imaging, and reconstruction filters," *Journal of Magnetic Resonance Imaging*, vol. 26, no. 2, pp. 375–385, 2007.

[54] J. Vymazal, R. A. Brooks, C. Baumgarner, V. Tran, D. Katz, J. W. Bulte, R. Bauminger, and G. Di Chiro, "The relation between brain iron and NMR relaxation times: an in vitro study.," *Magnetic resonance in medicine*, vol. 35, pp. 56–61, Jan. 1996.

[55] C. Birkl, C. Langkammer, J. Haybaeck, C. Ernst, R. Stollberger, F. Fazekas, and S. Ropele, "Temperature-induced changes of magnetic resonance relaxation times in the human brain: A postmortem study," *Magnetic Resonance in Medicine*, vol. 71, no. 4, pp. 1575–1580, 2014.

[56] H. R. Underhill, C. Yuan, and V. L. Yarnykh, "Direct quantitative comparison between cross-relaxation imaging and diffusion tensor imaging of the human brain at 3.0 T.," *NeuroImage*, vol. 47, no. 4, pp. 1568–1578, 2009.

[57] J. G. Sled and G. B. Pike, "Quantitative imaging of magnetization transfer exchange and relaxation properties in vivo using MRI.," *Magnetic resonance in medicine*, vol. 46, no. 5, pp. 923–31, 2001.